Covenant Journal of Engineering Technology (CJET)

Vol. 2 No. 1, June 2018

Articles

An Open Access Journal Available Online

Slug Flow in Large Diameter Pipeline-Riser Systems: Prediction and Mitigation

Adegboyega B. Ehinmowo[1,2*], Yi Cao[1] & Hoi C. Yeung[1]

[1]Oil and Gas Engineering Centre, Cranfield University, Bedfordshire, United Kingdom
[2]Chemical and Petroleum Engineering Department, University of Lagos, Lagos, Nigeria

Abstract- Slug flow could pose serious threat to oil and gas production facility. The objective of the study was to gain better insight into the behaviour of slug flow in large pipe diameter pipeline-riser system. The influence of geometry configuration on the slug characteristics was also investigated. The understanding of these are very important in the development of effective slug control strategy. Numerical simulations were carried out on a 3.7 km long horizontal pipeline leading to a 0.13 km vertical riser using an industrial software package. The pipeline and riser are both of 17" internal diameter. Slug envelopes were developed for the pipeline-riser system and its constituents' pipes. A total number of 572 data points were investigated, covering superficial velocities ranging from 0.01 to 44.28 m/s for gas and 0.02 and 8.25 m/s for liquid. The results showed three distinct slug flow regions: region due to horizontal pipeline slugging (H) where slugs formed in the horizontal pipeline are transported through the riser pipe nearly unchanged, region due to both horizontal and vertical pipes slug contributions (I) where the slugs formed in the horizontal pipe keeps growing even through the riser pipe and region due to vertical pipe slugging (V) where slug formation was predominantly due to the vertical pipe. The observed phenomenon is in consonance qualitatively with the experimental studies published in another paper, but quantitatively different and this may be due to diameter effect. The results also showed that choking can indeed be used to mitigate slug flow in all the regions but at considerable cost. The valve must be choked down at various degrees depending on the regions (flow conditions). There is therefore, the need to seek a better way of stabilizing slug flow bearing in mind the distinct behaviours of the identified regions.

Keywords: Slug flow, Choking, slug mitigation, Leda Flow, slug regions

I. Introduction

Slug flow is one of the challenges due to multiphase transportation of liquid and gas in a pipeline. This phenomenon can pose significant threat to oil and gas production facilities. Operational induced slug flow, hydrodynamic slug flow and severe slug flow are the widely known types. This study is dedicated to gaining insight into the behaviour of hydrodynamic slug flow in pipeline-riser systems and the impact of geometry interaction on slug flow. The understanding of this behaviour is very important in the development of effective slug control strategy to ensure that flow assurance demands are satisfied. The optimum design of the transporting pipelines and receiving facilities would be impossible without adequate understanding of the nature of slug flow expected in such system.

Hydrodynamic slug flow is known to occur in horizontal and near horizontal pipelines. In these pipelines, slugs can be formed from stratified regime by two main mechanisms. They are: growth of hydrodynamic instabilities and liquid accumulation due to instantaneous imbalance between pressure and gravitational forces caused by pipe undulation. The growth of hydrodynamic instability can be explained by the Kelvin Helmholtz (KH) instability theory while the second is usually referred to as terrain induced slug. It has been reported that slug formation can be as a result of either of these mechanisms or combination of both [1]. A good number of experimental and numerical works have been conducted to study slug initiation and evolution of two phase flows in horizontal pipes [1]–[6].

Previous studies have also provided significant understanding on the flow of hydrodynamic slug in horizontal pipes [6]–[11] and behaviour of severe slug flow in pipeline-riser system[12]–[17]. However, only few studies exist on hydrodynamic slug flow in pipeline-riser system and the impact of geometry [18], [19]. There is therefore the need to gain better understanding on the behaviour of slug flow in pipeline-riser system before an appropriate control strategy can be deployed.

Numerical tools provide an advantage of investigating industrial systems which are of larger sizes compared to the available experimental facilities. In this study, LedaFlow-one dimensional (1D) industrial multiphase code was used for numerical modelling and simulation of slug flow in pipeline-riser system. This helps to gain a good understanding of slug flow in pipeline-riser system. This understanding is needed for the development of an appropriate strategy for the slug attenuation. The well-established flow pattern maps were developed with special interest in the slug flow regime.

Flow regimes in Leda Flow are identified in terms of numeric values that correspond to the different flow regimes namely Stratified Flow = 1, Annular Flow = 2, Slug Flow = 3 and Bubbly Flow = 4. Details of the development and the mathematical models used in this software package

have been previously presented in literatures [20], [21].

This paper is organized as follows: in section 2, the methodology adopted for this study was presented; In section 3, the results were presented and discussed while section 4 presents the response of the slug flow to choking as a mitigation method. The work was concluded in the last section.

II. Methodology

Extensive numerical studies were conducted on a large size pipeline-riser system. The pipeline-riser system was a 3.7 km long horizontal pipeline leading to a 0.13 km vertical riser; both pipeline and riser are of 17" internal diameter as shown in Figure 1. Slug studies were also carried out on the horizontal pipeline and the vertical riser with a riser top valve. These geometries were discretised and grid sensitivity studies conducted. A total of 1800 cells was observed to be the optimum mesh and was adopted for this study.

A total number of 572 data points were investigated, covering superficial velocities ranging from 0.01 to 44.28 m/s for gas and 0.02 and 8.25 m/s for liquid.

In order to carry out a simulation study in LedaFlow, fluid property file must be specified. The information about the properties and amount of the fluid for a given range of temperature and pressure are housed in this file usually referred to as PVT file. The fluid properties and pipe materials properties are shown in Table 1 and 2 respectively.

Table 1 Fluid Properties

Component	Gas	OIl	Water
Density [kg/m^3]	23	780	1000
Viscosity [kg/m-s]	1.3×10^{-5}	1.1×10^{-3}	3.5×10^{-4}

Table 2 Properties of pipes and insulation materials

Material	Density [kg/m^3]	Specific heat [j/kg C]	Thermal conductivity [W/m C]
Material 1	7850	500	50
Material 2	2500	880	1

Materials 1 and 2 are the steel pipe and the insulation respectively. The heat transfer coefficient and pipe roughness values of 10 W/m^2-K and 4.572e^{-5} m were used respectively.
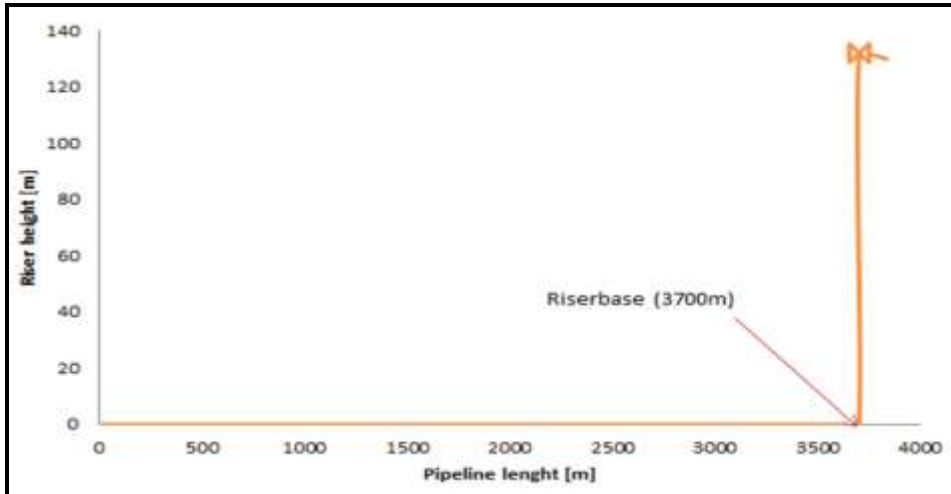
Fig. 1: Geometry of pipeline-riser system.

The numerical simulations of the pipeline-riser, horizontal and vertical pipes were carried out for various flow conditions using the various models (Unit cell, and slug capturing). A total number of about 572 simulations were done and a good number of the results fall within the slug region. The flow regime indicators in the software package were used to judge the presence or absence of slugging for the unit cell model while the fluctuation of the flow variables like pressure, mass flow rate and so on were used for the slug capturing. The superficial velocities were used to generate the flow envelopes which were analyzed to understand the behaviour of slug flow in pipeline-riser system.

Ⅲ. **Results and Discussions**

The slug envelopes obtained from horizontal pipeline, vertical pipeline, pipeline with riser downstream were discussed and comparisons of these systems have been made. Comparisons were also made between the envelopes obtained for various models.

Slug Flow Envelopes for the Horizontal Pipeline

The pure horizontal 3.7km, 17'' internal diameter pipeline described in section 2 was investigated and a total number of 332 data points were studied covering superficial velocities ranging from 0.039 to 34.99 m/s for gas and 0.18 and 8.25 m/s for liquid. Figure 2 shows the slug envelopes for the horizontal pipeline as predicted by slug capturing and unit cell models designated as SC and NSC. The regions reported to be void of slugging by unit cell model were reported to suffer slugging by the slug capturing model. It was observed that up to superficial gas flow rate of 9 m/s, slugs were observed for SC whereas none was observed at this condition for NSC. It appears that unit cell model under predicts slug envelope compared to the slug capturing models.

Figure 2 also shows the slug flow regime obtained from these models compared with the flow regime map provided by Mandhane et al. [22]. The Figure shows that considerable amount of data investigated for slug fall within the slug region of [22] and some region predicted as slug fall within the non-slug region and vice versa. This could be as a result of the effect of the difference in pipe diameter.
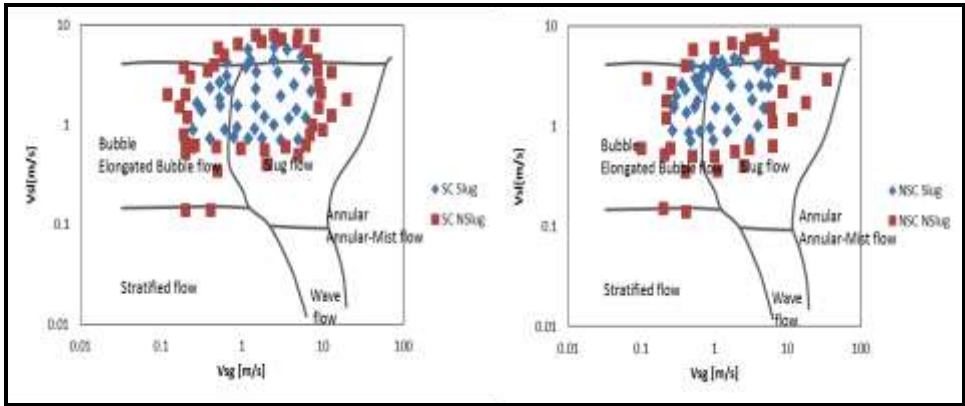
(a) Slug capturing model (SC)   (b) Unit cell model (NSC)

Fig. 2 Numerical flow regime compared with Mandhane et al.[22] flow regime

Slug Flow Envelopes for the Vertical Pipe

The slug flow envelope for the vertical pipe is as shown in Figure 3. It appears that the base of the envelope is wider and taper towards the top. This implies that in a vertical pipeline, slugs are formed at low flow rates and medium flow rates and not likely to occur at high flow rates. Though the envelope seems tilted compared to what was reported in the literatures for example Barnea [23].

(a) **Slug capturing model (SC)**   (b) **Unit cell model (NSC)**

Fig. 3 Numerical flow regime compared with Barnea [23] flow regime

Figure 3 also shows the slug flow regime obtained from the numerical studies compared with the flow regime map of Barnea [23]. The Figure shows that considerable amount of data fall within the slug region as predicted by Barnea [23]. However, some region predicted as slug by the models fall within the non-slug region and vice versa. This again could be a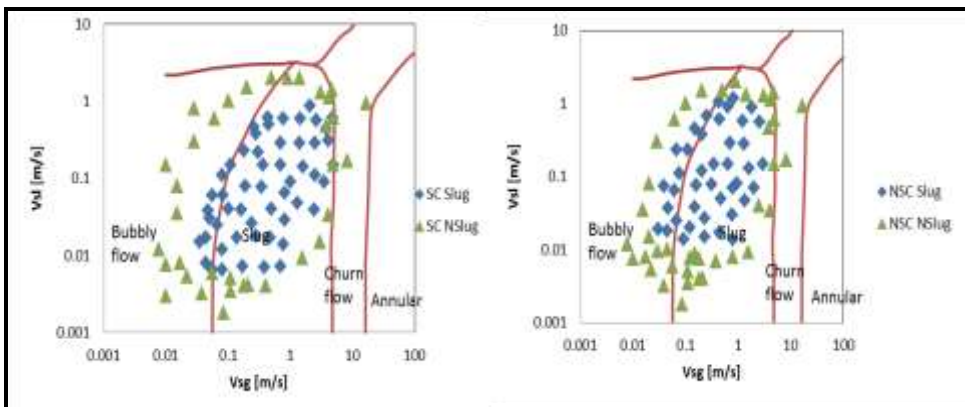s a result of the effect of the difference in pipe diameter. Again, it was observed that the unit cell model and the slug capturing predict at different levels. The region predicted by slug capturing model appears to be larger than that of unit cell model.

Slug Flow Envelopes for the Pipeline-riser System
The pipeline-riser system described in section 2 was studied for superficial velocities ranging from 0.01 to 44.28 m/s and 0.02 to 8.23 m/s for gas and liquid respectively. A total of 192 data points were studied. It was observed that at high flow rate the hydrodynamic slug was dominating the slugging in the pipeline-riser system. But at low flow rate the slug formation dynamics changed and the riser system dominates the slug formation mechanism.

Figure 4 shows the slug flow envelope developed for this pipeline riser system compared with flow regime map of Schmidt et al.[13]. Considerable number of data points investigated fall within the slug flow regime while the rest fall within the non-slug regime. Severe slug flow was reported in Schmidt et al.[13], however, such was not observed in this study. The region where hydrodynamic slug was observed in this study covers significant parts of regions reported as dispersed, bubble and transition to severe slug flow in Schmidt et al.[13]. This may be due to difference in pipeline-riser geometry
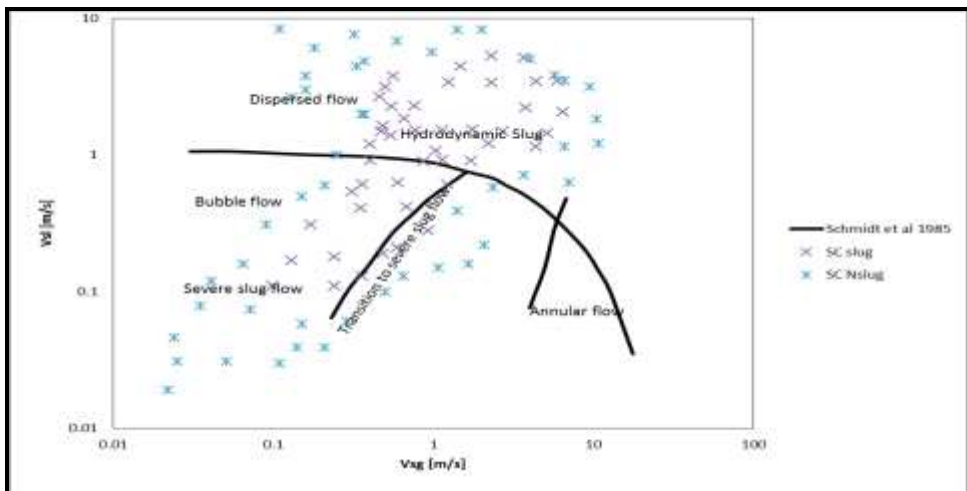

Fig. 4 Numerical flow regime compared with map of Schmidt et al. [13]

Slug Flow Envelopes for the Pipeline-riser System

This section seeks to obtain full qualitative picture of slug flow behaviour in a pipeline-riser system. To achieve this, comparisons were made between horizontal, vertical, and the pipeline-riser system envelopes.

From Figure 5, it was shown that at low flow rates slug flow occurs in vertical pipes whereas relatively higher flow rate is needed to experience slug in horizontal pipe. This is in consonance with previous works for example Schmidt [24] and Schmidt et al. [18].

The comparison of the horizontal, vertical and pipeline-riser envelopes shows that at low flow rates, the region where slugs were not experienced in horizontal pipeline suffer slugs in both vertical pipe and pipeline riser systems as can be seen in Figure 5. This can be traced to the fact that the mechanisms for hydrodynamic slug formation in horizontal and slug flow in vertical pipes are not same. In horizontal pipelines sufficient liquid level is needed for the interfacial waves to grow and block the pipe cross section [11], [25] whereas in vertical pipe, at low gas and liquid flow rates slug flow will occur when gas bubble usually referred to as Taylor bubble is formed and large enough to block the pipe cross section and hinder the flow of the heavier fluid (liquid slug). This usually leads to the instability in riser pipe [18] .
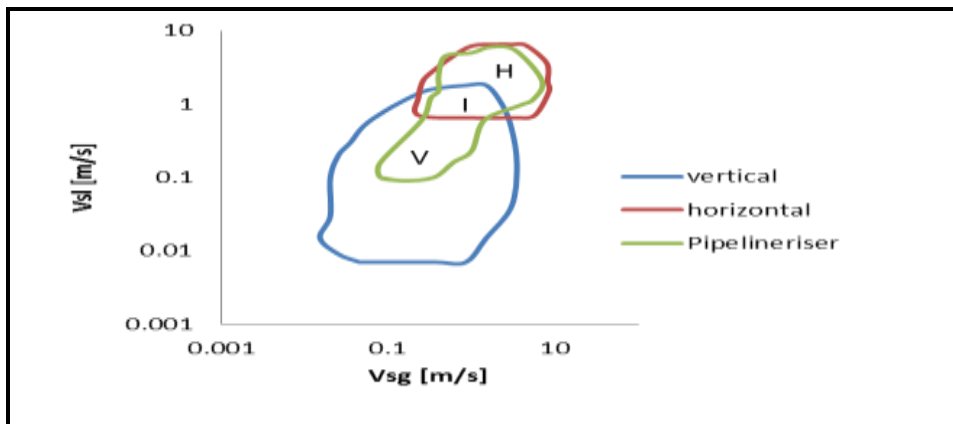
Fig. 5 Slug flow behavior in pipeline-riser system

The Figure also shows that the slug occurring at high flow rates in the pipeline-riser is due to slugs in the horizontal pipeline. The slug formed in the upstream horizontal pipeline is transported through the riser pipe under the same conditions where slug is absent for the vertical pipe. This implies that at high flow rates, the slug flow rate in the vertical riser are due to the slug flow from horizontal pipe upstream the riser pipe [13].This type of behaviour was reported for a gas-liquid flow in large pipeline-riser system where the effect of upstream configurations was investigated [26].

It can also be seen from the Figure that, there is significant reduction in the area prone to slugging in a vertical pipe compared to the pipeline-riser system. This could be due to the interaction between the pipeline and riser. This suggests the upstream horizontal pipeline has significant effect on the slug flow in the pipeline-riser system [26].

Figure 5 ultimately provides a clearer picture of the slug behaviour in pipeline-riser. The software package predicts three regions designated as head/horizontal (H), intersection/neck (I), and vertical/handle (V).

The region H shows the region due to slugs contributed from the horizontal pipeline. This region occurs at high flow rates and could have the characteristics of typical normal slug flow.

The intersection region (I) is the area where the horizontal and vertical envelopes intersect. It appears that both hydrodynamic slugs from the horizontal and slugs in the vertical pipes contribute to the slug behaviour in this region. This region could be complex and difficult to control as there would be interplay between different mechanisms.

Region V is the portion of the envelope below both H and I. It occurs at low flow rates. This is believed to be the region influenced by the vertical section of the pipeline-riser system, though it is narrower than the original portion of the vertical slug envelope. Region V was not originally present in a pure horizontal pipeline but appears in the pipeline-riser system which shows the contribution of the vertical section to the pipeline riser slugging. This shows clearly that both the horizontal and vertical pipes which constitute a pipeline riser system mutually affect the slug behaviour. The larger part of the slug region in the pipeline-riser system seems to be due to the contribution from the horizontal pipe. Therefore, the dynamics of the upstream pipeline cannot be neglected in the design of pipeline-riser system[18], [26].

Slug flow in H-region. From Figure 5, it is observed that the area designated as H region of the pipeline-riser slug envelope falls largely within the slug region of horizontal pipe. This region appears not to suffer slugging in the vertical region. It is therefore important to clarify if the overall dynamics of the pipeline-riser system is indeed determined by the horizontal pipe or not. A representative case in this region has been studied to observe the behaviour of slug in these systems.

Table 3 Properties of case study in H-region

Total mass flow [kg/s]	600
Gas mass fraction[-]	0.01
Oil mass fraction [-]	0.239
Water mass fraction [-]	0.751
Inlet Temperature [^{0}C]	90
Outlet Temperature [^{0}C]	40
PR outlet Pressure [bar]	22.5
Horiz outlet Pressure [bar]	27.95
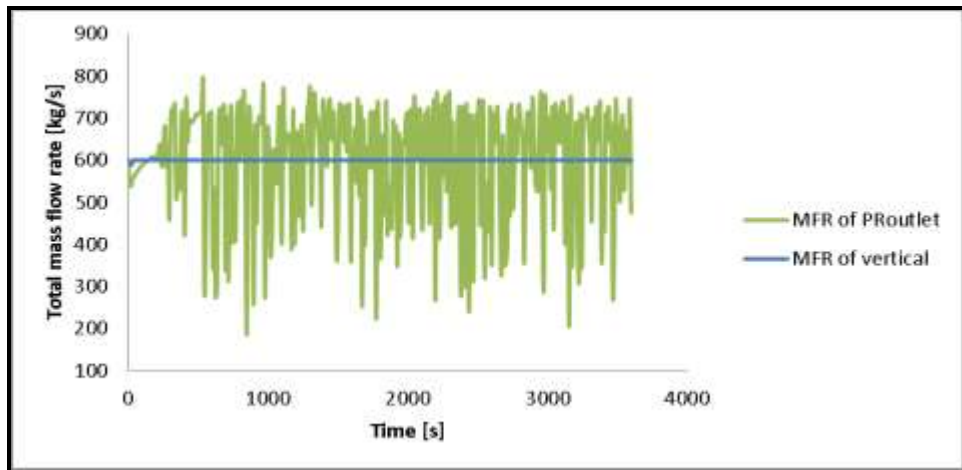
Fig. 6 Comparison of total mass flow rate for pure vertical pipe and pipeline-riser system

The evolution and dissipation of slug was studied in the pure horizontal pipeline and the pipeline-riser system using this case and the property of the case are summarised in Table 3. This representative flow condition corresponds to 2.48m/s and 4.50 m/s superficial velocities of gas and liquid respectively.

For a vertical pipe, this case did not experience any slugging as can be seen in Figure 6 when compared with the behaviour at the riser outlet. However, both the horizontal and pipeline-riser system were observed to suffer from slugging as shown in Figure 7.

Figure 7 (a) shows the trend plot of the total mass flow rates at 1km for pipeline-riser system (PR) and the horizontal pipeline (Horiz). It was observed that at 1 km from the inlet of the pipeline, the horizontal case has developed interfacial waves of peak in the 684 kg/s region. Similar waves were observed to have been formed in the pipeline-riser system. The highest peak of fluctuation recorded at this point for the pipeline-riser system was about 684kg/s apart from the initial surge which peaked at 708 kg/s.

Figure 7(b) shows the trend plot of total mass flow rates of the pipeline-riser system (PR) and the pure horizontal pipeline (Horiz) at 2km from the inlet. For the horizontal pipeline, the waves have grown to

form slugs and the flow fluctuating between 154 and 846 kg/s. Again similar trend was observed for the pipeline-riser system but with slightly lesser fluctuation around 183 and 808 kg/s. The initiation and development of slugs have been studied previously by many authors[3], [6], [11], [27], [28]. Ujang et al. [6] for example reported that in a 37m and 0.078m internal diameter pipe, slugs were initiated in the region of 3m from the inlet and

the slug further developed downstream the pipe. This is similar to the trend observed in Figures 7(b) and 7(c). Though they reported a reduction in slug frequency downstream the pipe from point of initiation, it appears that this is not the case in this study. This can be traced to the fact that there is enough liquid to enhance the slug growth and that the slug frequency has become independent of the distance from the inlet [29].

Fig. 7 H-region total mass flow rate (a) at 1 km from inlet, (b) at 2 km from inlet, (c) at 3 km from inlet, (d) 3.7 km (riser base)

Figure 7(c) shows the trend plot of total mass flow rates of the pipeline-riser system (PR) and the pure horizontal pipeline (Horiz) at 3km from the inlet. As can be seen the slugs have further grown when compared with Figure 7(b).

The pure horizontal pipe has further increased in flow fluctuation ranging from 150 and 1035kg/s while those in the pipeline-riser system fluctuate between 124 and 937kg/s. Again the frequency of the slugs was not observed to change. This suggests

that the liquid available in the pipelines are sufficient to offset the difference between the rate of liquid joining the slugs at the front and the rate of liquid leaving the slug at the back of the slugs [30], [31].

The constant frequency also suggests that the slug length in this region does not change. The average slug length was observed to be about 200 m which is greater than the riser height 130 m. This agrees with the observation of Brill et al.[32] that

hydrodynamic slug could be severe with length greater than the riser.

The total mass flow trend for the outlet of the pure horizontal pipeline and the riser base of the pipeline-riser system (3.7 km from the inlet) is shown in Figure 7(d). The horizontal pipeline experienced serious fluctuation ranging from 128 to 1620 kg/s whereas the flow in pipeline-riser system fluctuates between 142 and 1113kg/s. This quantitative difference in the behaviour of the slug at this point can be traced to the outlet boundary condition at the pure horizontal pipe and the riser base.

Slug flow in I-region. From Figure 5, it is shown that the area designated

as I region of the pipeline-riser slug envelope falls within the slug region of both pure horizontal pipe and vertical pipe. Again there is need to ascertain the contributions of the constituents' pipes making up the pipeline-riser system. A representative case of shown in Table 4 which corresponds to 0.25 m/s and 0.90 m/s superficial velocities of gas and liquid respectively in this region has been studied to observe the behavior of slug in these systems.

The evolution and dissipation of slug was studied in the pure horizontal pipeline and the pipeline-riser system using this case and the property of the case are summarized in Table 4.

Table 4 Properties of case study in I-region

Total mass flow [kg/s]	120
Gas mass fraction[-]	0.007
Oil mass fraction [-]	0.239
Water mass fraction [-]	0.754
Inlet Temperature [^{0}C]	90
Outlet Temperature [^{0}C]	40
PR outlet Pressure [bar]	22.5
Horiz outlet Pressure [bar]	27.95
Vert outlet Pressure [bar]	22.5

Figure 8(a) shows the trend plot of the total mass flow rates at 1km for pipeline-riser system (PR) and the pure horizontal pipeline (Horiz). It was observed that at 1 km from the inlet of the pipeline, the pure horizontal case has developed

interfacial waves of peak in the 135 kg/s region. Similar waves were observed to have been formed in the pipeline-riser system but appear to have higher amplitude towering to over 190kg/s. This behaviour could be traced to the liquid contribution from the riser pipe.
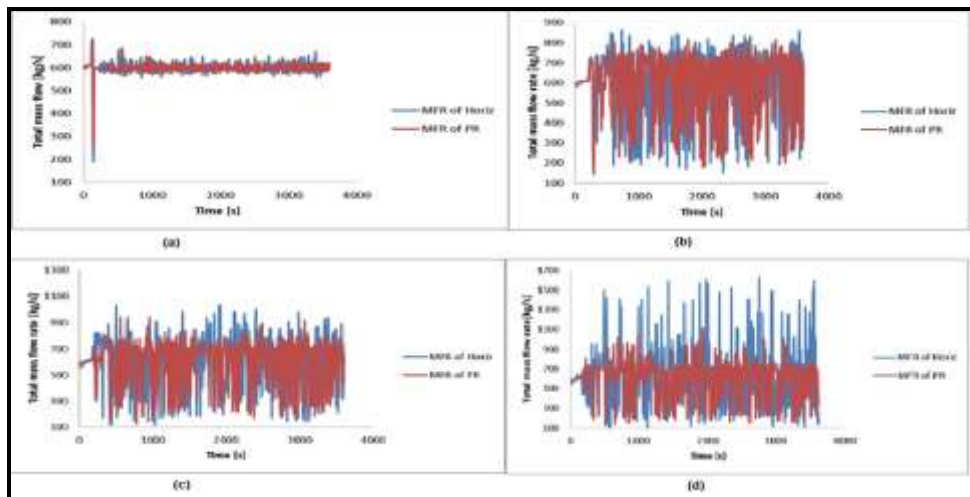
Fig. 8 I-region total mass flow rate (a) at 1 km from inlet, (b) at 2 km from inlet, (c) at 3 km from inlet, (d) 3.7 km (riser base)

Figure 8(b) shows the trend plot of total mass flow rates of the pipeline-riser system (PR) and the pure horizontal pipeline (Horiz) at 2km from the inlet. For the pure horizontal pipeline, the waves have grown to form slugs and the flow fluctuating between 46 and 150 kg/s. Again similar trend was observed for the pipeline-riser system but with higher fluctuation around 17 and 208 kg/s. It appears that the frequency has also increased further. This could be traced to the fact that more liquid is available from the riser pipe due to liquid fall back. This is believed to enhance the wave growth and the initiation of more slugs as the distance towards the riser base reduces from the inlet.

Figure 8(c) shows the trend plot of total mass flow rates of the pipeline-riser system (PR) and the pure horizontal pipeline (Horiz) at 3km from the inlet. As can be seen the slugs have further grown when compared with Figure 8(b). The pure horizontal pipe has further increase in flow fluctuation ranging from 39 and 198 kg/s while those in

the pipeline-riser system fluctuate between 11 and 284kg/s. However, the frequency of the slugs was observed to have reduced compared with Figure 8 (b). This could be due to release of some of the liquid for slug production in the riser pipe. It could also be that the slug has combined to form longer slugs [33]. The reduction in slug frequency downstream the pipe inlet has been previously reported for a 37m and 0.078m internal diameter pipe where slugs were initiated in the region of 3m from the inlet and developed further downstream with reduced frequency [6].

The total mass flow trend for the outlet of the pure horizontal pipeline and the riser base of the pipeline-riser system (3.7 km from the inlet) is shown in Figure 8(d). It appears that growth of slugs continued through the pure horizontal pipeline. The fluctuation lies within 39 and 210 kg/s range. This type of behaviour has been reported in Scott [33], and Zoeteweij [34]. Zoeteweij [34] observed that this type of slug that keeps growing till the end of the

pipeline is characterized by continuous change in length and can be difficult to predict and control. However, this view was not substantiated with any control study. Slug flow in V-region. From Figure 5, it was observed that the area designated as V region of the pipeline-riser slug envelope falls within the slug region of pure vertical pipe. This region is without slug in the pure horizontal envelope. A further investigation was conducted to determine the effect of geometry interaction on slug flow behaviour in this region. The evolution and dissipation of slug was studied in the pure horizontal pipeline and the pipeline-riser system using this case and the property of the case are summarised in Table 5. The representative flow condition investigated was equivalent to 0.2 m/s and 0.14 m/s superficial velocities of gas and liquid respectively.

For a pure horizontal case, this case did not experience any slugging as can be seen in Figure 9. However, both the vertical and pipeline-riser system were observed to suffer from slugging.

Table 5 Properties of case study in V-region

Total mass flow [kg/s]	19
Gas mass fraction[-]	0.04
Oil mass fraction [-]	0.239
Water mass fraction [-]	0.721
Inlet Temperature [^{0}C]	90
Outlet Temperature [^{0}C]	40
PR outlet Pressure [bar]	22.5
Horiz outlet Pressure [bar]	27.95

Figure 9(a) shows the trend plot of the total mass flow rates at 1km for pipeline-riser system (PR) and the pure horizontal pipeline (Horiz). It was observed that at 1 km from the inlet of the pipeline, the pure horizontal case remains stable at 19 kg/s and without any slug precursor or waves. However, for the pipeline-riser system, slug precursors were observed. This can be as a result of liquid fall back from the riser pipe which provides sufficient liquid in the pipeline for slug formation[13], [35]. The highest peak of fluctuation recorded at this point for the pipeline-riser system was about 28kg/s apart from the initial surge which peaked at 45 kg/s.

Figure 9(b) shows the trend plot of total mass flow rates of the pipeline-riser system (PR) and the pure horizontal pipeline at 2km from the inlet. Again for the pure horizontal pipeline, the flow is stable at 19 kg/s without any slug precursor or waves. However, the waves observed at 1km for the pipeline-riser system has grown further with the first surge peaking at about 89kg/s and the regular slug precursor at about 38kg/s.
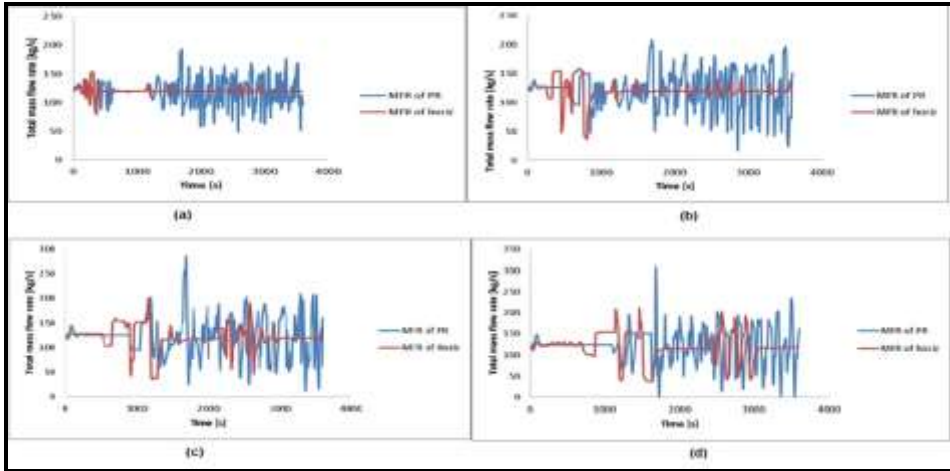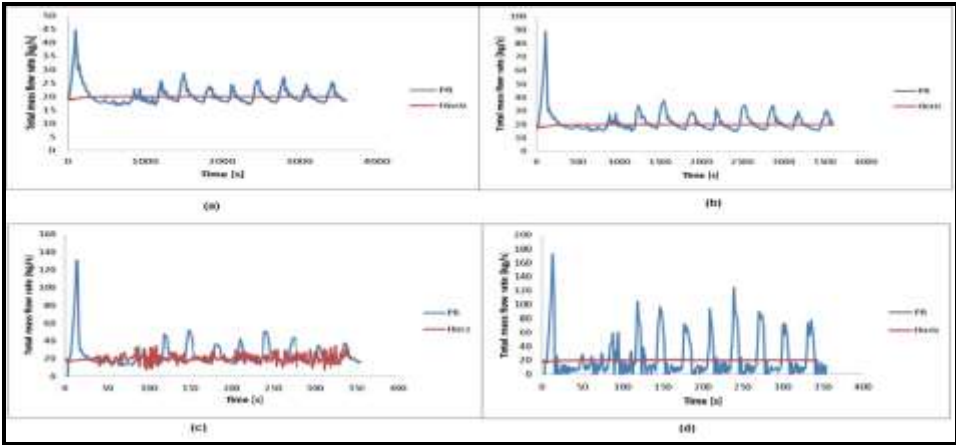
Fig. 9 V-region total mass flow rate (a) at 1 km from inlet, (b) at 2 km from inlet, (c) at 3 km from inlet, (d) 3.7 km (riser base)

Figure 9(c) shows the trend plot of total mass flow rates of the pipeline-riser system (PR) and the pure horizontal pipeline (Horiz) at 3km from the inlet. As can be seen the frequency of the slug precursors observed in the pipeline-riser system remain the same while the fluctuation in the total mass flow rate has moved further north. The first surge has now reached about 130 kg/s and the regular slugs peaked at about 50kg/s. Interestingly it was observed that the horizontal pipeline experienced some waves at the interface at this point. However, this interfacial wave dissipated before the outlet as can be seen in Figure 9(d). This could be because the available liquid height in the pipeline is not high enough to bridge the pipe for slug formation[36], [37].

Figure 9(d) shows trend plot for the total mass flow rate at the outlet of the pure horizontal pipeline and the riser base of the pipeline-riser system (3.7 km from the inlet). The horizontal pipeline experienced no slug at the outlet but slugging was observed at the riser base of the pipeline. This can be traced to the combination of the growth of the slug precursors transported from the horizontal part of the pipeline-riser system and the liquid fall back from the riser pipe. Slug growth was observed along the riser pipe as shown in increase in fluctuation amplitudes. The additional growth could be as a result of liquid fall back from the riser pipe and the inability of the incoming flow to overcome the hydrostatic head in the riser. This shows a clear contribution from the riser pipe to the slug formation in the pipeline-riser system.

Stabilizing Slug Flow in Pipeline-riser System using Choking Method

Three slug flow regions have been identified in the previous section and the behaviour explained. In this section, the potential of using increase in the downstream pressure to attenuate slug flow was investigated. This concept is investigated for each of the representative flow condition in the regions. The riser top choke valve was used to generate the pressure increase. This method has been extensively used in the oil and gas

14

industry to eliminate severe slug. The slug mitigation potential of this traditional method is investigated for the slug regions identified in this study. Bifurcation maps are generated for the representative slug flow conditions in these regions to further understand the behaviour of these slug types. Bifurcation map for H-region. Figure 10 (a) shows the riser base pressure bifurcation map of the industrial pipeline-riser system described in section 2. The flow and boundary condition for the representative flow condition is as shown in Table 3.

(a)

(b)

15
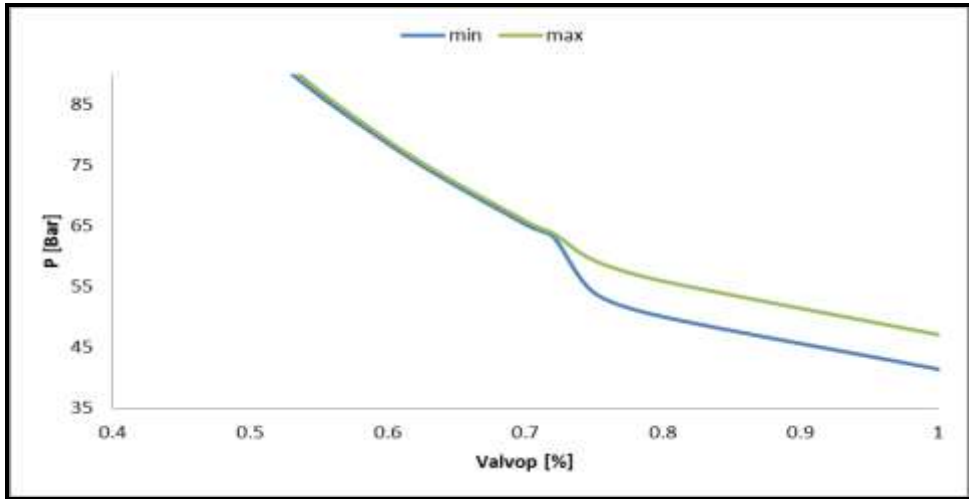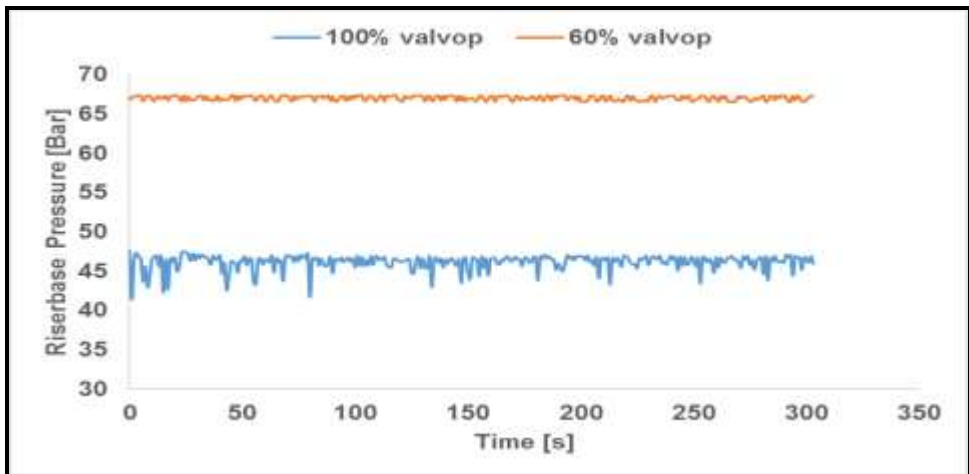
Fig. 10 H-region riser base pressure (a) bifurcation map of pipeline-riser system, (b) Riser base pressure trend at 100% valve opening and Riser base trend plot at 60% valve opening The blue dotted line runs through the bifurcation point which is 72% valve opening and at 63.85 bar. The right-hand plane of the line is the unstable region while the left hand plane is the stable region. Figures 10 (b) shows the riser base pressure trend plot at 100% and 60% valve opening respectively. It is shown that at 100% valve opening the system is unstable but at 60% valve opening the valve has supplied sufficient back pressure to stabilize the unstable flow.

Bifurcation map for I-region. The riser base pressure bifurcation map of the case described in Table 4 is shown in Figure 11. The stable and unstable region is divided using a dotted blue line and the fluctuation in the unstable region is enclosed by the blue and green lines. The green line connects the maximum pressures as the valve openings are varied while the blue line represents the corresponding minimum pressures. The bifurcation occurs at valve opening of 20% and 45.71 Bar.

Fig. 11 I-region riser base pressure bifurcation map for pipeline-riser system

Fig. 12 V-region riser base pressure bifurcation map for pipeline-riser syste

Bifurcation map for V-region. Figure 12 shows the riser base bifurcation map of the pipeline-riser system in the V-region. The dotted blue line serves to demarcate the stable f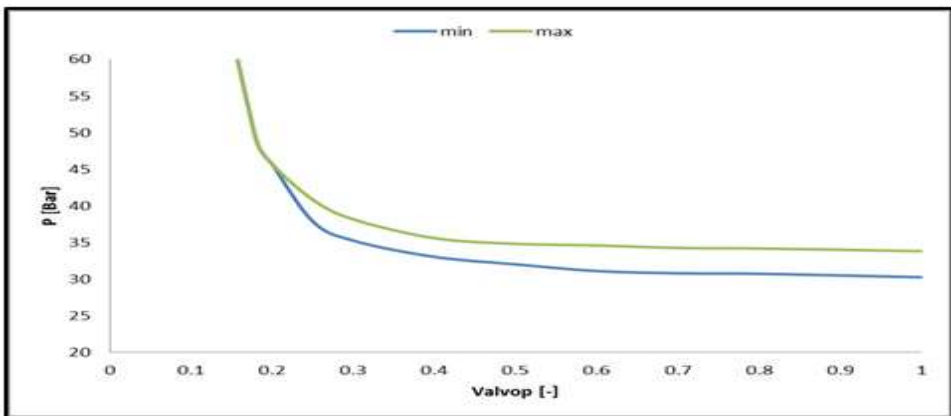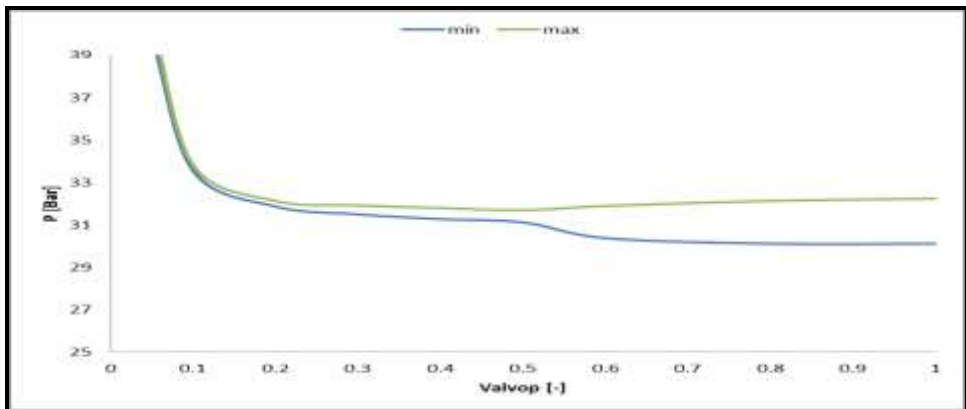rom unstable region. The green line connects the maximum pressure for all the valve openings while the blue line represents the pressure low peaks for all the valve openings. The bifurcation lies around 10% valve opening and pressure value of 33.7bar. Small amplitude fluctuations were experienced below 50% valve opening. At valve opening above 50%, the system was observed to experience a more chaotic instability. Though the maximum pressure fluctuation experienced is in the neighborhood of 2 Bar, the valve opening required to stabilize the system in this region is very small compared with other regions 72% and 20% for H-region and I-region respectively. This shows a degree of instability in this region compared with other regions. It is widely known that severe slugging occurs at a low flow rate but with the help of an inclined pipeline upstream the riser pipe[35]. However, in this study a pure upstream horizontal pipe was used. This suggests that whether an inclined pipe precedes a riser pipe or not, severe slugging can still occur. This view has been reported in earlier works[38]. It has been shown that significant choking was needed to stabilize the unstable hydrodynamic slug flow which unfortunately could mean less production [39]. It is therefore important to develop an approach to stabilizing the slug flow at larger valve opening.

The numerical results presented in this work and indeed the observed phenomenon is in consonance qualitatively with the experimental studies [40], but quantitatively different and the difference could be due to diameter effect. Although the software package used in this work predicted slug flow for a large vertical pipe, as opposed to churn flow that has been reported by several authors including Ali [41], the code developers might want to consider differentiating slug and churn flow regime in subsequent versions. However, churn flow has generally been classified as an intermittent flow, therefore the results may still be considered valid.

IV. Conclusion

The need to understand the behavior of slug flow in large diameter pipeline has necessitated this study. The understanding derived from this study can be pivotal to the design and operation of pipeline-riser system where slug flow is expected. Considerable insight has been gained from the results and the following conclusion can be drawn.

- There is significant reduction in the area prone to slugging in a vertical pipe compared with the pipeline-riser system. This could be due to the interaction between the pipeline and riser pipe. This suggests the upstream horizontal pipeline has significant effect on the slug flow in the pipeline-riser system.

- Three distinct slug regions and behavior were identified: region due to horizontal pipeline slugging (H) where slugs formed in the horizontal pipeline are transported through the riser pipe

nearly unchanged, region due to both horizontal and vertical pipes slug contributions (I) where the slugs formed in the horizontal pipe keeps growing even through the riser pipe and region due to vertical pipe slugging (V) were slug formation was predominantly due to the vertical pipe. The slugs in I and V regions are severe slugging-like.

• Choking can indeed be used to mitigate the slug flow in all the regions identified but at varying and considerable loss in production. The valve must be choked down at various degrees depending on the regions (flow conditions).

• The understanding of slug behavior in various regions of the envelopes could be useful in seeking a better way to stabilize slug flow in pipeline-riser system.

References
[1] R. I. Issa and M. H. W. Kempf, "Simulation of slug flow in horizontal and nearly horizontal pipes with the two-fluid model," *Int. J. Multiph. Flow*, vol. 29, no. 1, pp. 69–95, 2003.

[2] W. H. Ahmed, "Experimental investigation of air–oil slug flow using capacitance probes, hot-film anemometer, and image processing," *Int. J. Multiph. Flow*, vol. 37, no. 8, pp. 876–887, 2011.

[3]   M. R. Ansari and V. Shokri, "Numerical modeling of slug flow initiation in a horizontal channels using a two-fluid model," *Int. J. Heat Fluid Flow*, vol. 32, no. 1, pp. 145–155, 2011.

[4]   C. Vallée, T. Höhne, H.-M. Prasser, and T. Sühnel, "Experimental investigation and CFD simulation of horizontal stratified two-phase flow phenomena," *Benchmarking CFD Codes Appl. to Nucl. React. Saf.*, vol. 238, no. 3, pp. 637–646, 2008.

[5] P. Valluri, P. D. M. Spelt, C. J. Lawrence, and G. F. Hewitt, "Numerical simulation of the onset of slug initiation in laminar horizontal channel flow," *Int. J. Multiph. Flow*, vol. 34, no. 2, pp. 206–225, 2008.

[6] P. M. Ujang, C. J. Lawrence, C. P. Hale, and G. F. Hewitt, "Slug initiation and evolution in two-phase horizontal flow," *Int. J. Multiph. Flow*, vol. 32, no. 5, pp. 527–552, 2006.

[7]   K. Bendiksen and M. Espedal, "Onset of slugging in horizontal gas-liquid pipe flow," *Int. J. Multiph. Flow*, vol. 18, no. 2, pp. 237–247, 1992.

[8] E. T. Hurlburt and T. J. Hanratty,

"Prediction of the transition from stratified to slug and plug flow for long pipes," *Int. J. Multiph. Flow*, vol. 28, no. 5, pp. 707–729, 2002.

[9] U. Kadri, R. F. Mudde, R. V. A. Oliemans, M. Bonizzi, and P. Andreussi, "Prediction of the transition from stratified to slug flow or roll-waves in gas–liquid horizontal pipes," *Int. J. Multiph. Flow*, vol. 35, no. 11, pp. 1001–1010, 2009.

[10] U. Kadri, R. F. Mudde, and R. V. A. Oliemans, "On the prediction of the transition from stratified flow to roll waves and slug flow in horizontal pipes," in *13th International Conference on Multiphase Production Technology*, 2007, p. 65.

[11] Z. Fan, F. Lusseyran, and T. J. Hanratty, "Initiation of slugs in horizontal gas liquid flows," *AIChE J.*, vol. 39, no. 11, pp. 1741–1753, 1993.

[12] J. L. Baliño, K. P. Burr, and R. H. Nemoto, "Modeling and simulation of severe slugging in air-water pipeline-riser systems," *Int. J. Multiph. Flow*, vol. 36, no. 8, pp. 643–660, 2010.

[13] Z. Schmidt, D. Doty, and K. Dutta-Roy, "Severe slugging in offshore pipeline riser-pipe systems," *Old SPE J.*, vol. 25, no. 1, pp. 27–38, 1985.

[14] Y. Taitel, S. Vierkandt, O. Shoham, and J. P. Brill, "Severe slugging in a riser system: experiments and modeling," *Int. J. Multiph. Flow*, vol. 16, no. 1, pp. 57–68, 1990.

[15] V. Tin and M. M. Sarshar, "An investigation of severe slugging characteristics in flexible risers," in *Proc. 6th Int. Conf. on Multiphase Production, BHRG, France*, 1993, vol. 205, p. 228.

[16] L. Xing, H. Yeung, J. Shen, and Y. Cao, "Numerical study on mitigating severe slugging in pipeline/riser system with wavy pipe," *Int. J. Multiph. Flow*, vol. 53, pp. 1–10, Jul. 2013.

[17] R. Malekzadeh, R. Henkes, and R. F. Mudde, "Severe slugging in a long pipeline–riser system: Experiments and predictions," *Int. J. Multiph. Flow*, vol. 46, pp. 9–21, Nov. 2012.

[18] Z. Schmidt, J. P. Brill, and H. D. Beggs, "Experimental Study of Two-phase Normal Slug Flow in a Pipeline -riser Pipe System.," *J. Energy Resour. Technol. Trans. ASME*, vol. 103, no. 1, pp. 67–75, 1981.

[19] E. Guzman Vazquez and Y. Fairuzov, "A study of normal slug flow in an offshore production facility with a large diameter flowline," *SPE Prod. Oper.*, vol. 24, no. 1, pp. 171–179, 2009.

[20] T. J. Danielson, K. M. Bansal, R. Hansen, and E. Leporcher, "LEDA: the next multiphase flow performance simulator," in *12th International Conference on Multiphase Production Technology*, 2005.

[21] A. Goldszal, J. I. Monsen, T. J.

Danielson, K. M. Bansal, Z. L. Yang, S. T. Johansen, and G. Depay, "LedaFlow 1D: Simulation results with multiphase gas/condensate and oil/gas field data," in *13th International Conference on Multiphase Production Technology*, 2007.

[22] J. M. Mandhane, G. A. Gregory, and K. Aziz, "A flow pattern map for gas—liquid flow in horizontal pipes," *Int. J. Multiph. Flow*, vol. 1, no. 4, pp. 537–553, 1974.

[23] D. Barnea, "A unified model for predicting flow-pattern transitions for the whole range of pipe inclinations," *Int. J. Multiph. Flow*, vol. 13, no. 1, pp. 1–12, 1987.

[24] Z. Schmidt, "Experimental study of two-phase slug flow in a pipeline-riser pipe system," University of Tulsa, Tulsa, 1977.

[25] Z. Ruder, P. J. Hanratty, and T. J. Hanratty, "Necessary conditions for the existence of stable slugs," *Int. J. Multiph. Flow*, vol. 15, no. 2, pp. 209–226, 1989.

[26] N. K. Omebere-Iyari and B. J. Azzopardi, "Gas/liquid flow in a large riser: effect of upstream configurations," in *13th International Conference on Multiphase Production Technology*, 2007.

[27] P. Y. Lin and T. J. Hanratty, "Prediction of the initiation of slugs with linear stability theory," *Int. J. Multiph. Flow*, vol. 12, no. 1, pp. 79–98, 1986.

[28] H. GU and L. GUO, "Experimental Investigation of slug development on horizontal two-phase flow," *Chinese J. Chem. Eng.*, vol. 16, no. 2, pp. 171–177, 2008.

[29] R. I. Issa, S. Barbeau, C. P. Hale, U. Odozi, G. F. Hewitt, S. M. Richardson, and W. L. Wong, "Measurement and prediction of slug characteristics in three-phase flows," in *13th International Conference on Multiphase Production Technology*, 2007.

[30] D. Barnea, O. Shoham, Y. Taitel, and A. E. Dukler, "Gas-liquid flow in inclined tubes: flow pattern transitions for upward flow," *Chem. Eng. Sci.*, vol. 40, no. 1, pp. 131–136, 1985.

[31] Y. Taitel and A. E. Dukler, "A model for predicting flow regime transitions in horizontal and near horizontal gas-liquid flow," *AIChE J.*, vol. 22, no. 1, pp. 47–55, 1976.

[32] J. Brill, S. Zelimir, W. Coberly, J. Herring, and D. Moore, "Analysis of two-phase tests in large-diameter flow lines in Prudhoe Bay field," *Old SPE J.*, vol. 21, no. 3, pp. 363–378, 1981.

[33] S. L. Scott, "Modeling slug growth in pipelines," Tulsa Univ., OK (USA), 1987.

[34] M. L. Zoeteweij, "Long liquid slugs in horizontal tubes: development study and characterisation with

electrical conductance techniques," Ph.D Thesis, Delft University of Technology, Netherlands, 2007.

[35] Z. Schmidt, J. P. Brill, and H. D. Beggs, "Experimental study of severe slugging in a two-phase-flow pipeline-riser pipe system," *Old SPE J.*, vol. 20, no. 5, pp. 407–414, 1980.

[36] P. Y. Lin and T. J. Hanratty, "Effect of pipe diameter on flow patterns for air-water flow in horizontal pipes," *Int. J. Multiph. Flow*, vol. 13, no. 4, pp. 549–563, 1987.

[37] P. Y. Lin and T. J. Hanratty, "Detection of slug flow from pressure measurements," *Int. J. Multiph. Flow*, vol. 13, no. 1, pp. 13–21, 1987.

[38] J. Fabre, L. Peresson, J. Corteville, R. Odello, and T. Bourgeois, "Severe slugging in pipeline/riser systems," *SPE Prod. Eng.*, vol. 5, no. 3, pp. 299–305, 1990.

[39] O. N. Nwoke, I. P. Okokpujie, and S. C. Ekenyem. "Investigation of Creep Responses of Selected Engineering Materials." *Journal of Science, Engineering Development, Environmen and Technology (JOSEDET)* 7, no. 1 (2017): 1-15.

[39] A. B. Ehinmowo, A. T. Ogunbiyi, O. D. Orodu, D. S. Aribike, and A. O. Denloye, "Experimental investigation of hydrodynamic slug flow in pipeline-riser systems," *Int. J. Appl. Eng. Res.*, 2016.

[40] S. F. Ali, "Two-phase flow in a large diameter vertical riser," Cranfield University, Bedford, Uk, 200.

An Open Access Journal Available Online

Effects of Mycobacterium Tuberculosis Macrophage Interaction: Surface Energetic Mechanism

[1*]Chukwueneke J. L., [2]Chukwujike I. C., [3]Sinebe J. E., [4]Ugwuegbu C. D.

[1]Department of Mechanical Engineering,
Nnamdi Azikiwe University, Awka, Nigeria.
[2]Department of Polymer & Textile Engineering,
Nnamdi Azikiwe University, Awka, Nigeria.
[3]Department of Mechanical Engineering,
Delta State University, Oleh, Nigeria.
[4]Department of Mechanical Engineering,
Federal Polytechnic, Nekede, Nigeria.

Abstract─ The mechanisms effects of mtb – macrophage using surface energetic in determining the interaction processes with the surface interfacial energies explained using van der Waals concept of particle – particle interactions. The Lifshitz derivations for van der Waals forces were applied as an alternative to the contact angle approach which has been widely used in other biological systems. The methodology involved taking sputum samples from twenty infected persons and from twenty uninfected persons for absorbance measurement using a digital Ultraviolet visible Spectrophotometer. Matlab software tools were used in the mathematical analysis of the data generated from the absorbance values. The values of $A_{132abs} = 0.21631 \times 10^{-21}$Joule (for mtb infected sputum) and $\tilde{A}_{132abs} = 0.18825 \times 10^{-21}$Joule (for mtb/HIV infected sputum) were obtained. The free energies of adhesion calculated were found to be negative with combined Hamaker coefficient positive. The implication of this result is the positive value of the absolute combined Hamaker coefficient which entails net positive van der waals forces demonstrating an attraction between mtb and the macrophage. This however, implies that infection is very likely to occur. It was also shown that in the presence of HIV, the interaction energy is reduced by 13% confirming adverse effects observed in HIV patients suffering from tb. Negative Hamaker coefficient (-0.22669×10^{-19}mJ/m^2) indicated that separation of mtb is practical. The condition was sought for repulsion to occur and that

condition was based on the value of A_{33} that would render the absolute combined Hamaker coefficient A_{131abs} negative. Mathematically it was derived as $A_{33} \geq 0.9527 \times 10^{-21}$ Joule which satisfies this condition for negative A_{132abs}. To achieve the condition of A_{33} above, possible additive(s) in form of drugs to the sputum should be required.

Keywords- Absorbance; surface energetics; hamaker coefficient; macrophage; mycobacterium tuberculosis; van der waals forces; wavelength.

I. Introduction

Tuberculosis, tb, is an airborne disease caused by the bacterium mycobacterium tuberculosis, mtb. This causative agent of tb is one of the world's most destructive human pathogens. The infectious bacteria is transmitted through air and most commonly affects the lungs, but can also attack other parts of the body, such as the brain, spine or kidneys, which is responsible for more than 75% of cases (Aandahl, 2012).

The World Health Organization, WHO, declared tb as a global emergency in 1993. Unfortunately, the efforts made by the discontinue tb strategy were not enough to impede the occurrence of 1.3 million deaths in 2009 (WHO, 2010). However, WHO estimates that the number of cases per capita peaked at 2004 and is slowly falling (WHO, 2012). Nonetheless, the battle against tb is far from being over, since mtb (the main causative agent of tb) proved to be highly adaptive (Kumar and Rao, 2011) and capable of evading the current strategies for treatment of about half million cases of multi-drug-resistant tb (MDR-tb) that were reported in 2007, including cases of extensively drug-resistant tb (XDR-tb) (WHO, 2012), and the more recently reported totally drug-resistant strains (TDR-tb) (Kumar and Rao, 2011; Velayati et al, 2009).

Several researchers so far have reported the occurrences of tb cases, a fussy report surveyed that only 35 out of 134 countries showed declination of cases of about 5% per year based on per capita rate (Lonnroth et al, 2009). This review considered the data from 1998 – 2007. Different surveillance analysis and mathematical modeling studies recommended reduction of tb incidences per capita is around 1% per year, further suggesting diminution of cases by 2015 (Adeeb et al, 2013). The world population growth has being predicted approximately 2% per year; this may be an important reason for increment of tb cases (WHO, 2012). All these preceding reports showing the presence of lacunae in the existing management approaches for tb and the inadequate effectiveness of public health systems, with particular reference to underdeveloped countries. In malice of the availability of anti-tb drugs developed over the last five decades, one-third of the world's population retains a dormant or latent form of mtb (Corbett et al, 2003).

Much research has been and is still on, on the subject with a cure not yet in view. The role of surface properties in this biological process will be established. Surface energetic approach is a very important

thermodynamics tool used in determining the absolute and combined Hamaker coefficients of mtb – macrophage interaction processes (Chukwuneke et al, 2017). The Lifshiftz derivation for van der Waals forces is used to model the interaction and the surface energies and surface free energies of adhesion obtained by this method will be used to predict the nature of surface interactions between two solid particles suspended in a liquid medium.

It is a well-known fact that surface property determination of interacting particles lead to the further understanding of the mechanism of interactions. A common area of contact is established once two particles meet each other. In such process, a certain portion of each particle gets displaced through work (Chukwuneke et al, 2016). The work responsible for the displacement of a unit area is known as surface free energy. The consecutive impact on the surface is known as surface energetic effects. To attain the equilibrium such impacts are changed in a slow pace. In this particular study similar concepts have been implemented to characterize the mtb – macrophage interactions with the sputum as the intervening medium.

In this paper, mtb is conceptualized as particle dispersed in a liquid medium "sputum" and interacting with another particle "macrophage". The bacterium attaches itself on the surface of the macrophage cell before penetrating and attacking it. If the surface of the macrophage cell is such that it will repel the bacteria, access of the bacteria into the alveoli of the cell would have been denied. Thus the initial actions actually take place on the surface of the cell and of the bacteria. It is alongside this background that this paper surveys a novel and exceptional approach using interfacial free energy approach to search for a way forward in the research on the topic of mtb – macrophage interaction mechanisms.

II. Methodology

The methodology of this paper involved sputum sample collection, mycobacterium and macrophages structural studies, mtb screening, and the study of the mechanism of interactions of the bacterium and the macrophage. Twenty samples each of infected, uninfected and *mtb*/HIV co-infected sputum were collected. Each specimen was screened to determine the infection status using GeneXpert and Ziehl-Neelsen staining method. The slides were prepared and the absorbance, ā, values of each specimen, for wavelength range of 230–950nm were measured using digital Ultraviolet Visible Spectrophotometer. The data generated and the various equations governing the relationship among the variables were used in calculating values for the reflectance, R, transmittance, T, refractive index, n, and the dielectric constant, ε. MatLab software tools were employed in the mathematical analysis of the data generated from the absorbance values.

III. Thermodynamic Mechanism of Interactions

Suppose in a certain case, the bacterium, *mtb* has been considered as a particle coming in the surrounding area of the macrophage which is further considered as another

particle. In the consecutive step, the bacterium attaches itself on the surface of the macrophage under a

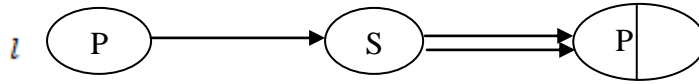specific condition where the macrophage is dispersed in sputum medium (see figure 1).

Figure 1: Conceptual representation of *mtb* – macrophage adhesion process

Expression of the thermodynamic free energy associated with adhesion process provided in figure (1) is represented as follows (Omenyi, 1978; Visser, 1981):

$$\Delta F_{pls}^{adh}(d_o) = \gamma_{ps} - \gamma_{pl} - \gamma_{sl} \quad (1)$$

Equation (1) represents the integrated free energy of adhesion considered from infinity to the equilibrium where separation distance is d_o. In this equation, P, S represents bacteria and macrophage respectively and L signifies the sputum medium. In the right hand side of the equation, γ_{ps} expresses the interfacial free energy between P and S. γ_{pl} represents the same for P and L, whereas, γ_{sl} provides the same information between S and L.

Successful bacterial penetration in the macrophage cells will occur through the engulfment of the bacteria requiring net free energy, represented as (Omenyi, 1978; Chukwuneke et al, 2015):

$$\Delta F_{NET} = \gamma_{ps} - \gamma_{pl} < 0 \quad (2)$$

ΔF^{adh} can be determined by several approaches, apart from the above surface free energy approach. The classical work of (Hamaker, 1937) is very appropriate.

A system containing two planes could be considered for computing the free energy of interaction (Hamaker, 1937):

$$\Delta F_{132}(d_o) = \left[-\frac{A_{132}}{12\pi d_o^2} \right] \quad (3)$$

In this, A_{132} refers to the Hamaker coefficient for a respective system. Considering nominal isolation distance d_0, and equation (3) as valid for such a small distance, the Hamaker coefficient should be expressed:

$$A_{132} = -12\pi d_o^2 \Delta F^{adh}(d_o) \quad (4)$$

Following Lifshitz theory, the Hamaker coefficient A_{132} is represented as follows (Lifshitz, 1961):

$$A_{ikj} = \frac{3}{4}\pi\hbar \int_0^\infty \left[\frac{\varepsilon_i(i\zeta) - \varepsilon_k(i\zeta)}{\varepsilon_i(i\zeta) + \varepsilon_k(i\zeta)} \right]\left[\frac{\varepsilon_j(i\zeta) - \varepsilon_k(i\zeta)}{\varepsilon_j(i\zeta) + \varepsilon_k(i\zeta)} \right] d\zeta \quad (5)$$

Where, $\varepsilon_j(i\zeta)$ refers to the dielectric constant of a specific material j, this is considered through the imaginary i, frequency axis, $(i\zeta)$, $\hbar$ is planck's constant.

In this context, the evaluation of equation (5) should result in equivalent value with the thermodynamic free energy of adhesion, provided in equation (1).

Thus, the Hamaker coefficient and the interfacial free energies are connected through the following equation:

$$A_{pls} = -12\pi d_o^2 (\gamma_{ps} - \gamma_{pl} - \gamma_{sl}) \quad (6)$$

This equation has been derived through combining equation (4) with equation (1). For the issue of self-interaction of a particle equation (7) should be considered:

$$A_{ij} = \frac{3}{4}\pi\hbar \int_0^\infty \left[\frac{\varepsilon_i(i\zeta) - \varepsilon_j(i\zeta)}{\varepsilon_i(i\zeta) + \varepsilon_j(i\zeta)}\right]^2 d\zeta \tag{7}$$

To determine the Hamaker coefficients using the Lifshitz theorem of equation (7), there is a need to evaluate the dielectric constant ε. From the information of light absorbance, reflection and transmittance, it could be seen that:

$$\bar{a} + T + R = 1 \tag{8}$$
$$T = \exp^{-\bar{a}} \tag{9}$$

Where; $\bar{a}$ is absorbance, T is transmittance, and R is reflectance.

A value for the refractive index, n is obtained by employing the mathematical relation (Robinson, 1952):

$$n = \left[\frac{1 - R^{\frac{1}{2}}}{1 + R^{\frac{1}{2}}}\right] \tag{10}$$

A value for the extinction coefficient, k is obtained using:

$$k = \left[\frac{\alpha\lambda \times 10^{-9}}{4\pi}\right] \tag{11}$$

Where; α is the absorption coefficient defined as follows:

$$\alpha = \left[\frac{\bar{a}}{\lambda \times 10^{-9}}\right] \tag{12}$$

The dielectric constant, ε could thus be given by (Charles, 1996);
For the real part:
$$\varepsilon_1 = n_1^2 - k^2 \tag{13}$$
For the imaginary part:
$$\varepsilon_2 = 2n_2 k \tag{14}$$

With these values, it is possible to determine A_{ij} using the relevant equations to determine A_{11}:

$$A_{11} = 2.5\left[\frac{\varepsilon_{10} - 1}{\varepsilon_{10} + 1}\right]^2 = 2.5\left[\frac{n_1^2 - 1}{n_1^2 + 1}\right]^2 \tag{15}$$

This gives a value to the Hamaker constant A_{11}, and by extension to other Hamaker constants A_{22} and A_{33}. For combination of two different materials 1 and 2 in approximation:

$$A_{12} = \sqrt{A_{11}A_{22}} \tag{16}$$

For a combination of two disimilar materials (i.e. macrophage, 1 and the bacteria, 2) with the gap between 1 and 2 filled with sputum as the medium 3, the combined Hamaker coefficient will be given by:

$$A_{132} = A_{12} + A_{33} - A_{13} - A_{23} \tag{17}$$
$$A_{131} = A_{11} + A_{33} - 2A_{13} \tag{18}$$

Therefore, the system under consideration follows equations (17) and (18):

Rewriting these equations will give:

$$A_{132} = \left(\sqrt{A_{11}} - \sqrt{A_{33}}\right)\left(\sqrt{A_{22}} - \sqrt{A_{33}}\right) \tag{19}$$
$$A_{131} = \left(\sqrt{A_{11}} - \sqrt{A_{33}}\right)^2 \tag{20}$$

Equation (20) shows that, for a three-component system involving three different materials, 1, 2 and 3, A_{132} can become negative:

$$A_{132} < 0 \tag{21}$$

When;

$$\sqrt{A_{11}} > \sqrt{A_{33}}$$
$$\text{and } \sqrt{A_{22}} < \sqrt{A_{33}} \tag{22}$$

A_{33} = Hamaker constant for sputum;
A_{13} = Hamaker constant between both materials (i.e. *mtb* and sputum);
A_{23} = Hamaker constant between both materials (i.e. macrophage and sputum).

Thus the Hamaker Coefficient A_{132} becomes:

$$A_{132} = \frac{3}{4}\pi\hbar \int_0^\infty \left[\frac{\varepsilon_1(i\zeta) - \varepsilon_3(i\zeta)}{\varepsilon_1(i\zeta) + \varepsilon_3(i\zeta)}\right]\left[\frac{\varepsilon_2(i\zeta) - \varepsilon_3(i\zeta)}{\varepsilon_2(i\zeta) + \varepsilon_3(i\zeta)}\right] d\zeta \tag{23}$$

Integrating all the values of the combined Hamaker coefficient, A_{132}

gives an absolute value for the coefficient denoted by A_{132abs} and applying Lifshitz derivation for van der Waals forces as in equation (23).

IV. Results and Discussion

The absorbance values were obtained as a function of wavelength and summarized in Table 1. It could be seen that the peak absorbance values of the various sputum samples and components vary in magnitude revealing the notable effect of the bacteria on them. The comparison

between the positive and negative samples of the macrophages is imperative to this research. This is because mtb actually attacks the macrophages by attaching itself to the macrophage cells. Figure 2 reveals the disparity between the peak absorbance values of *mtb/HIV* positive and negative sputum samples respectively, and this shows an indication of how the bacteria affect the properties of sputum.
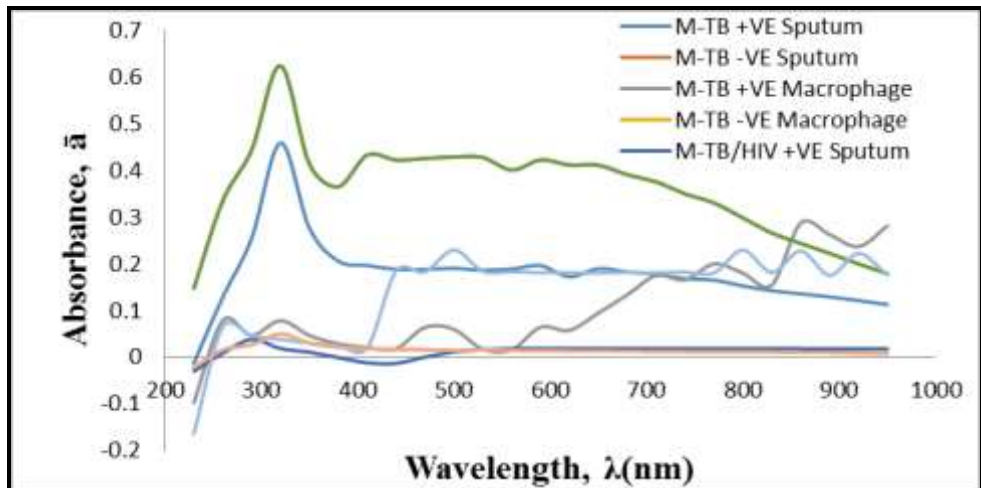
Figure 2: Variation of Average Absorbance, *ā* with Wavelength, *λ* for *mtb*, *mtb/HIV* Sputum and *mtb*, *mtb/HIV* Macrophages

Table 1: Comparison between Peak Absorbance values of *mtb* Positive, *mtb/HIV* Positive and Negative Sputum Components respectively

Sample Type	Wavelength, λ(Å) Peak Values	Absorbance, ā Peak Values				
		M-TB Positive	**M-TB Negative**	**M-TB/HIV Co-infected**	**M-TB/HIV Uninfected**	**Mean Values**
Sputum	320	0.2918 – 0.7877	---	---	---	0.4588±0.1468
		---	0.2657 – 1.2501	---	---	0.6244±0.3545
	290	---	---	0.0231 – 0.0498	---	0.0379±0.0108
		---	---	---	0.2657 – 1.2501	0.6244±0.3545
o p	3 2 0	0.0206 –	---	---	---	0.0496±0.

		0.0736				0116
		---	0.0478 – 0.1148	---	---	0.0784±0.0206
	290	---	---	0.0152 – 0.0637	---	0.0456±0.0106
		---	---	---	0.0478 – 0.1148	0.0784±0.0206

Figure 2 shows a peak absorbance value of greater than 0.60 and 0.45 for *mtb* negative and positive sputum respectively and a peak absorbance value of greater than 0.07 and 0.04 for *mtb* positive and negative macrophages respectively were recorded at wavelength of 320nm. This peak values falls within the visible range of ultraviolet radiation which is between 300 – 600nm. This is important as a reference point in the study of the infection mechanism and may be of importance in determining the critical Hamaker coefficient that favours repulsion between the bacterium and the macrophage. It could be well-known that the infected *mtb* sputum has lower absorbance values than the uninfected ones.

The absorbance values of both the *mtb* positive and negative Macrophages were increasing with increase in wavelength. This may be explained away by the fact of a higher energy level of these cells. The *mtb* infected macrophages gave higher absorbance values than the *mtb* uninfected macrophages. This is a clear indication that infection had occurred and shows the alteration in absorbance values due to *mtb* infection.

The absorbance of the *mtb/HIV* co-infectious sputum samples systematically increased as the wavelength increased until a critical wavelength of 290nm, where peak absorbance values of greater than 0.60 and 0.06 for *mtb/HIV* negative and positive sputum respectively were accomplished. The trend here shows that the uninfected sputum reveals a higher absorbance values at all wavelengths. This indicates that a shift in the energy equation of the system is tenable by some alteration to the sputum as an intervening medium in the *mtb/HIV* – macrophage interaction. It then suggests a possibility of attaining repulsion between the *mtb/HIV* and the macrophage cells by some additives to the sputum.

The absorbance values of the *mtb/HIV* positive macrophages were increasing with increase in wavelength. The *mtb/HIV* co-infected macrophages also gave higher absorbance values than the uninfected ones at wavelengths greater than 400nm. This may explain away by the fact of a higher energy level of these cells. This is a clear indicator that bacteria ingestion had occurred and shows the alteration in absorbance values due to *mtb/HIV* infection.

The trend is such that the mean absorbance peak values of mtb negative sputum samples are reduced by infection from 0.6244 ± 0.3545 to 0.4588 ± 0.1468 (see table 1) by a factor of about 26.5%. In mtb macrophage samples, the reduction is from 0.0784 ± 0.0206 to $0.0496\pm$

0.0116, a factor of about 36.7%. While in mtb/HIV co-infected macrophage samples, the reduction is from 0.0784± 0.0206 to 0.0456± 0.0106 by a factor of about 41.8%. Comparing the mean absorbance peak values of mtb positive sputum samples and the mean absorbance peak values of mtb/HIV co-infected sputum samples; the results of the mean absorbance peak values reveal that the mean absorbance peak value of the mtb/HIV co-infected samples is generally reduced as compared to that of the mean absorbance peak values of the mtb positive sputum samples (Table 1).

Equation (7) was used to obtain for each interacting system, $A_{ij}(A_{11}, A_{22}, A_{33}, A_{12}, A_{13}, A_{23})$ by approximate change of variables. MatLab computation tools were used. This involved the numerical integration of equation (7) for each wavelength from 230 to 950 for all the twenty samples in each category. Applying Lifshitz derivation for van der Waals forces as in equation (23), The absolute value for the Hamaker coefficient could be derived by obtaining the mean of all the A132, A131, and A232 values got from the Lifshitz relation.

Table 2: Values of the Hamaker Constants and Hamaker Coefficients for the Infected and Uninfected

Variable (x10^-21 Joule)	M-TB Samples				M-TB/HIV Samples			
	Infected Sputum		Uninfected Sputum		Infected Sputum		Uninfected Sputum	
	Peak Value	Absolute Value	Peak Value	Absolute Value	Peak Value	Absolute Value	Peak Value	Absolute Value
A_{11}	---	---	1.1328	0.9418	---	---	1.1328	0.9418
A_{22}	1.2134	0.9606	---	---	1.0267	0.9786	---	---
A_{33}	0.4205	0.2307	0.6701	0.4247	0.5962	0.2881	0.6701	0.4247
A_{132}	0.5187	0.2163	---	---	0.4253	0.1883	---	---
A_{131}	---	---	0.2241	0.1016	---	---	0.2241	0.1016

A_{232}	0.6298	0.2498	⋮	⋮	0.5014	0.2047	⋮	⋮

Table (2) show the comparison of the Hamaker constants and coefficients for the positive and negative sputum samples. A_{11} is Hamaker constant for the uninfected sputum samples. A_{22} is the Hamaker constant for the *mtb*, here represented by the infected macrophage. This is as a result of no known process of isolation of the *mtb* at the moment. This is a very close approximation for the bacteria owing to the manner of the infection mechanism. The Hamaker constants A_{33} for the sputum show greater values for the uninfected samples which regularly indicate a higher surface energy than the infected samples. The higher absolute values of A_{132} and A_{232} as against that of A_{131}, as well as the lower value of the absolute combined Hamaker coefficient A_{131abs} for the uninfected samples is a clear suggestion of the relevance of the concept of Hamaker coefficient in the M-TB infection process. The surface energy A_{131} of the macrophages is less than the surface energy A_{232} of the bacteria (*mtb*).

Table (2) shows the comparison of the Hamaker constants and coefficients for the positive and negative sputum samples. $\tilde{A}_{11}$ is Hamaker constant for the uninfected sputum samples. $\tilde{A}_{22}$ is the Hamaker constant for the *mtb/HIV* co-infection, here represented by the infected macrophage. This is as a result of no known process of isolation of the *mtb/HIV* co-infection at the moment. Though, this is a very close approximation for the bacteria owing

to the manner of the infection mechanism. The Hamaker constants $\tilde{A}_{33}$ for the sputum show greater values for the uninfected samples which regularly indicate a higher surface energy than the infected samples. The higher absolute values of $\tilde{A}_{132}$ and $\tilde{A}_{232}$ as against that of $\tilde{A}_{131}$, as well as the lower value of the absolute combined Hamaker coefficient $\tilde{A}_{131abs}$ for the uninfected samples is a clear suggestion of the relevance of the concept of Hamaker coefficient in the *mtb/HIV* co-infection process. The surface energy $\tilde{A}_{131}$ of the macrophages is less than the surface energy $\tilde{A}_{232}$ of the bacteria (*mtb*).

A_{33}, which serves as the energy of sputum as an intervening medium, is seen in *mtb* data to be reduced by infection from 0.4247 $x10^{-21}$J to 0.23067 $x10^{-21}$J by a factor of about 45.7% (see table 2). In *mtb/HIV* co-infection, the reduction is from 0.4247 $x10^{-21}$J to 0.28812 $x10^{-21}$J, a factor of about 32.2% (see table 2).

The reduction is lower in *mtb/HIV* co-infection probably because of the interaction between *HIV* and *tb*. For the combined Hamaker coefficient, the value is 0.21631 $x10^{-21}$J for *mtb* and 0.18825 $x10^{-21}$J for *mtb/HIV*. This result is as expected. *HIV* has the tendency to reduce the energy on the surface of a given material, in this case by about 13%, conforming adverse effects observed in HIV patients with tuberculosis. Note that the values of A_{132} are all positive showing that attraction exists between the macrophage and the *mtb*

particles. The effect of the infection can only be abated if a drug, in the form of additive is added that can change the value of A_{132} to negative under that condition, mutual

.

repulsion will occur and it will be expected that, in principle, the *tb* bacteria will not attack the macrophage
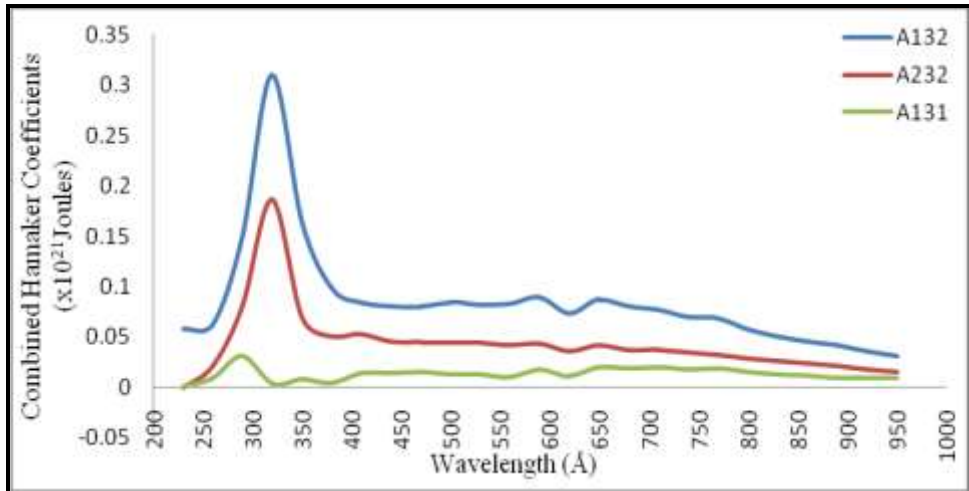

Figure 3: Variation of Average Combined Hamaker Coefficients, A_{132} A_{131} and A_{232} with Wavelength, λ (nm) for the *mtb* infected Sputum Samples

Figure (3) reveals the pattern of the average combined Hamaker coefficients, A_{132}, A_{131} and A_{232} for the sputum samples with clear peak values occurring at various wavelengths. The peak average values of A_{132} and A_{232} occur at wavelength of 320nm with values of 0.30968 $x10^{-21}$J and 0.18609 $x10^{-21}$J respectively, while the peak average value of A_{131} occurs at wavelength of 290nm with value of 0.03074 $x10^{-21}$J. Energy level increases in average combined Hamaker coefficients, A_{132} and A_{232} which is the infected Hamaker coefficients as against the decreased energy level of the uninfected average combined Hamaker coefficient, A_{131}. This is quite a significant phenomenon which explains away the fact of the effect of co-infection.

Table (2) reveal that the surface energy of the macrophages as computed in terms of Hamaker coefficients is less than the surface energy of the *mtb*, *mtb/HIV*. This result also shows that the surface energy of the *mtb/HIV* macrophage is less than that of *mtb* macrophage. *HIV* has the tendency to reduce the energy with the consequence of increased viral loads and decreased immune systems. *tb* is an opportunistic disease and in presence of *HIV*, the consequence is dreadful. Hence for $A_{132} > 0$, $A_{131(macropage)} < A_{232(mtb/HIV)}$.

The mean of all values of A_{11} and A_{22} could be obtained and substituted into equation (19) in order to derive a value for A_{33} at which A_{132} is equal to zero in agreement with the earlier stated reasons. Rearranging equation (19) and making A_{33} subject of the formula;

$$A_{33} = \left[\frac{2\sqrt{A_{11}}\sqrt{A_{22}} - A_{132}}{\sqrt{A_{11}} + \sqrt{A_{22}}} \right]^2 \quad (24)$$

The mean of all the values of A_{11} and A_{22} respectively gave the absolute values of the Hamaker constants as: $A_{11}= 0.94188 \times 10^{-21}$Joule and $A_{22} = 0.96068 \times 10^{-21}$Joule (for *mtb*); $\tilde{A}_{11}= 0.94188 \times 10^{-21}$Joule and $\tilde{A}_{22} = 0.97862 \times 10^{-21}$Joule (for *mtb/HIV* co-infection). Thus, inserting these values into equation (24) and rendering $A_{132} \leq 0$ will give the critical value of A_{33C} that satisfies the condition for the combined Hamaker coefficient to be equal to or less than zero. Hence any value of A_{33} greater than the critical would be the desired value necessary to attain a negative combined Hamaker coefficient.

Thus, the critical absolute Hamaker constant A_{33C} for the sputum which renders the A_{132} negative is given as: $A_{33C} = 0.9527 \times 10^{-21}$Joule (for *mtb*) and $\tilde{A}_{33C} = 0.9598 \times 10^{-21}$Joule (for *mtb/HIV* co-infection). Thus for negative combined Hamaker coefficient A_{132}, $\tilde{A}_{132}$ of the infected *mtb*, *mtb/HIV* sputum to be attained respectively, the combined Hamaker constant of the sputum as the intervening medium A_{33}, $\tilde{A}_{33}$ respectively should be of the magnitude: $A_{33C} \geq 0.9527 \times 10^{-21}$Joule and $\tilde{A}_{33C} \geq 0.9598 \times 10^{-21}$Joule respectively. Inserting the above values of A_{33}, $\tilde{A}_{33C}$ into equation (24) would yield negative values for A_{132}, $\tilde{A}_{132}$ respectively as follows: $A_{132} = -0.22669 \times 10^{-25}$Joule (when $A_{33} = 0.9527 \times 10^{-21}$Joule) and and $\tilde{A}_{132} = -0.08786 \times 10^{-25}$Joule (when $A_{33} = 0.9598 \times 10^{-21}$Joule).

Table 3: Computation of the values of Surface Free Energy γ_{sv} of the *mtb and mtb/HIV* Infected and Uninfected Sputum and Change in free energy of adhesion, ΔF^{adh} (mJ/m^2)

Variable	Infected Sputum		Uninfected Sputum		Variable	Hamaker constant, A ($\times 10^{-14}$ mJ)	ΔF^{adh} (mJ/m^2)
	Hamaker constant, A ($\times 10^{-14}$ mJ)	γ_{sv} (mJ/m^2)	Hamaker constant, A ($\times 10^{-14}$ mJ)	γ_{sv} (mJ/m^2)			
A_{11}	---	---	0.94188	37.7	A_{132}	0.21631	-17.3
A_{22}	0.96068	38.5	---	---	A_{131}	0.10165	-8.1
A_{33}	0.23067	9.2	0.42470	17.0	A_{232}	0.24986	-20.0
$\tilde{A}_{11}$	---	---	0.94188	37.7	$\tilde{A}_{132}$	0.18825	-15.1
$\tilde{A}_{22}$	0.97862	39.2	---	---	$\tilde{A}_{131}$	0.10165	-8.1
$\tilde{A}_{33}$	0.28812	11.5	0.42470	17.0	$\tilde{A}_{232}$	0.20474	-16.4

Since the surface energy is a measure of workdone on the surface. Table 3 shows the surface energy of the *mtb* is greater than the surface energy of the sputum. Also, the surface energy of the uninfected sputum 17.0mJ/m2 was apparently reduced to 9.2mJ/m2 when *mtb* attacked the human system. Consequently, the disease incidence lowers the surface energy of the infected sputum as shown in table 2.

This in effect indicates that *mtb* has a surface energy reducing capacity. Table 3 shows that the surface energy of the *mtb/HIV* is greater than the surface energy of the sputum. Also, the surface energy of the uninfected sputum 17.0mJ/m2 was in fact reduced to 11.5mJ/m2 when *mtb/HIV* co-infection attacked the human system. As a result, the bacteria incidence lowers the surface energy of the infected sputum. This in effect indicates that *mtb/HIV* has a surface energy reducing capacity tending to make the surface of the bacteria (sputum) more hydrophobic. From table 3; the following deductions are made: Surface free energies of infected sputum components are lower than the uninfected, *mtb* infection has the surface energy reducing capacity (i.e. reduces the work done on the surface), It is well identified that *mtb/HIV* attacks the macrophage; the reduction (difference on infected and uninfected) in surface free energies of Sputum could be as a result of its presence in the sputum.

The surface free energies described in table 3 are used to determine the free energy of adhesion. When the change in free energy of adhesion is negative; adhesion is thermodynamically favorable. Adhesion is therefore governed by attractive van der Waal forces. When *mtb* or *mtb/HIV* co-infection affixes itself to the surface of the macrophage in a liquid medium, there is the tendency of the bacteria to be engulfed by the macrophage cells causing their destruction. Thus increased adhesion may lead to more depletion of macrophage cells. The adhesion of the bacteria on the cell

will lead to penetration into the macrophage. Such a penetration will cause replication of bacteria and destruction of macrophage. What is required is for this attachment not to occur. Results obtained (Table 3) give the following deductions: The change in free energies of adhesion is all negative indicating that the net van der Waals forces are attractive; the change in free energies of adhesion is higher for infected *mtb/HIV* than infected *mtb*. In order words, presence of *HIV* increases the change in free energy of adhesion and hence tendency for increased attack, Hamaker coefficients are all positive suggesting van der Waals forces are attractive as negative free energy of adhesion.

V. Conclusion

The absolute Hamaker coefficient A_{131}=0.10165x10^{-21}Joule gives the interaction energy among the macrophage cells in the sputum while A_{232} is the interaction energy among the *mtb* particles in the sputum. A_{232} for *mtb/HIV* co-infection is less than that for *mtb* alone. Reduction in energy in the presence of HIV confirms the adverse effect when *mtb* and HIV occur simultaneously in a patient. This is so since a positive Hamaker value for any interacting system implies an attraction between the interacting bodies or particles while a negative Hamaker coefficient means repulsive van der Waals forces hence the interacting bodies would repel each other. The importance of negative Hamaker coefficient $(-0.2267x10^{-19}$mJ/m$^2)$ indicated that separation of bacteria is realistic. The desired outcome is that the bacteria do not adhere to the macrophage cells to avoid

penetration, in which case a condition for rendering combined Hamaker coefficient negative is required. Thus, a condition was required for repulsion to occur and that condition was based on the value of A_{33} that would render the absolute combined Hamaker coefficient A_{132abs} negative. A model for the infection mechanism was built-up employing the principle of particle – particle interaction. Mathematically, it was derived as

$A_{33} \geq 0.9527 x 10^{-21}$ Joule which satisfies this condition for negative A_{132abs}. To achieve the condition of A_{33} above, possible additive(s) to the system (in form of drugs) to the sputum as intervening medium should be required. That, as expected, may be the much desired way out for drug resistant strains of the *mtb* bacteria.

References

[1] Aandahl R. Z., Reyes F. J., Sisson A. S., Tanaka M. M. (2012). A model-Based Bayesian Estimation of the Rate of Evolution of VNTR Loci in Mycobacterium tuberculosis. *PLoS Comput. Biol.* 8(6): 1 – 9.

[2] Adeeb S., Gauhar R., Mazhar U., Waleed A. K., Young S. L., (2013). Challenges in the development of drugs for the treatment of tuberculosis. *The Brazilian journal of infectious diseases,* 17(1): 74 – 81.

[3] Charles, Kittel, (1996): Introduction to Solid State Physics, 7th Ed., John Willey and sons Inc. New York. 308.

[4] Chukwuneke J. L., Chukwuneke P. C., Okolie P. C., Sinebe J. E. (2016). Hamaker Coefficient Concept: The Application to the Mycobacterium Tuberculosis – Macrophage Interactions Mechanism. *Advances in Bioscience and Bioengineering*, 4(1): 1 – 20.

[5] Chukwuneke J. L., Achebe C. H., Ejiofor O. S. and Sinebe J. E. (2015). Surface Energetics of Mycobacterium Tuberculosis – Macrophage Interactions. *Journal of Biomedical Engineering and Medical Imaging,* 2(6): 49 – 61.

[6] Corbett E. L., Watt C. J., Walker N., Maher D., Williams B. G., Raviglione M. C., Dye C. (2003). The growing burden of tuberculosis: global trends and interactions with the HIV epidemic. *Arch. Int. Med.*, 163(9): 1009 – 1021.

[7] Hamaker H C (1937) The London–van der Waals attraction between spherical particles. *Physica* 4: 1058 – 1072.

[8] Jeremiah CL, Chinonso AH, Jude SE, Duke UC (2017) Surface Energetic Effects of Human Immunodeficiency Virus Co-Infection on Mycobacterium Tuberculosis-Macrophage Interaction Mechanism. J. Appl. Biotechnol. Bioeng. 3(6): 1 – 8.

[9] Kumar D., Rao K. V. S., (2011). Regulation between Survival persistence. *Microbes infect.*, 13: 121 – 133.

[10] Lonnroth K., Jaramillo E., Williams B. G. (2009). Drivers of tuberculosis epidemics: the role of risk factors and social determinants. *Soc. Sci. med.*, 68: 2240 – 2246.

[11] Omenyi S. N. (1978) Attraction and Repulsion of particles by

Solidification Fronts. PhD Dissertation, University of Toronto. p23, p33, p34.

[12] Robinson, T.S., (1952). Optical Constants by Reflection. *Proceedings of the Physical Society London* 65(11): B910.

[13] Velayati A. A., Masjedi M. R., Fernia P., Tabarsi P., Ghanavi J., Ziazarifi A. H., Hoffner S. E., (2009). Emergence of new forms of Totally drug-resistant tuberculosis or Totally drug-resistant Strains in Iran. *Chest.,* 136: 420 – 425.

[14] Visser, J., (1981). Advances in Interface Science, *Elsevier Scientific Publishing Company, Amsterdam,* 15: 157–169.

[15] World Health Organization (WHO), (2010). Global tuberculosis control: WHO report 2010, Geneva, Switzerland, WHO/HTM/TB/2010.7. *Retrieved* 24-11-13

[16] World Health Organization (WHO), (2012). Global tuberculosis report 2012. Geneva, Switzerland. http://www.who.int/tb/publications/factsheet_global.pdf. *Retrieved* 24-11-13.

An Open Access Journal Available Online

Numerical and Analytical Modeling of Solar for Chimney Combined Ventilation and Power in Buildings

Layeni A. T. [1], Nwaokocha C. N.*[1], Giwa S. O. [1], Olamide O. O.[1]

[1]Department of Mechanical Engineering,
Olabisi Onabanjo University, Ago Iwoye, Nigeria
* collinsnwaokocha@gmail.com, yomilayeni@gmail.com

Abstract- Analytical and numerical studies were carried out to investigate the performance of the combined solar chimney for power generating system and ventilation based on a developed mathematical model. Numerical solution of the problem was based on the continuity, momentum and energy equations for turbulent, steady-flow using k-ε model and the finite volume method using ANSYS Fluent CFD package. The analysis domain was a 2-D room of 4×4 m^2 with solar chimney of various dimension attached. The results obtained revealed that Chimney Height (CH), Collector Width (CW), Solar Heat Flux (SHF) and ambient wind speed were found to be the most important factors in the design of the SC. Results showed that the room mass flow rate increased from 1 kg/s with no wind effect to about 30 kg/s with induced wind of 1 m/s. The mass flow rate increased from about 6 to 9 kg/s at CH of 5 and 8 m respectively for no wind condition and SHF of 400 W/m^2. Power outputs were obtained for the average velocity of the chimney, collector area and chimney height. It was observed from results obtained from both the numerical and analytical analysis that power outputs of the power generating systems increases with increase in heat energy in the collector space area which is a function of the global solar radiation intensity, the collector area, and the chimney height. The power outputs results showed that with SHF of 400 W/m^2 for CH of 5 and 9 m were 33 and 85 W/m^2 respectively. The respective power output for SHF of 200 and 1,000 W/m^2 were 25 and 47 W/m^2. Furthermore, the optimum values of CH, CW and SHF were 5 m, 1 m and 417 W/m^2 respectively under no wind condition with room temperature of 300 K and chimney velocity 0.12 m/s. It was also observed that with the increase in the mass flow rate in the chimney, the ventilation requirements were adequately met.

Keywords: Solar collector; Chimney; Turbine generator; Power output, Ventilation.

I. Introduction

At the present stage of technology development fossil fuels are the main source of energy in the world. Current energy production from coal and oil is damaging to the environment and non-renewable, which necessitated the research into other sources of energy which are renewable. It is noted that inadequate energy supplies can lead to high energy costs which invariably leads to low standard of living as well as to poverty. There is therefore need for a switch to renewable sources of energy.

Renewable energy, according to Odai et al (2016) Renewable energy, is energy which comes from natural resources such as sunlight, wind, rain, tides, waves and geothermal heat, which are renewable. It is further reported according to the Renewables 2011 Global Status Report that about 16% of global final energy consumption comes from renewables, with 10% coming from traditional biomass, which is mainly used for heating, and 3.4% from hydroelectricity. New renewables (small hydro, modern biomass, wind, solar, geothermal, and biofuels) accounted for another 3% and are growing very rapidly. The share of renewables in electricity generation is around 19%, with 16% of global electricity coming from hydroelectricity and 3% from new renewables (Renewables 2011 Global Status Report).

According to current research, the use of wind power, widely used in Europe, Asia, and the United States, is increasing at an annual rate of 20%, with a worldwide installed capacity of 238,000 megawatts (MW) at the end of 2011. However, since 2004, photovoltaic passed wind as the fastest growing energy source, and since 2007 has more than doubled every two years. At the end of 2011 the photovoltaic (PV) capacity worldwide was 67,000 MW, and PV power stations are popular in Germany and Italy (Alex Morales, 2012; Renewable Energy, 2012).

Moreover, while many renewable energy projects are large-scale, renewable technologies are also suited to rural and remote areas, where energy is often crucial in human development. Climate change concerns, coupled with high oil prices, peak oil, and increasing government support, are driving increasing renewable energy legislation, incentives and commercialization in many developed and developing countries. New government spending, regulation and policies helped the industry weather the global financial crisis better than many other sectors. According to a 2011 projection by the International Energy Agency, solar power generators may produce most of the world's electricity within 50 years, dramatically reducing the emissions of greenhouse gases that harm the environment (Ben Sills, 2011; UNEP, 2007; Zhou, et al., 2007a).

Schlaich and Wolfgang (2000) in the Encyclopedia of Physical Science and Technology, Third Edition, stated that "Sensible technology for the use of solar power must be simple and reliable, accessible to the

technologically less developed countries that are sunny and often have limited raw materials resources, should not need cooling water or produce waste heat and should be based on environmentally sound production from renewable materials." This is where other technology of harnessing the solar energy is sought after, that will produce the required energy at a cost lower that of the PV solar energy technology. The solar chimney meets these conditions and makes it possible to take the crucial step toward a global solar energy economy. Schlaich and Wolfgang (2000) reported that Economic appraisals based on experience and knowledge gathered so far shown that even solar chimneys rated at 100 and 200 MW are capable of generating energy at costs comparable to those of conventional power plants. This is a major reason to develop this form of solar energy utilization further. In a future energy economy, solar chimneys could thus help assure economic and environmentally appropriate utilization of energy in sunny regions.

Another application of the solar chimney is in the area of ventilation systems for buildings. Natural ventilation of buildings can be achieved with solar-driven, buoyancy-induced airflow through the solar chimney channel. Gontikaki, et al (2010) noted that the exploitation of sustainable energy sources in relations to the functional demands of buildings (for heating, ventilation, cooling, etc.) can contribute significantly to energy savings in buildings, and thus to alleviating of the present environmental, economic and social problems related to conventional energy practices. Passive (natural) ventilation of buildings is a successful means to save energy otherwise consumed for mechanical ventilation and/or cooling which can be achieved successfully with the use of a solar chimney ventilation system (Gontikaki, et al., 2010).

Background

Solar Chimney Ventilation System

Chimneys or channels are used in various applications such as heating and ventilating of buildings, drying of agricultural products, and various other passive systems such as for cooling electronic components (Bar-Cohen and Krauss, 1988; Bilgen and Michel, 1979; Ekechukwa and Norton, 1999).

A Solar Chimney (SC) ventilation system differs from a conventional chimney in that at least one wall is made transparent; solar radiation enters the chimney through the glazed part and heats up the walls. The temperature of the air inside the SC channel rises due to heat transfer from the walls and the resulting buoyancy drives the airflow through the channel. The SC pulls air from the interior of the building, which is replaced by fresh air through openings or other paths, and natural ventilation is accomplished. Performance of the SC is primarily described by the induced ventilation flow rates; in case heat harvesting is also of interest, air temperature in the channel is the other important performance indicator (Gontikaki, et al., 2010; Hirunlabh, et al., 1999; Nouanégué and Bilgen, 2009; Schlaich and Wolfgang, 2000; Sudapom and Bundit, 2006).

Burek and Habeb (2007), in their report on an experimental investigation into heat transfer and mass flow in thermosyphoning air heaters, such as solar chimneys and Trombe Walls. Their principal results showed that the mass flow rate through the channel was a funct both the heat input and the ch...... depth given by

37

$m/Q^{0:572}$ and

$m/s^{0:712}$;

And that the thermal efficiency of the system (as a solar collector) was a function of the heat input, and not dependent on the channel depth given by
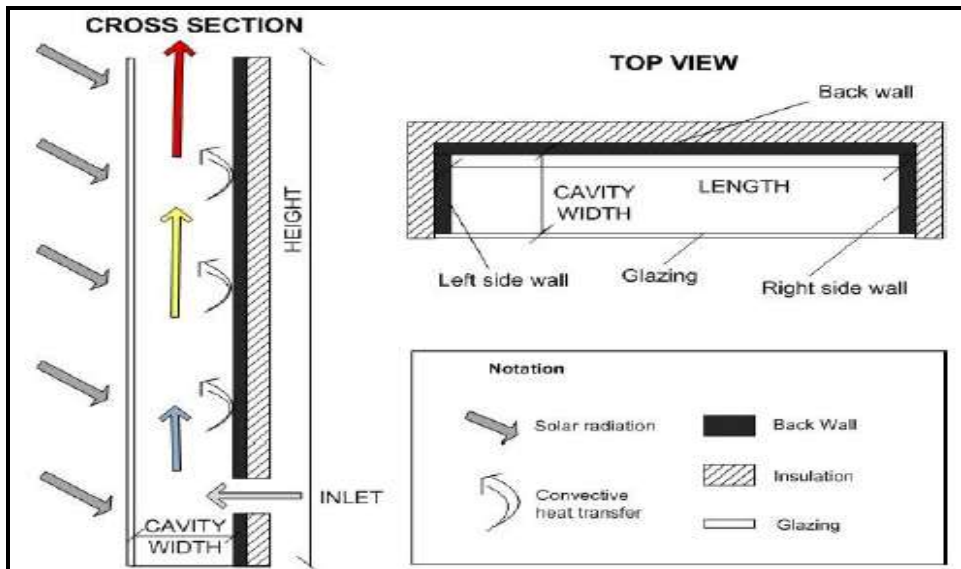
$h/Q_i^{0.298}$

Figure 1: Cross-Section and Top View of Solar Chimney

Nouanégué and Bilgen (2009), in their Numerical study by conjugate heat transfer carried out on solar chimney systems for heating and ventilation of dwellings, produced results showing that the surface radiation modifies the flow and temperature fields, affects the Nusselt number and the volume flow rate, both in a positive way, and improves the ventilation performance of the chimneys.

Zhou et al (2007a,b) studies a combined solar house with a solar chimney and a solar water collector. Theoretical analyses were carried out

to investigate natural ventilation in the solar house, compared with that in the individual chimney ventilation system under the same conditions. Their results showed that the proposed combined ventilation system improved the ventilation. When the mean solar radiation during a day from 8:00 to 18:00 h is 550 Wm^{-2}, the mean airflow rate in the combined ventilation system reaches 0-32 m/s, which is 18.5% higher than that (0.27 m/s) in the individual chimney ventilation system under the same conditions. Furthermore, results showed that the effect of night

ventilation on the combined solar house is better, although less energy is drawn out from the room by comparing chimney airflow temperatures and rates when the dampers are open after 18:00 hour, with those when the dampers are open day and night.

Gontikaki et al (2010) in their report stated their parametric findings of the SC. In parametric analysis, parameters are varied to determine the sensitivity of the system's performance against each other. They stated that the most influential parameters fall under the category of geometrical (e.g. wall height, gap width), construction (e.g. type of glass, insulation) and climatic (e.g. solar radiation, wind) parameters. The effect of wall height and cavity width has in some cases been studied and expressed separately, while in others inextricably, in terms of the height-to-width aspect ratio (also referred to as height-to-gap ratio). Air flow increases with height, since the back wall's heat gains increase: in a parametric study on Trombe walls, it is reported that an increase in wall height by a quarter is equivalent to an increase in heat gains by three quarters. In another study air flow rates increased in when the wall height increased from 3.5 to 9.5m (a cavity width of 0.3m was considered). With respect to the cavity width, it was found that the induced flow rate increases with increasing width.

The intensity of solar heat flux is the motive force for the operation of the SC and is thus the most determinant factor for its performance. In the experimental study of Chen et al. (2003) varying values were considered for the uniform heat flux on the back wall and the airflow rate was found to rise by 38% for a threefold increase of heat flux (from 200W/m2 to 600W/m2). Mathur et al. (2006) found that airflow rate increases linearly with solar radiation. Based on experimental investigations on a small-scale SC, Burek and Habeb (2007) derived that the mass flow rate is proportional to $Q_i^{0.572}$ where Q_i (W/m^2) the uniform heat flux supplied to the back wall.

According to Gontikaki et al (2010) Wind is the second most influential climatic parameter, as it can create positive or negative pressures at the outlet of the SC and thus obstruct or enhance the airflow. In the outdoor experiments by Arce, et al. (2009) at a full-scale SC, the highest airflow rates coincided with the highest recorded wind velocity.

Maerefat and Haghighi (2010a), examined the heat and mass transfer characteristics of a Solar Chimney (SC) and an Evaporative Cooling Cavity using low-energy-consumption technique to improve passive cooling and natural ventilation in a solar house. The results obtained show that the system is capable of providing good indoor air condition during daytime even with low solar intensity of 200 W/m^2. Further results also show that relative humidity is a factor and at RH lower than 50%, the system performs effectively even at 40° C. Another analysis carried out by Maerefat and Haghighi (2010b), to investigate cooling and ventilation in a solar house using solar chimney (SC) together with earth to air heat exchanger (EAHE) for passive cooling as a low-energy consuming

technique for removing heat from a building in the hot seasons. The results show that the solar chimney can be used to power the underground cooling system during the daytime, without any need of electricity.

DeBlois *et al.* (2013), investigated the performance and energy level of the roof type solar chimney, and noted it being a low cost energy reduction method for passive ventilation. The results obtained indicate that the ventilated roof provided cost-free cooling and passive ventilation in all climates and seasons. The results also observed that stack effect rather than natural convection was the driving force. Further results show that the system reduced the cooling load by about 80%, while cross ventilation alone by 50% percent.

Koronaki (2013), investigated ventilation performance to assess the effectiveness of three high thermal inertia solar thermosyphonic configurations, used as night natural ventilation systems. The results obtained show that a thermal chimney with duct attached behind the absorber facing West was the most effective design with predicted flow rate 98% higher than the a similar size conventional SC.

Solar Chimney Power Plant

Man learned to make active use of solar energy at a very early stage: greenhouses helped to grow food, chimney suction ventilated and cooled buildings and windmills ground corn and pumped water. Schlaich and Wolfgang (2000) stated the solar chimney's three essential elements - glass roof collector, chimney, and wind turbines - have thus been familiar from time immemorial. A solar-thermal chimney power plant simply combines them in a new. The technology combines three components: a collector, a chimney and turbines. In the collector, solar radiation is used to heat an absorber (ordinarily soil or water bags) on the ground, and then a large body of air, heated by the absorber, rises up the chimney, due to the density difference of air between the chimney base and the surroundings. The rising air drives large turbines installed at the chimney base to generate electricity. The concept of solar chimney power technology was first conceived many years ago first described in a publication written by a German author, Gunther in 1931 (Zhou, *et al,* 2010), again presented in 1978 and proven with the operation of a pilot 50 kW power plant in Manzanares, Spain in the early 1980s (Pretorius & Kröger, 2006; Liu, *et al.*, 2005; Schlaich and Wolfgang, 2000; Zhou, *et al.*, 2010).

Pretorius and Kröger (2006) examined the effect of a convective heat transfer equation, more accurate turbine inlet loss coefficient, quality collector roof glass and various types of soil on the performance of a large scale solar chimney power plant. The Results show that the new heat transfer equation reduces plant power output considerably. Further results show that the effect of a more accurate turbine inlet loss coefficient is trivial, and using better quality glass enhances plant power production. It was also discovered that using Limestone and Sandstone soil produced similar results to Granite.
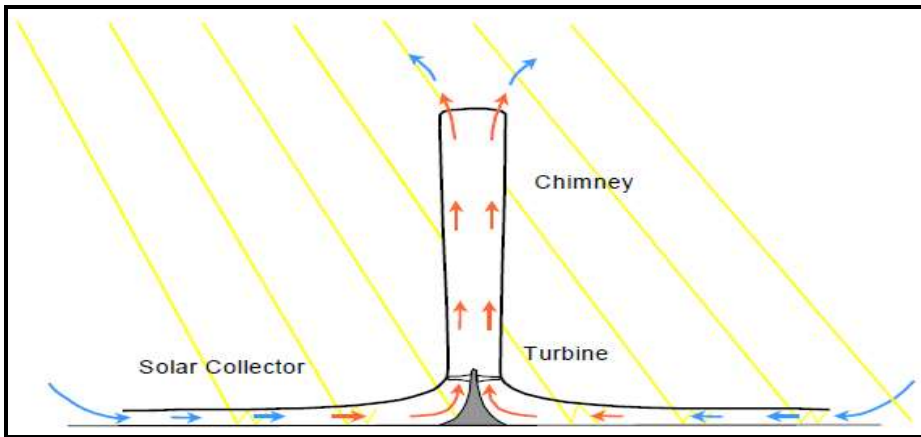
Figure 2: Principle of the solar chimney: glass roof collector, chimney tube, wind turbines

Fluri and von Backstrom (2008a) carried out performance evaluation using analytical models and optimisation techniques on several turbo-generator layouts of SCPP. Results show that slight changes in modelling approach have significant impact on the performance estimate. Further results conclude that the single rotor layout without guide vanes performs very poorly. The counter rotating layouts provide the highest peak efficiencies, however at relatively low speeds, which leads to undesirable higher torque for the same power output. Further study by Fluri and Von Backstrom (2008b) investigated the performance of the Power Conversion Unit of a SCPP and its effect on the plant. The results obtained show that single vertical axis turbine has a little better efficiency and energy yield due to some loss mechanisms are not present, however, the output torque value makes its feasibility less desirable. Further results show that redesigning the flow passage reduces aerodynamic losses and improve performance. Results show that the PCU efficiency depreciates significantly with increasing diffuser

area ratio but improves only slightly with reducing the diffuser area ratio below unity.

Zhou et al (2009) in their report found that the results based on the Manzanares prototype show that as standard lapse rate of atmospheric temperature is used, the maximum power output of 102.2 kW is obtained for the optimal chimney height of 615 m, which is lower than the maximum chimney height with a power output of 92.3 kW. Sensitivity analyses are also performed to examine the influence of various lapse rates of atmospheric temperatures and collector radii on maximum height of chimney. The results show that maximum height gradually increases with the lapse rate increasing and go to infinity at a value of around 0.0098 $K\ m^{-1}$, and that the maximum height for convection and optimal height for maximum power output increase with larger collector radius.

Pretorius and Krögerb (2009) in their report presented results indicating that windy conditions impair plant performance considerably, while nocturnal temperature inversions cause significant reductions in night-time output. Petela (2009), carried out

a thermodynamic analysis of energy and exergy balances on a simplified model of solar chimney power plant (SCPP). The results obtained show that an energy input of 36.81 MW of solar radiation to SCPP, corresponds to 32.41 MW input of radiation exergy.

Proposed combined ventilation and power solar chimney
Zhou et al (2009) describes solar chimney power technology, designed to produce electric power on a large-scale, as utilizing solar energy to produce ventilation that drives wind turbines to produce electric power. The generation of power in the process of passive ventilation is the main objective of the study; the development of a combined ventilation and power solar chimney.

II. Mathematical Model
Zhou et al (2007b) in their study developed a mathematical model based on energy balance to predict the performance of the solar chimney thermal power generating equipment for different conditions. The following assumptions are made:
1. Air follows the ideal gas law.
2. The mathematical model is considered to be in steady state.
3. There is no friction or leakage considered in the system.
4. Only the buoyancy force is considered, and wind-induced natural ventilation in the ambient is not included.
5. The temperature of the natural ground under the heat insulator bed is equal to that of the ambient.

Figure 2 shows the physical model for the solar chimney thermal power generating system. The absorber and the glazing can be heated to temperatures of T_a and T_p, respectively, due to solar energy and the greenhouse effect produced in the solar collector. Air at the ambient temperature T_∞ enters into the collector and is heated to the mean temperature T_f in the solar collector. The energy balance equations for the different components of the system are given as follows:

Collector and Chimney Glazing:

$$S_1 + h_{rap}(T_a - T_p) + h_p(T_p - T_f) = U_t(T_p - T_\infty)$$
(1)

where, S_1 denotes solar radiation absorbed by glazing cover;
h_{rap} is the radiation heat transfer coefficient between absorber and glazing cover; h_p is the convective heat transfer coefficient between glazing cover and airflow in the solar collector;
U_t denotes the overall heat loss coefficient from glazing cover to ambient, including convection by wind, radiation heat transfer from glazing cover to sky and conduction through glazing.

Absorber:

$$S_2 = h_a(T_a - T_f) + h_{rap}(T_a - T_p) + U_b(T_a - T_\infty)$$
(2)

where, S_2 denotes solar radiation absorbed by absorber;
h_a is the convective heat transfer coefficient between absorber bed and airflow in the solar collector;
U_b denotes the overall heat transfer coefficient from the absorber to the earth.

Collector airflow:

$$h_a(T_a - T_p)A_{coll} = h_p(T_p - T_f)A_{coll} + Q$$
(3)

where, A_{coll} is the collector area;

Q denotes the useful heat energy transferred to the moving airflow by convection.

The mean temperature of hot air, T_f, can be given by,

$$T_f = \varepsilon T_\infty + (1 - \varepsilon)T_0 \tag{4}$$

where, T_o is the collector outlet airflow temperature;

ε denotes the constant in mean temperature approximation, which is recommended as 0.25 by Hirunlabh et al. (1999),

$$\dot{Q} = c_p \dot{m}(T_0 - T_\infty) =$$
$$c_p \dot{m}(T_f - T_\infty)/(1 - \varepsilon) \tag{5}$$

where, c_p is the specific heat of air; m denotes the mass flow rate of hot airflow in the solar collector, which is equal to the mass flow rate of hot airflow passing through the solar collector outlet and can be calculated by the following equation,

$$\dot{m} = \rho A_{ch} V \tag{6}$$

where ρ is the air density at the solar collector outlet;

A_{ch} is the cross-sectional area of solar chimney;

V denotes hot air velocity at the solar collector outlet.

According to Schlaich J. (1995), V can be expressed as

$$V = \sqrt{2gH_{ch}(T_0 - T_\infty)/T\infty} \tag{7}$$

where g is the acceleration due to gravity and

      H_{ch} is the height of the chimney.

System's Power:

Power output P_{out} can be found as (Schlaich, 1995),

$$P_{out} = \frac{1}{3}\eta_w \rho A_{ch} V^3 \tag{8}$$

where $\acute{\eta}_w$ is the turbine generator efficiency, usually between 50% and 90%.

Ortega (2011) stated in the analyses of solar chimney design, that the

Boussinesq Model treats density as constant value in all the equations except in the buoyancy term of the momentum equation, given as follows

$$\square = \square 0\, 1 - \square\Delta\square \rightarrow \square\Delta\square \ll 1 \tag{9}$$
$$\Delta\square_{\square\square\square\square\square\square\square\square} = \square\square\square\square\Delta\square \tag{10}$$

Chimney

Assuming a uniform velocity and temperature inside the chimney the theoretical flow rate will be (Ortega, 2011):

- Energy balance in the chimney

$$Q = q\rho c_p T_{out} - T_{ext} \tag{11}$$
$$T_{out} = T_{ext} + \frac{Q}{q\rho c_p} \tag{12}$$

- Approximation velocity profile constant

$$V \cdot A = q \tag{13}$$

- Drag coefficient Vs constant pressure loss

$$C_d = \frac{1}{\sqrt{\sum K_{loss}}} \tag{14}$$

- Bernoulli equation

$$\rho g H \frac{(T_{out} - T_{ext})}{T_{ext}} = \frac{1}{2}\rho V^2 \sum K_{loss}$$

$$\rho g H(T_{out} - T_{ext}) = \frac{1}{2}\rho T_{out}\left(\frac{q}{Ac_d}\right)^2$$

$$q^3 + q^2 \frac{Q}{T_{ext}\rho c_p} - \frac{(AC_d)^2 2gHQ}{T_{ext}\rho c_p} = 0 \tag{15}$$

The value of C_d is calculated as a function of the sum of coefficient of pressure loss of the inlet, the nozzle, the outlet and the friction of the walls

$$\sum K = K_{inlet} + K_{nozz} + K_{outlet} +$$
$$f\frac{H}{Dh} \tag{16}$$

In theory, C_d is a function of the flow rate, because the factor f depends of the Reynolds's number Re, but $\square \in$ 0.04, 0.015 which gives a $\square_\square \in$ 0.75, 0.788, which is small difference (Ortega, 2011). Therefore C_d can be

considered only as the function of the height:

$$\sum K = 0.04 + 0.48 + 1 + 0.04 \frac{H}{0.5} \quad (17)$$

$$C_d = \frac{1}{\sqrt{1.52 + 0.08H}} \quad (18)$$

Natural ventilation takes place when buoyancy pressure overcomes the sum of all flow pressure losses. A mathematical model based on Bernoulli's equation is used to evaluate the system flow rate (Maerefat & Haghighi, 2010a). The chimney net draft is given by the following formula

$$Draft_{ch} = (\rho_a - \rho_{chout})gH - \left(\sum c_j + \zeta_{ch}\frac{L_{ch}}{(d_{hyd})_{ch}}\right) \times \left(\frac{\rho_{chout}V_{ch}^2}{2}\right)$$
$$(19)$$

where, c_j is the pressure loss coefficients,

ζ_{ch} is the chimney friction factor,

V_{ch} is the chimney air velocity,

ρ_{chout} is the air density at chimney outlet,

ρ_a is the ambient air density.

The kinetic energy efficiency is one of the solar chimney properties that allow the comparison of the solar chimney with other technologies. This efficiency can be calculated as the coefficient between the kinetic energy and the power generated in the solar collector:

$$\eta = \frac{\frac{1}{2}\dot{m}V^2}{Q} = \frac{\frac{1}{2}q\rho\left(\frac{q}{A}\right)^2}{Q}$$

$$\eta = \frac{q^3\rho}{2QA^2} \quad (20)$$

Computational Fluid Dynamics (CFD) Analysis

The CFD analysis of this study is performed using ANSYS FLUENT software (ANSYS, 2011). The mathematical model for the CFD analysis are the Navier-Stokes equations, the Continuity and momentum equations and the energy equation for the heat transfer analysis of the system. Additional transport equations are modelled for turbulent flow. In Reynolds averaging, the solution variables in the instantaneous (exact) Navier-Stokes equations are decomposed into the mean (ensemble-averaged or time-averaged) and fluctuating components. For the velocity components:

$$u_i = \hat{u}_i + u'_i \quad (21)$$

where $\hat{u}_i$ and u'_i are the mean and fluctuating velocity components (j = 1,2,3). Likewise, for pressure and other scalar quantities:

$$\phi = \hat{\phi}_i + \phi' \quad (22)$$

where ϕ denotes a scalar quantity. Substituting expressions of this form for the flow variables into the instantaneous continuity and momentum equations and taking a time average yields the ensemble-averaged momentum equations, written in Cartesian tensor form as:

$$\frac{\partial \rho}{\partial t} + \frac{\partial}{\partial x_i}(\rho u_i) = 0 \quad (23)$$

$$\frac{\partial}{\partial t}(\rho u_i) + \frac{\partial}{\partial x_j}(\rho u_i u_j) = -\frac{\partial}{\partial x_i} + \frac{\partial}{\partial x_j}\left[\mu\left(\frac{\partial u_i}{\partial x_j} + \frac{\partial u_j}{\partial x_i} - \frac{2}{3}\delta_{ij}\frac{\partial u_l}{\partial x_l}\right)\right]$$
$$(24)$$

Equation (23) and Equation (24) are the Reynolds-averaged Navier-Stokes (RANS) equations and have the same general form as the instantaneous Navier-Stokes equations, with the velocities and other solution variables now representing ensemble-averaged (or time-averaged) values. Additional terms now appear that represent the effects of turbulence. Reynolds

stresses $(-\rho u_i' u_j')$ are modelled in order to close Equation 24. The Boussinesq hypothesis is related to the Reynolds stresses to the mean velocity gradients:

$$-\rho \overline{u_i' u_j'} = \mu_t \left(\frac{\partial u_i}{\partial x_j} + \frac{\partial u_j}{\partial x_i}\right) - \frac{2}{3}\left(\rho k + \mu_t \frac{\partial u_k}{\partial x_k}\right)\delta_{ij}$$

(25) The Boussinesq hypothesis is used in the $k - \varepsilon$ models employed in the study. The standard $k - \varepsilon$ model is based on model transport equations for the turbulence kinetic energy (k) and its dissipation rate (ε).

$$\frac{\partial}{\partial t}(\rho k) + \frac{\partial}{\partial x_i}(\rho k u_i) = \frac{\partial}{\partial x_j}\left(\left(\mu + \frac{\mu_t}{\sigma_k}\right)\frac{\partial k}{\partial x_j}\right) + G_k + G_b - \rho\varepsilon + S_k$$

(26)

$$\frac{\partial}{\partial t}(\rho\varepsilon) + \frac{\partial}{\partial x_i}(\rho\varepsilon u_i) = \frac{\partial}{\partial x_j}\left(\left(\mu + \frac{\mu_t}{\sigma_\varepsilon}\right)\frac{\partial\varepsilon}{\partial x_j}\right) + C_{1\varepsilon}(G_k + C_{3\varepsilon}G_b) - C_{2\varepsilon}\rho\frac{\varepsilon^2}{k} + S_\varepsilon$$

(27)

In the equations above, G_k represents the generation of turbulence kinetic energy due to the mean velocity gradients, and G_b is the generation of turbulence kinetic energy due to buoyancy. ANSYS FLUENT solves the energy equation in the following form:

$$\frac{\partial}{\partial t}(\rho E) + \nabla \cdot \left(\vec{V}(\rho E + \rho)\right) = \nabla \cdot \left(k_{eff}\nabla T - \sum_J h_j \bar{J}_j + (\bar{\tau}_{eff}\cdot\vec{V})\right) + S_h$$

(28)

Where k_{eff} is the effective conductivity ($k + k_t$, where k_t is the turbulent thermal conductivity, defined according to the turbulence model being used), and $\bar{J}_j$ is the diffusion flux of species j. The first three terms on the right-hand side of Equation (8) represent energy transfer due to conduction, species diffusion, and viscous dissipation, respectively.
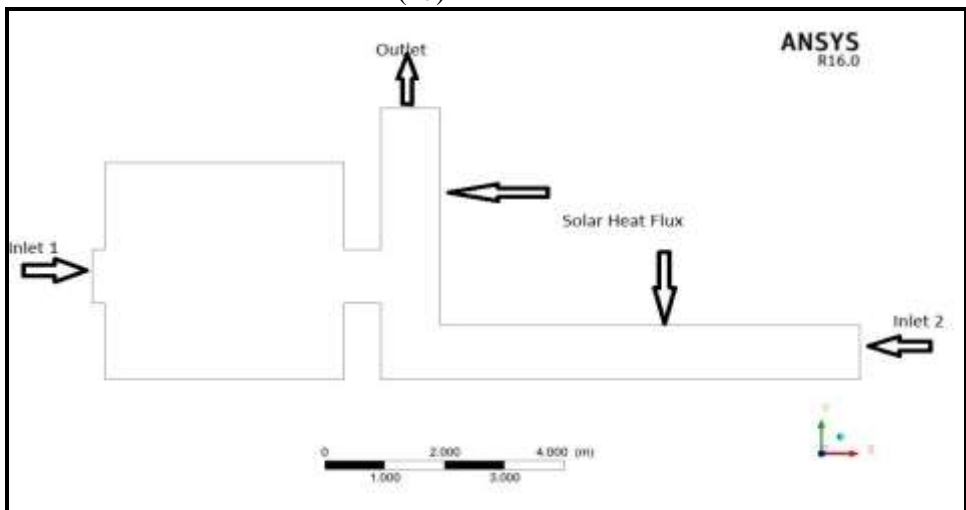
Computational Domain

Figure 3: 2D Computational Domain

III. Results and Discussion

The analytical model was simulated using an Excel Spread Sheet, while the numerical simulation was carried out using ANSYS Fluent package. The power outputs simulated by the program are obtained for different conditions, as shown in Figures 15 and 16. The results show that power outputs of the power generating systems increases with increase in the Heat Energy in the collector space area which is a function of the global solar radiation intensity and collector area, and chimney height.
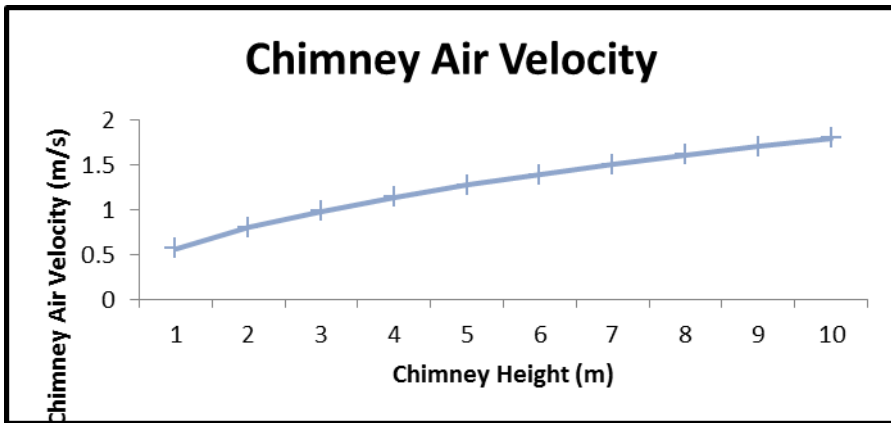
Analytical Results:

Figure 4: Effect of Chimney Height on Chimney Air Velocity (Analytical)
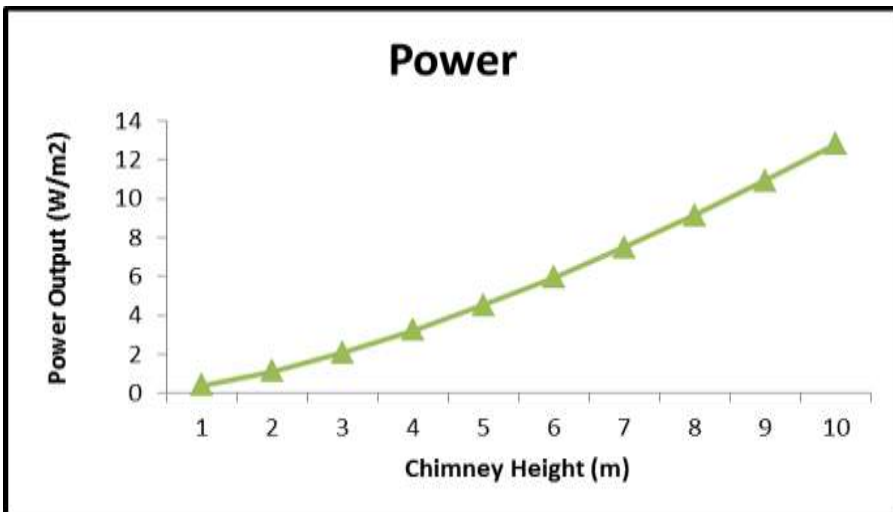
Figure 5: Effect of Chimney Height on Power Generated
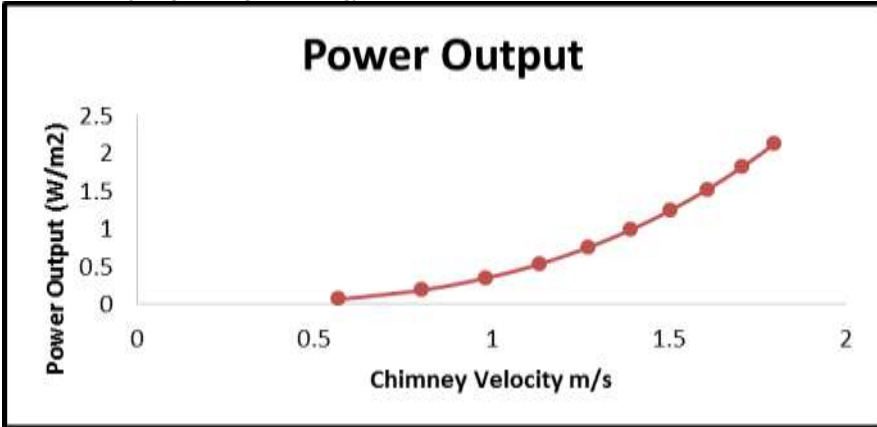
Figure 6: Effect of Chimney Air Velocity Power Output Ra = 10^{10}
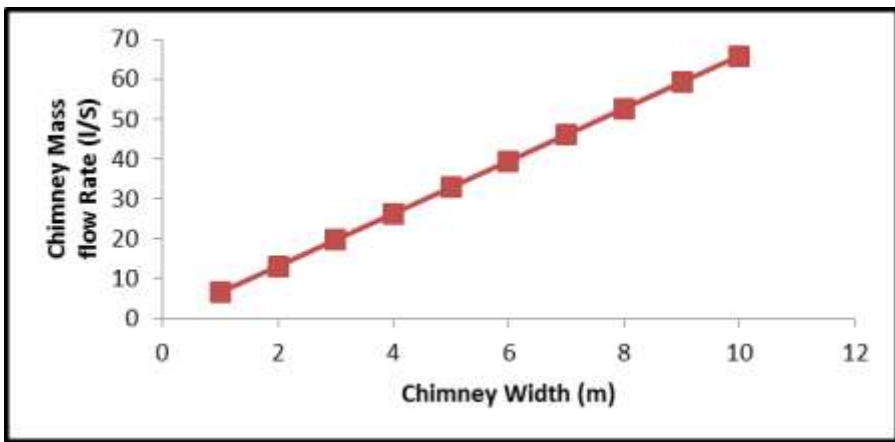
Figure 7: Effect of Chimney Width on Air Mass Flow Rate
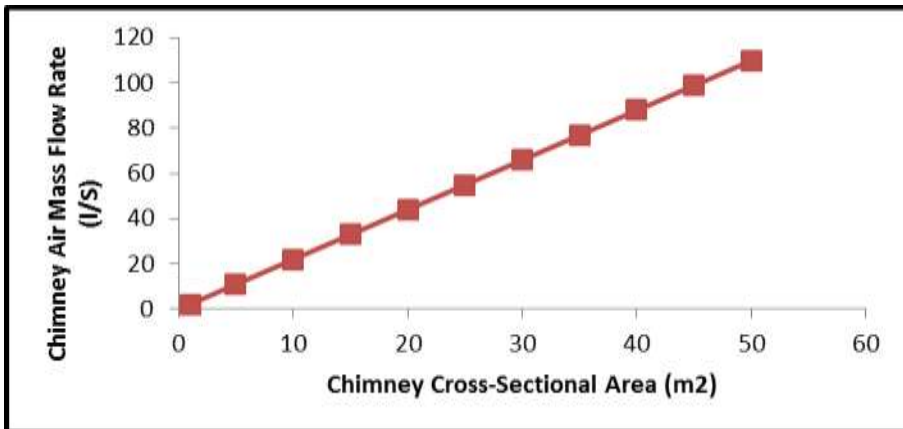
Figure 8: Effect of Chimney X-Sectional Area on Air Mass Flow Rate
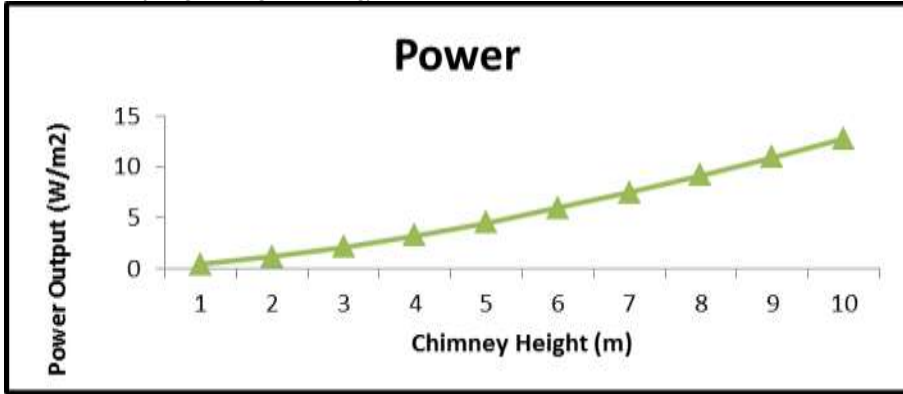
Figure 9: Effect of Chimney Height on Power Generated
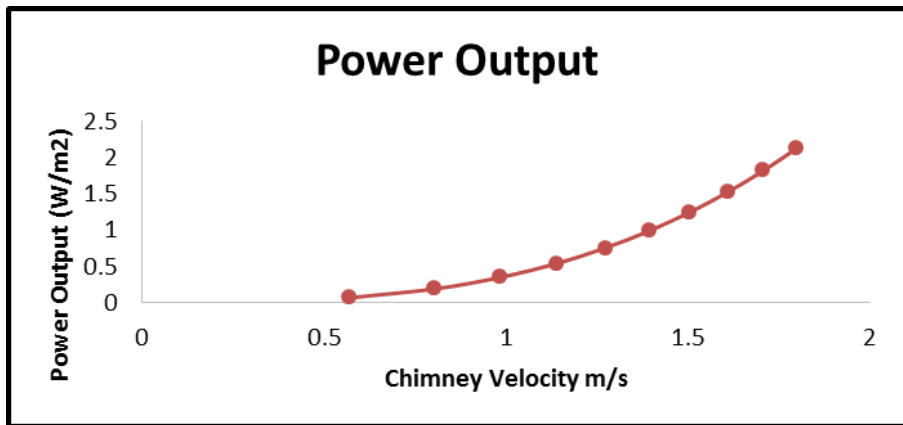
Figure 10: Effect of Chimney Air Velocity Power Output Ra = 10^{10}
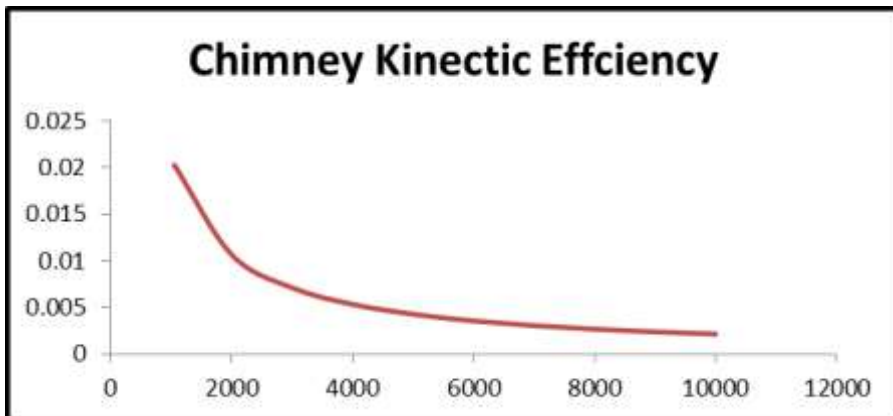
Figure 11: Comparison of Heat Energy (Power Generated) in the Collector with Chimney Kinetic Efficiency
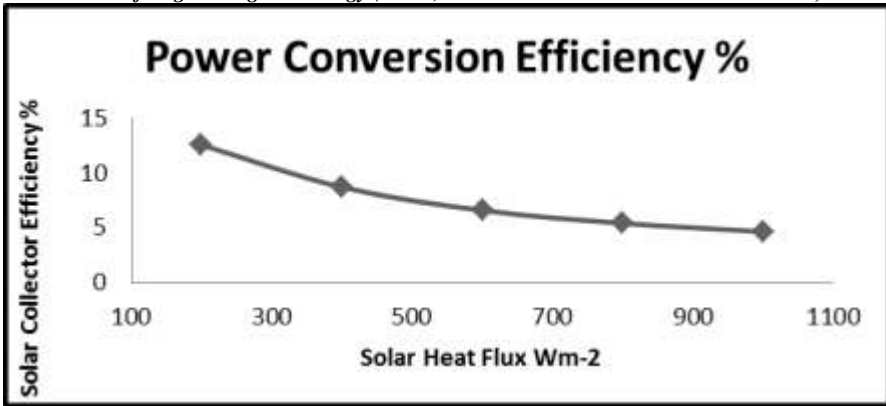
Figure 12: Solar Collector Efficiency with Increase in Solar Heat Flux
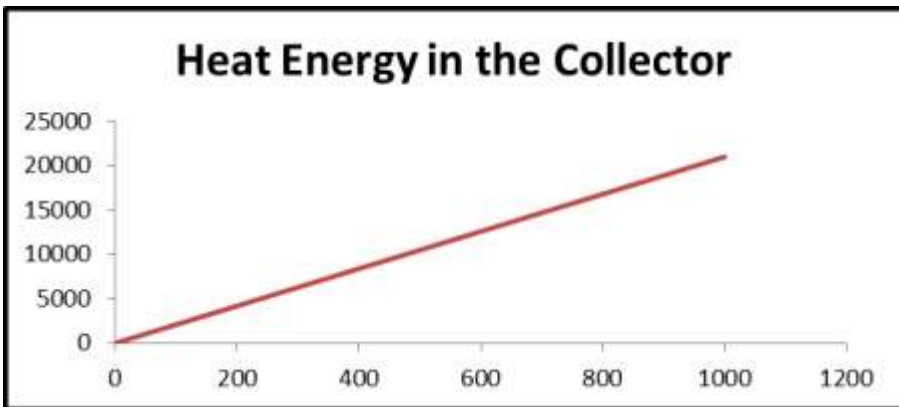
Figure 13: Effect of Collector Area on Heat Energy in the Collector Space
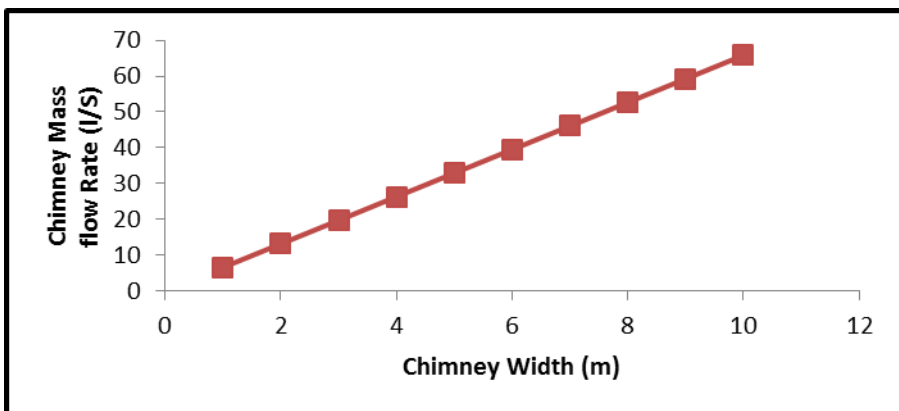
Figure 14: Effect of Chimney Width on Air Mass Flow Rate

Numerical Results:
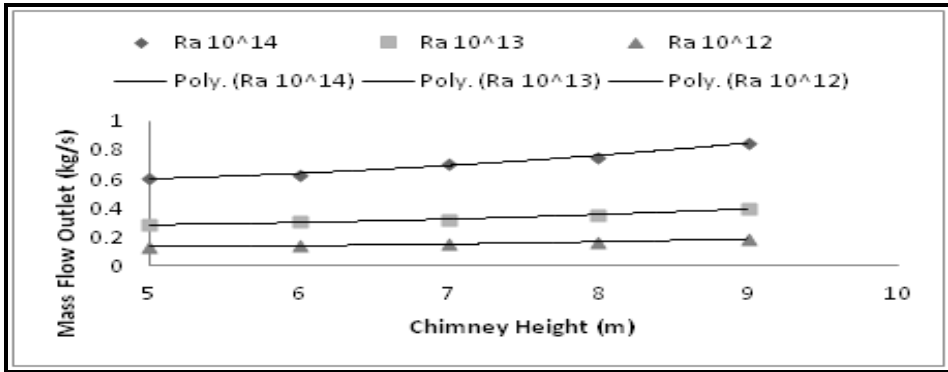
Figure 15: Effect of Chimney Height on Mass Flow at Outlet at no Induced Wind, CH of 5 m and SHF of 400 W/m^2 Condition for Ra = 10^{12} – 10^{14}
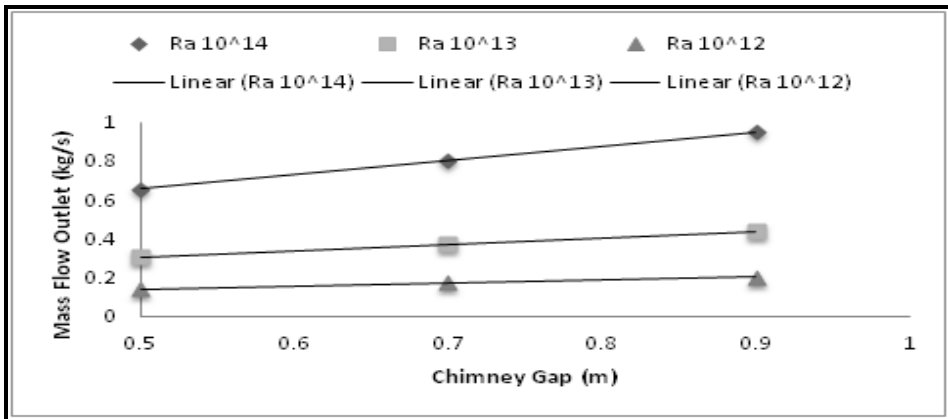
Figure 16: Effect of Chimney Gap on Mass Flow at Outlet at no Induced Wind, CH of 5 m and SHF of 400 W/m^2 Condition for Ra = 10^{12} – 10^{14}
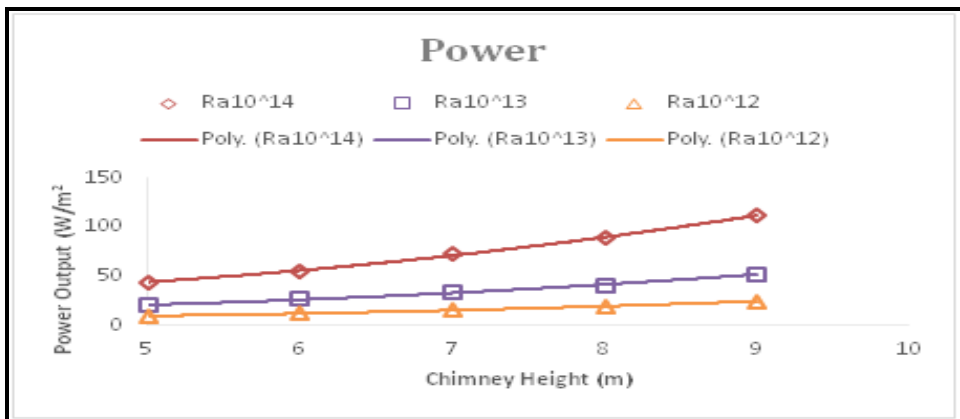
Figure 17: Effect of Chimney Height on Power Output for Ra = 10^{12} - 10^{14}
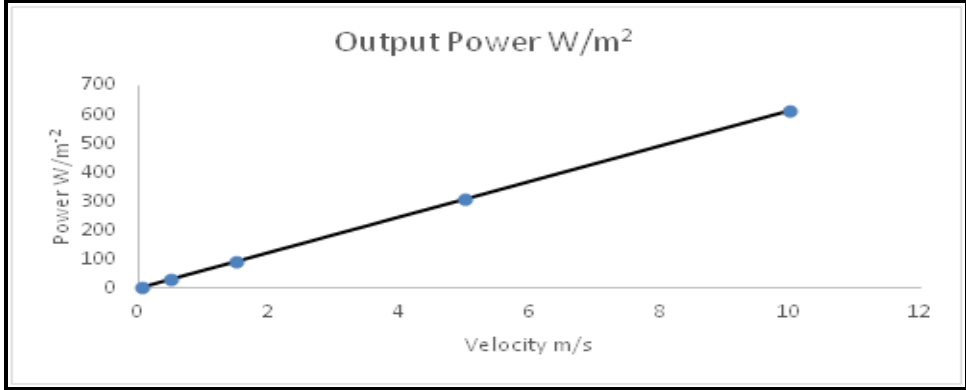
Figure 18: Effect of Flow Velocity on Power Output Ra = 10^{14}
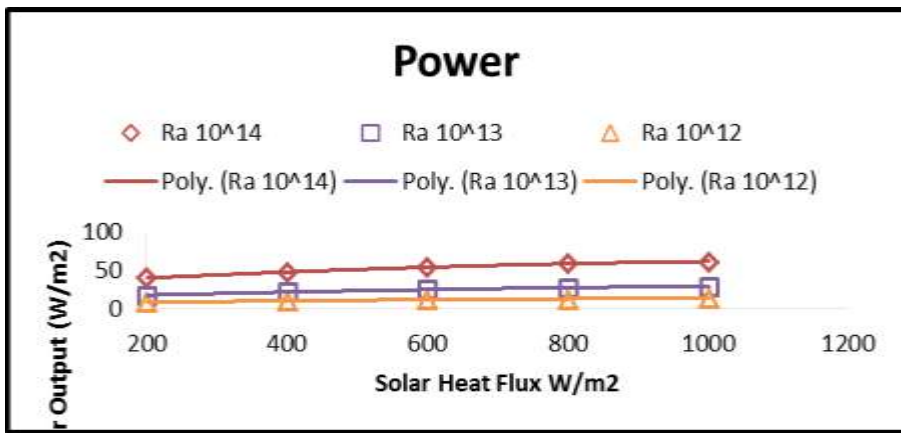
Figure 19: Effect of Solar Heat Flux on Power Output for Ra = 10^{12} - 10^{14}

Effect of Solar Heat Flux, Chimney Height and Chimney width on Outlet Mass Flow Rate and Chimney Velocity

The outlet mass flow rate, which is also a function of the chimney velocity was observed to increase from 0.5 to 0.8 kg/s at Ra = 10^{14} for SHF of 200 to 1 000 W/m^2 with a chimney height of 5 m and width of 1 m. The velocity increased from about 0.6 to about 2 m/s for chimney height of 1 m to 10 m. This confirms observations from literature that the chimney height is a major factor in determining the power output of the

SC (Schlaich and Schiel, 2000; Liu *et al*, 2005; Pretorius and Kröger, 2006; Zhou *et al*, 2009).

Effect of Solar Heat Flux and Chimney Height on Power Output

The power output per unit area was found to increase from 39 to 61 W/m^2 for solar radiation of 200 and 1,000 W/m^2 at Ra = 10^{14}, with a solar radiation to flow power conversion of 19.5 % and 6.1 % respectively. The effect of the chimney height on the power output of the SC was 154.6 % increase from power output of 44 to 112 W/m^2 at chimney height of 5 to 9 m at solar radiation of 400 W/m^2 and

Ra = 10^{14}. The conversion effect (ratio of power to chimney height) are 8.8 and 12.4 for heights of 5 and 9 m respectively.

Effect of Flow Velocity on Power Output

The flow velocity is another major factors of the power output of the SC. Results show that an increase in channel velocity from 0.05 to 1.5 m/s caused the power output to increase from 3.1 to 92.1 W/m^2, while an increase to 5 and 10 m/s resulted in a power output of 307.1 and 614.1 W/m^2 respectively. It was noted that the channel velocity was affected by factors, which include the ambient wind velocity, the temperature difference between the ambient temperature and the channel temperature (which was a function of the solar heat flux) and the geometry of the SC. However, the factor within human control was the geometry of the system. At constant ambient conditions, it is suggested that a convergent divergent channel may help in increasing the velocity at required points for an increase in power output instead of the rectangular channel used.

Optimised Model Analysis

The optimisation criteria have been set with model constraints that will produce optimum effect for both room ventilation and power generation. Two (2) optimal solutions were found that placed the chimney height and the solar collector breadth at values of 5 m and 1 m respectively. This solution minimised the chimney height and the solar collector breadth, which will reduce the size of the system and consequently reduce the cost of the system.

The minimisation of the solar heat flux was between 200 and 600 W/m^2, as a result of the average solar insolation experienced in the Southern Nigeria Region. The optimised solutions found for the solar heat flux for the two optimum (2) solutions are 407 and 417 W/m^2 which is close to the average range of Solar Heat Flux values for Nigeria (Osueke *et al.*, 2013).
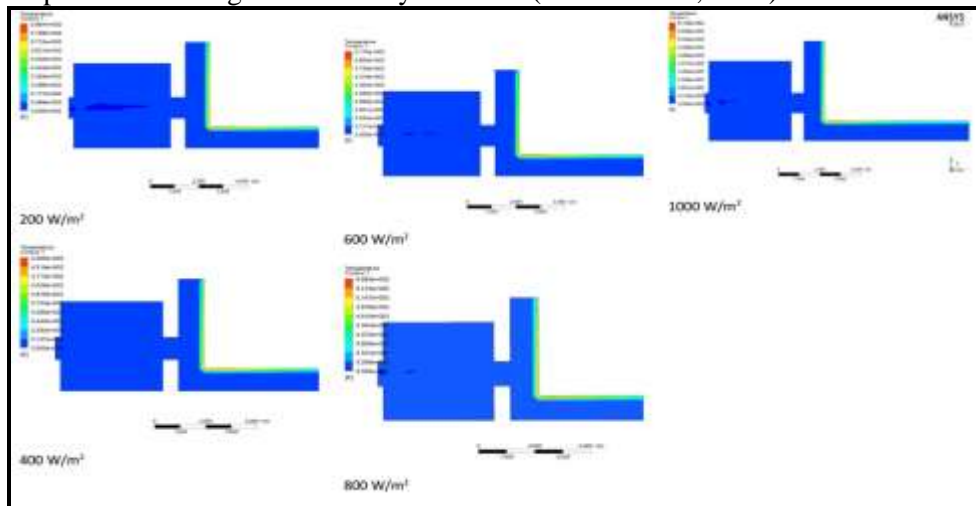
Figure 20: The temperature contour of the SC system at heat flux of 200 – 1,000 W/m^2

The results from the optimised model showed that the room temperature was conserved and maintained at the value of 300 K (Figure 20). This increase in velocity at the cavity as the room air enters the chimney is due to the boundary layer effect at the cavity and the suction pressure differential; coupled with the stack effect within the chimney, the velocity increase was observed within the chimney from 0.05 m/s to 0.12 m/s.. The chimney temperature was found to have increased from 300 K to 314.7 K and 315.1 K for both solutions.

The velocity at the junction between the chimney and the horizontal solar collector also showed an increase in velocity from 0.05 m/s to 0.07 m/s for both optimised solutions. However, it was observed that for power generation it will be more desirable to put the turbine at a position close to the top of the Chimney, since it is this part that correspond to maximum velocity.

Moreover, Gontikaki *et al.* (2010) noted that wind is a highly influential climatic parameter and its effect is a major contributor to the effectiveness of a SC system: In that respect, thus would improve the results from the optimised model.

Effect of Solar Radiation on Ventilation flow pattern and Temperature within the Room

The outlet mass flow rate, which is also a function of the chimney velocity was observed to increase from 0.5 to 0.8 kg/s at $Ra = 10^{14}$ for SHF of 200 to 1 000 W/m^2 with a chimney height of 5 m and width of 1 m. The flow within the room showed that with cross ventilation the flow across increases in velocity as the solar radiation increases, creating two pressure zones above and one below the cross flow section (Figure 21). This is due to the pressure differential created by the cross flow and the temperature vis-à-vis density of air at the two zones.
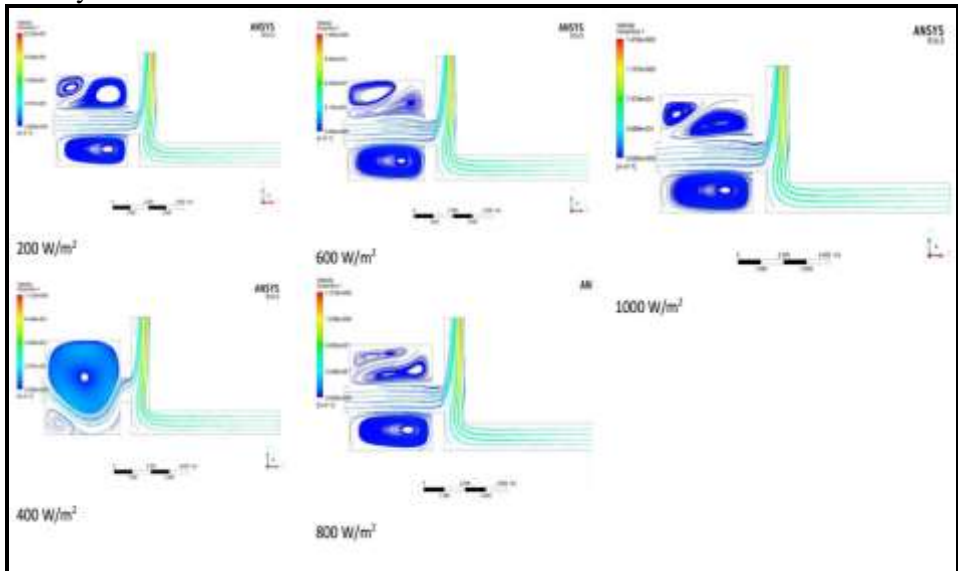
Figure 21: The flow pattern of the SC system at heat flux of 200 – 1,000 W/m^2

IV. Conclusion

In conclusion, the Solar Chimney was analysed for potentials for providing being used as a means of ventilation and electric power generation in buildings in Nigeria. The study aimed at the development of a solar chimney model for the dual purpose of passive ventilation and renewable power generation in buildings. In this study analysis were carried out using basic equations of thermos-fluids to carry out sensitivity analysis of the model. The mass flow rate increased as chimney height increases. It was also observed that the mass flow is a direct function of the solar radiation input. The power output of the system was found to increase with both increase in solar radiation and chimney height. It is therefore concluded from the performance analysis that the combined solar chimney is a feasible a means of improving energy efficiency of buildings. Furthermore, it is noted that combined solar chimney had better results at locations with higher solar radiation and wind conditions for both ventilation and power.

Reference

[1]   Alex Morales (February 7, 2012). "Wind Power Market Rose to 41 Gigawatts in 2011, Led by China" (http://www.businessweek.com/news/2012-02-07/wind-powermarket-rose-to-41-gigawatts-in-2011-led-by-china.html). Bloomberg.

[2] ANSYS FLUENT Theory Guide (2011) ANSYS, Inc., Southpointe, 275 Technology Drive, Canonsburg, PA 15317, ansysinfo@ansys.com, http://www.ansys.com, Release 14.0 November 2011.

[3]   Arce, J., Jimenez, M. J., Guzman, J. D., Heras, M. R., Alvarez, G., Xaman, J. (2009). Experimental study for natural ventilation on a solar chimney. *Renewable Energy*, 34: 2928-2934.

[4]   Bar-Cohen, A. & Krauss, A.D. (1988). Advances in Thermal Modeling of Electronic Components and Systems. Hemisphere Publishing Corporation, New York.

[5] Ben Sills (Aug 29, 2011). "Solar May Produce Most of World's Power by 2060, IEA Says". *Bloomber http://www.bloomberg.com/news/2011-08-29/solar-may-produce-most-of-world-s-power-by-2060-iea-says.html* (viewed 1st Nov. 2012)

[6]   Bilgen, E. & Michel, J., (1979). Integration of solar systems in architectural and urban design. In: Sayigh, A.A.M. (Ed.), *Solar Energy Appl Build*. Academic Press, New York.

[7]   Burek, S.A.M., Habeb, A. (2007). Air flow and thermal efficiency characteristics in solar chimneys and Trombe Walls. *Elsevier, Energy and Buildings* 39: 128–135.

[8] Chen, Z.D., Bandopadhayay, P., Halldorsson, J., Byrjalsen, C., Heiselberg, P., Li, Y. (2003). An experimental investigation of a solar chimney model with

uniform wall heat flux. *Building and Environment,* 38: 893-906.

[9]   Ekechukwa, O.V. & Norton, B. (1999). Review of solar energy drying system II. An overview of solar drying technology. *Energy Conserv. Manage.* 40: 615–655.

[10] DeBlois J., Bilec M., Schaefer L. (2013). Simulating home cooling load reductions for a novel opaque roof solar chimney configuration. *Applied Energy,* 112: 142–151.

[11] Fluri T. P., von Backstrom T. W. (2008a). Comparison of modelling approaches and layouts for solar chimney turbines. *Solar Energy,* 82: 239–246.

[12] Fluri T. P., Von Backstrom T. W. (2008b). Performance analysis of the power conversion unit of a solar chimney power plant. *Solar Energy,* 82: 999–1008.

[13] Gontikaki, M., Trcka, M., Hensen, J.L.M. & Hoes, P. (2010). Optimization of a Solar Chimney Design to Enhance Natural Ventilation in a Multi-Storey Office Building. Proceedings of 10th International Conference for Enhanced Building Operations, Kuwait: ICEBO.

[14] Hirunlabh J, Kongduang W, Namprakai P, Khedari J. (1999). Study of natural ventilation of houses by a metallic solar wall under tropical climate. *Renewable Energy,* Volume 18:109–19.

[15] Koronaki I. P. (2013). The impact of configuration and orientation of solar thermosyphonic systems on night ventilation and fan energy savings. *Energy and Buildings,* 57: 119–131.

[16] Liu W., Ming T. and Yang K. (2005). Simulation of Characteristics of Heat Transfer and Flow for MW Grade Solar Chimney Power Plant. Proceedings of ISEC 2005, 2005 International Solar Energy Conference, August 6-12, 2005, Orlando, Florida. ISEC2005-76221.

[17] Maerefat M., Haghighi A. P. (2010a). Natural cooling of stand-alone houses using solar chimney and evaporative cooling cavity. *Renewable Energy,* 35: 2040–2052.

[18] Maerefat M., Haghighi A. P. (2010b).Passive cooling of buildings by using integrated earth to air heat exchanger and solar chimney. *Renewable Energy,* 35: 2316–2324.

[19] Mathur, J., Bansal, N. K., Mathur, N. K., Jain, M., Anupma. (2006). Experimental investigations on solar chimney for room ventilation. *Solar Energy,* 80: 927-935.

[20] Nouanégué, H.F. & Bilgen, E. (2009). Heat transfer by convection, conduction and radiation in solar chimney systems for ventilation of dwellings, *Elsevier,*

International Journal of *Heat and Fluid Flow*, 30: 150–157.

[21] Ortega E. P. (2011). Analyzes of Solar Chimney Design. Master's Thesis submitted to the Norwegian University of Science and Technology, Department of Energy and Process Engineering July 2011. 82 Pages.

[22] Petela R. (2009). Thermodynamic study of a simplified model of the solar chimney power plant. *Solar Energy,* 83: 94–107.

[23] Pretorius, J. P. & Kröger, D. G. (2006). Critical evaluation of solar chimney power plant performance. *Elsevier, Solar Energy*, 80: 535–544.

[24] Pretorius, J. P. & Kröger, D. G. (2009). The Influence of Environment on Solar Chimney Power Plant Performance. *R & D Journal, of the South African Institution of Mechanical Engineering, 25.* http://www.saimeche.org.za (open access)

[25] Renewables 2011 Global Status Report (2011). http://www.ren21.net/Portals/97/do cuments/GSR/GSR2011_M aster18.pdf (viewed 1st Nov. 2012).

[26] Odia, O. O., Ososomi, S. A., & Okokpujie, P. I. (2016). Practical Analysis of A Small Wind Turbine for Domestic Use on Latitude 7.0670 N, Longitude 6.2670

E. *Journal of Research in Mechanical Engineering*, *2*(11), 8-10.

[27] Schlaich J. (1995). The solar chimney: electricity from the sun. In: Maurer C, editor. Germany: Geislingen

[28] Schlaich, J., Wolfgang S. (2000). Solar Chimneys, Encyclopedia of Physical Science and Technology, Third Edition.

[29] Sudaporn C. and Bundit L. (2006). A Numerical Study of Natural Ventilation in Buildings - Utilized Solar Chimney and Cool Ceiling. The 2nd Joint International Conference on "Sustainable Energy and Environment (SEE 2006)" November 2006, Bangkok, Thailand B-043 (P) 21-23.

[30] United Nations Environment Programme: *Global Trends in Sustainable Energy Investment 2007: Analysis of Trends and Issues in the Financing of Renewable Energy and Energy Efficiency in OECD and Developing Countries,* sefi.unep.org/fileadmin/med ia/sefi/docs/publications/SE FI_Investment_Report_2007 .pdf (viewed 1st Nov. 2012)

[31] Zhou X. P., Yang J. K. and Xiao B. (2007a). Improving natural ventilation in combined solar house with solar chimney and solar water collector. *Journal of the Energy Institute*, Volume 80(1): 55-59.

[32] Zhou, X. P., Yang, J. K., Xiao, B. & Hou, G. (2007b).

Simulation of a pilot solar chimney thermal power generating equipment. *Elsevier Renewable Energy,* 32: 1637–1644.

[33] Zhou, X. P., Yang, J. K., Xiao, B., Hou, G. & Xing, F. (2009). Analysis of chimney height for solar chimney power plant. *Elsevier Applied Thermal Engineering*, 29: 178-185.

[34] Zhou, X. P., Wanga, F., Fan J. and Ochieng, R. M. (2010). Performance of solar

chimney power plant in Qinghai-Tibet Plateau. *Elsevier Renewable and Sustainable Energy Reviews,* 14: 2249–2255.

[35] Osueke, C. O., Uzendu, P., Ogbonna, I. D. (2013), Study and Evaluation of Solar Energy Variation in Nigeria. International Journal of Emerging Technology and Advanced Engineering, 3(6): 501 – 505.

Thermophysical Properties of Gmelina Arborea Biodiesel

Mercy Ogbonnaya[1]*, Francis Onoroh[1], Abiodun O. Falope[2] & Peace I. Omoruyi[1]

[1]Department of Mechanical Engineering, University of Lagos, Akoka, Nigeria.
[2]Department of Chemical Engineering, University of Lagos, Akoka, Nigeria
*mogbonnaya@unilag.edu.ng; mercydivine2k2@yahoo.co.uk

Abstract- The depletion of petroleum reserves, rising cost of conventional fuels and the ill effect of emission from the use of fossil fuel on human health and environment have driven scientific research towards the development of alternative source of fuels such as biofuel and biodiesel. Biodiesel is a fuel from a renewable sources and it has the potential of being used as an alternative to fossil diesel in compression ignition engine. Some of the challenges encountered in the use of biodiesel in compression ignition engine are its availability, use of edible oil for its production, cost of biodiesel feedstock and unfavorable properties of biodiesel such as its high viscosity. Presently, there is a search for more inedible oil seeds since the available inedible feedstock are still not enough to replace more than 20 - 25% of the total transportation fuels. The thermophysical properties of the biodiesel which vary from feedstock have a significant impact on the combustion process thereby affecting the overall engine performance and emissions. The aim of this study is to test the compatibility of biodiesel from Gmelina arborea seed oil in the compression ignition engine through its thermophysical properties. The biodiesel was produced using transesterification method and the thermophysical properties tests were carried out. The results showed that the density and viscosity of Gmelina arborea seed oil was 868.8 kg/m^2 (at 27.5°C) and 1.882(mm)^2/s (at 40.0°C) respectively. It also showed that the biodiesel obtained had a density and viscosity value of 821.2 kg/m^3 (at 27.5°C) and 0.794 9 (mm)^2/s (at 40.0°C) respectively. Comparing these results with other biodiesel, it was observed that Gmelina arborea oil has a lower viscosity and density than other biodiesel from different feedstocks; therefore it has potential to perform better in the diesel engine in comparison to other biodiesel.

Key Words: Viscosity, Biodiesel, Density, Thermo-physical properties, Transesterification, Gmelina Arborea

I. Introduction

Energy is important in the development and growth of any nation. Over the past years, most of the energy consumed in the power and transportation sectors is gotten from fossil fuel. With the depletion of petroleum reserves, rising cost of conventional fuels and the ill effect of emission from the use of fossil fuel on human health and environment, the total dependence of energy from this source is no longer sustainable. Due to these energy crises faced by the world and the desire to reduce greenhouse gases in the transportation and other sectors, several researches are ongoing on renewable energy technologies such as biodiesel, biomass, ethanol, solar and wind in order to produce and promote the use of alternative energy that are renewable, competitive, sustainable and its emission has little or no effect on the human and the environment when compared with fossil fuel (Raj et al., 2011).

Amongst the various biofuel that are being investigated for use in compression ignition engine, biodiesel has recently been considered as one of the best alternative to diesel fuel because it is simple to produce and use, biodegradable, non-toxic, reduces air pollutants and greenhouse gases such as particulates, sulphur, carbon monoxide, hydrocarbons and can be used in a compression ignition engine with little or no modification to the core engine configuration (Dennis et al, 2009; Ma and Hanna, 1999).

Biodiesel is defines as a mixture of mono-alkyl ester of long chain (C16-C18) fatty acid derived from vegetable oil or animal fats and meets the specification of ASTM D 6751 (Knothe, 2005). Biodiesel can either be used in its pure form called (B100) or can be blended with petroleum diesel at any level to create a biodiesel blend (B5, B10, B20 etc.). Several methods such as direct blending with diesel, pyrolysis, micro emulsification and transesterification have been used to reduce the high viscosity of vegetable oil and fat in order to enable their use in existing diesel engine without operational problems such as formation of large droplets in injection which could cause poor fuel atomization during the spray, increase depositions on the engine, more energy to pump the fuel and wears in fuel pump elements and injectors (Xue et al., 2011). High viscosity of biodiesel can also cause poor combustion, increase exhaust smoke and emission (Knothe and Steidley, 2005). Biodiesel can be produced from animal fat, plants' oil, waste frying oil and recently microorganism such as microalgae, yeast, fungi and bacterium (Meng et al., 2008). Plant oils are promising feedstocks for the production of biodiesel since they are renewable in nature, readily available and can be produced on a large scale. The plant oils may be categorized into edible oil from sunflower, groundnut, soybean, palm and coconut oil while the inedible oils can be gotten from jatropha, karanja, rubber seed, neem, mahua (Kumar and Sharma 2011; Ogbonnaya 2010; Sharma et al. 2008). More than 95% of biodiesel produced comes from edible oils

since the properties of biodiesel produced from these oils are suitable alternative to diesel fuel (Gui et al., 2008). However, several debates are ongoing on the effect of using edible oil for biodiesel production on food production and its price. It is believed that the use of edible oils will give rise to food scarcity. Some economic analysts believe that the increase in staple food prices is connected with the use of edible oil for biodiesel production (FAO, 2008). Animal fat which is also a potential alternative to edible oil contains higher saturated fatty acids and normally exist as solid in atmospheric temperature and pressure; thus requiring multiple chemical steps or other methods which may increase the cost of biodiesel production. Therefore, there is a need to source for more inedible plant oil seeds which has the potential to replace the edible oil seeds and thereby increase the available inedible feedstock which are still not enough to replace more than 20-25 % of the total transportation fuels.

Researches have shown that the thermophysical properties of biodiesel strongly depend on the feedstock used in the production of biodiesel. The composition of a particular plant feedstock depends on the soil type, climatic conditions, plant health and maturity upon harvest (Abdullah et al., 2007). The properties of the various individual esters that compose biodiesel determine its overall properties (Knothe, 2005). Alamu et al. (2008) studied the properties of palm-kernel biodiesel. Result of the study was compared to that of the European biodiesel standard, rapeseed biodiesel and canola biodiesel. The result

showed that biodiesel from palm kernel had a cloud point of 6°C which was higher than biodiesel from rapeseed and canola oil with values of -2°C and -1°C respectively. Ogbonnaya (2010) studied the effect of varying biodiesel production parameters such as the amount of catalyst used on biodiesel yield and thermophysical properties of biodiesel using jatropha oil. Result of the study showed that at optimal yield of 95%, the kinematic viscosity was 4.7 mm^2/s while the density was 865 kg/m^3. The results also showed that the thermophysical properties of jatropha biodiesel were within the ASTM standard for diesel and biodiesel which makes it suitable for use in compression ignition engines.

Yuan et al. (2003) developed a method to predict the physical properties of biodiesel for combustion modelling. The prediction of the critical properties of the biodiesel is very important because they are used to estimate the biodiesel's properties such as liquid density, heat of vaporization, thermal conductivity and diffusion coefficient. These parameters have direct effect on the performance of the compression ignition engine using biodiesel (Tesfa et al, 2010). Lin (2011) investigated the effect carbon composition of different vegetable oil which in includes carbon contents, carbon chain lengths and saturated or unsaturated carbon bond on engine performance, fuel consumption, the exhaust emissions and exhaust gas temperature. The result showed that biodiesel with shorter carbon length and more saturated carbon bond can effectively reduce exhaust emission, smoke, HC, NOx, and exhaust gas

temperature. The engine performance was satisfactory.

The prime aim of this paper is to produce biodiesel from an alternative inedible feedstock known as Gmelina arborea seed oil usin 59 transesterification method and to experimentally determine the thermophysical properties of the biodiesel produced. The obtained values are to be compared with ASTM D 6751 of biodiesel and ASTM D 975 of petroleum diesel to ascertain the possibility of using biodiesel produced from Gmelina arborea directly or blended with diesel fuel in a compression ignition engine without modification to the engine core.

II. Methodology

Preparation and extraction of oil from Gmelina arborea seed

Gmelina arborea trees make up about 60% of Nigeria's planted forest. The Gmelina arborea seeds are not consumed by humans or animals. Oil can be extracted from this seed, thereby making it a viable good source of biodiesel. The Gmelina arborea seeds used was obtained from Ututu in Arochukwu Local Government, Abia state, Nigeria. The seed obtained was de-hulled and dried under the sun for about 2 - 4 days. The kernel was then separated from the shell to remove the oil seed. The ideal conditions to store the oil seed are; 26 - 27°C and 60 - 70% humidity in a well-ventilated place to prevent the seeds from decaying.

Two types of method were used to extract the oil from the seed which are the hydraulic manual pressing machine and the solvent method. The oil extracted using hydraulic manual pressing machine was about 20 - 30%

while the solvent method gave a higher oil yield of about 40 - 50%. Comparing result with the oil yield of 35%, 30.40% and 40% for coconut, jatropha, and neem, respectively (Ogbonnaya, 2010), the Gmelina oil seeds has greater oil yield thereby making it more economical in biodiesel production.

Optimization of biodiesel production process

The oil obtained was heated to about 100°C and held at that temperature to allow any trace of water present to evaporate. The presence of water will slow the rate of reaction and also cause the formation of soap during the biodiesel production. The cartilage filter was used to remove solid particles from the oil.

Titration process was performed before the production of biodiesel to determine the appropriate amount of potassium hydroxide (KOH) catalyst that would produce optimal yield of biodiesel. The materials used for titration are Iso-propyl alcohol, deionized water and phenolphthalein. 0.1 KOH solution was created by dissolving 1 gram of KOH in 1 liter of distilled water. The Isopropyl-oil mixture was obtained by measuring 10 ml of Isopropyl alcohol with a syringe and mixed it with 1 ml of warm oil (40°C) in a beaker labelled "alcohol and oil". The solution was warmed and stirred gently until the mixture turned clear. The KOH solution was poured out in a beaker and 3 ml was measured out with a syringe. Two (2) drops of phenolphthalein were added to the isopropyl-oil mixture. 0.5ml of KOH solution was then added sequentially into the isopropyl-oil mixture, stirring all the time, until the mixture stayed pink for 10 seconds.

The process of transesterification was used in the production of biodiesel because it is simple and cost effective when compared with other processes. Transesterification involves stripping the glycerin from the fatty acid with a catalyst and replacing it with an anhydrous alcohol as shown in Figure 1. The alcohol and catalyst used was methanol (CH_3OH), 99% pure and Potassium hydroxide (KOH) respectively. This process yielded alcohol esters and glycerol as the by product.
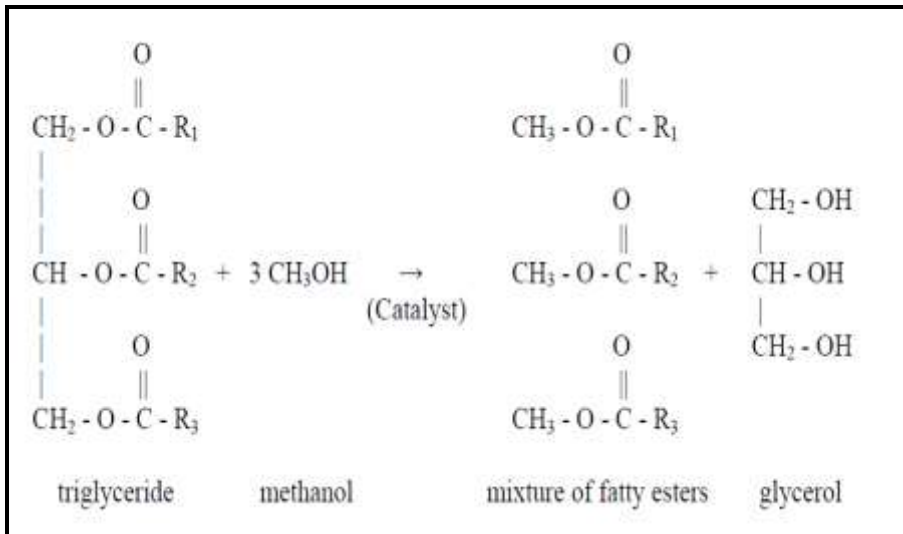
Fig. 1: Transesterification reaction process (Schuchardt *et al*., 1997)

R_1, R_2 and R_3 are long chains of carbon and hydrogen atoms, sometimes called fatty acids. The chains are usually of different length and degree of saturation within the triglyceride molecule of the lipid.

Three batches of methoxide solution were prepared to confirm the result of the titration for the optimal yield of biodiesel before the commencement of the biodiesel production. 20ml of oil and 20% by volume of methanol (4ml) was measured. KOH of 0.14g, 0.6g, 1.0g were used to prepare 3 batches of methoxide solution by dissolving it in 4ml of methanol. The methoxide solutions were added to the heated oil and agitated vigorously using the magnetic stirrer. The resultant mixture was then poured into 3 different separating funnels labelled 0.14g, 0.6g, 1.0g respectively based on the amount of KOH used for each batch as shown in Figure 2. The mixture was left for 72 hours until it separated into two layers. The biodiesel on the upper and glycerol in the lower layer of the separating funnel. The glycerol was carefully separated from the biodiesel. Warm water was used to wash the biodiesel to remove any trace of methanol and catalyst which may likely to cause corrosion in the engine core if present. The process was repeated continuously until the PH value for the water was neutral. Residue water was removed from the biodiesel through heating.

Fig. 2: Biodiesel separation

III. Results And Discussion
Determination of thermophysical properties of Gmelina arborea oil and biodiesel

The quality of biodiesel is expressed in terms of its properties such as viscosity, density, flash point, FFA, acid value, cloud point, pour point, iodine value and saponification value. In Table 1, the thermophysical properties of gmelina oil and gmelina biodiesel are presented. The measurement was carried out at atmospheric pressure and temperature of 27.5°C. From Table 1, it can be seen that the viscosity and density of the gmelina arborea oil reduce after the process of transesterification which makes it suitable for use in compression ignition engine.

Table 1: Thermophysical properties of gmelina oil and gmelina biodiesel

	Gmelina oil	Gmelina Biodiesel	Method
Density (kg/m^3)	868.8	821.2	ASTM D1298
Kinematic Viscosity (mm^2/s) at 40°C	1.882	0.794	ASTM, D445
Cloud Point (°C)	2.0	4.0	ASTM D 2500
Pour Point (°C)		-1	ASTM D 97
Flash point (°C)	130	110	ASTM D 93
Color	1.5 – 2.0	0.5 – 1.0	ASTM D

The thermophysical properties of Gmelina biodiesel was compared to other biodiesel produced from inedible oil as shown in Table 2. Comparing the kinematic viscosity of gmelina biodiesel and other biodiesels from inedible vegetable oils, it can be seen that the kinematic viscosity of the gmelina biodiesel is lower which makes it more suitable for use in existing compression ignition engine without operational problems. High viscosity can plug the fuel filter and injection system in the engines (Tat and Van Garpen, 1999). The lower cloud point of gmelina biodiesel makes

it more suitable for use as fuel at low temperatures. The lower density of gmelina biodiesel will reduce the specific fuel consumption of biodiesel

when compared with other biodiesel. A denser biodiesel has higher energy content and will give better mileage and increased power.

Table 2: Comparison of thermophysical properties of gmelina arborea and other inedible vegetable oil biodiesel (Lal et al. 2010; Ogbonnaya, 2010; Atabania *et al*. 2011; Kumar *et al*. 2014)

	Gmelina biodiesel	Jatropha biodiesel	Karanja biodiesel	Polanga biodiesel
Density (kg/m^3)	821.2	865	890	872
Kinematic Viscosity (mm^2/s) at 40.0°C	0.794	4.73	5.12	4.1
Cloud Point (°C)	4.0	-	16.3	12.9
Pour Point (°C)	-1	-	14.6	3.9
Flash point (°C)	110	184	166	129
Color	0.5 – 1.0	2.5	clear	-

Comparison analysis of gmelina biodiesel and ASTM standard for biodiesel and diesel is shown in Table 3. The viscosity of gmelina biodiesel is shown to be lower than the ASTM standard for biodiesel and diesel. Hence problems related to high viscosity will not exist but the low

viscosity may result to inadequate lubrication the engine parts. The result showed that the flash point of gmelina biodiesel to be lower than the ASTM standard of biodiesel but higher than the diesel which makes it safe to handle.

Table 3: Comparison of G*melina* biodiesel with ASTM standard of Biodiesel and diesel

	Gmelina oil Biodiesel	ASTM D6751 Biodiesel	ASTM D975 Diesel
Density (kg/m^3)	868.8	Report	820-870
Kinematic Viscosity (mm^2/s) at 40.0°C	0.794	1.9-6.0	1.6-5.5
Cloud Point(°C)	4.0	Report	3^0C for winter 15^0C for summer
Pour Point(°C)	-1	Report	Report
Flash point(°C)	110	130 min	35^0C min
Color	0.5 – 1.0	3.5	3.5

Qualitative and Quantitative Analysis of Biodiesel

Quantitative and qualitative analysis of the reaction mixture was conducted using gas chromatography (GC). This

procedure is used in determining the composition of a mixture of methyl esters. The result of the gas chromatography is presented in Figure 3. The Bruker Table Top FTIR was

used to perform infrared Spectroscopy to determine the functional group present and to compare it with the standard infrared Spectroscopy of FAME and diesel.
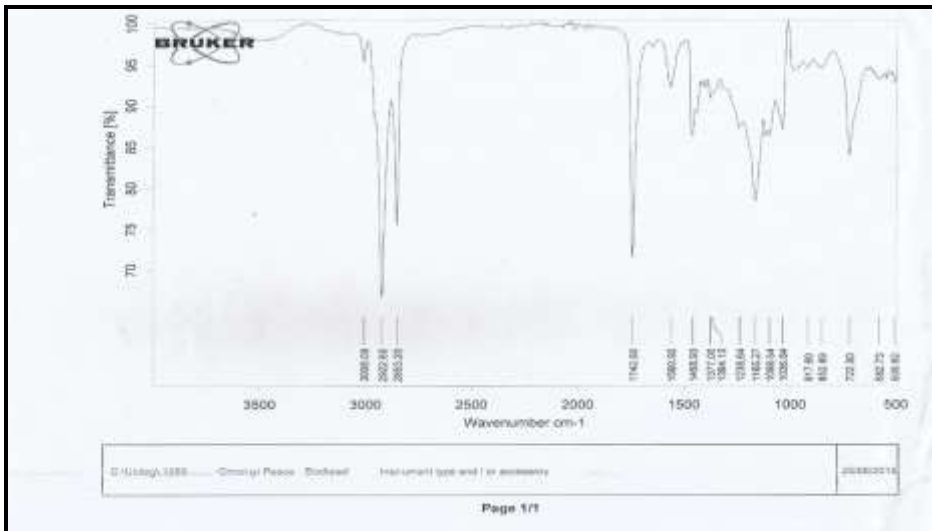
Fig. 3: Infrared Spectroscopy of Gmelina biodiesel

The infrared spectroscopy result obtained shows that the obtained product has the functional groups of FAME and matches exactly with the standard Infrared spectra of FAME as prescribed by the ASTM D7371 method.

IV. Conclusion

From the result above it can be concluded that oil from Gmelina arborea seed, which is non-edible and rarely consumed by man or animals has the potential to be used in the production of biodiesel for direct use in the internal combustion engine. This study also showed that Gmelina arborea seed has greater oil content when compared with other inedible oil seeds. Hence, it is more economical to utilize it for biodiesel production.

In order to further validate the acceptability and sustainability of gmelina arborea for use in internal combustion engine, experimental studies need to be carried out to evaluate the engine performance and emission when using different blends of biodiesel. The econometric study of biodiesels' production needs to be carried out to evaluate the cost of producing a litre of biodiesel.

References

[1] Abdullah A. Z, Razali N., Mootabadi H., Salamatinia B. (2007), Critical Technical areas for Future Improvement in Biodiesel Technologies. *IOP Publishing, Environ. Res. Lett.,* p.2.

[2] Atabania A.E., Silitongaa A.S., Mahliaa T.M.I., Masjuki H.H., Badruddin I.A. (2011), Calophyllum inophyllum L. as a potential feedstock for bio-

diesel production. *IGEC-6 – 2011 – 084.*

[3] Dennis, L. Y., Xuan, W., & Leung, M. (2009), A review on biodiesel production using catalyzed transesterification, *Applied Energy*, 1-13.

[4] FAO (2008), The State of Food and Agriculture. Biofuels: Prospects, Risks and Opportunities. http://www.fao.org

[5] Gui, M., Lee, K., & Bhatia, S. (2008), Feasibility study of edible oil vs. non-edible oil vs. waste edible oil as biodiesel feedstock. *Energy*, 46-53.

[6] Knothe G. (2005), Dependence of biodiesel fuel properties on the structure of fatty acid alkyl esters. *Fuel Processing Technology*, 1059–1070.

[7] Knothe G. and Steidley K. R. (2005), Kinematic Viscosity of Biodiesel Fuel Components and Related Compounds. Influence of Compound Structure and Comparison to Petro diesel Fuel Components. *Fuel* 84, 1059–1065

[8] Korus, R.A., Mousetis, T.L., Lloyd, L., (1992), Polymerization of vegetable oils. In: Vegetable Oils Fuel. *Proceedings of the International Conference on Plant and Vegetable Oils as Fuels, ASAE Publication* 4-82, 218–223.

[9] Kumar, A., Sharma, S (2011), Potential non-edible oil resources as biodiesel feedstock: An Indian perspective. *Renewable and Sustainable Energy Reviews*, 15, 1791–1800.

[10] Kumar D., Garg R., Tripathi R. K. (2014), Optimization of biodiesel production process from low cost high FFA Polanga (Calophyllum Inophyllum L.) oil. *International Journal of Scientific & Engineering Research,* 5(10), 695-701.

[11] Lal A., Gupta A.K., Kumar A. and Yadav Indu N.K. (2010), Manufacture and study of physico-chemical properties of Karanja bio-diesel. *Material Science Research India Vol*. 7(1), 153-158.

[12] Lin, L., Cunshan, Z., Vittayapadung, S., Xiangqian, S., Mingdong, D. (2011), Opportunities and challenges for biodiesel fuel. *Applied Energy*, 88, 1020-1031.

[13] Ma, F. and Hanna, M. A., (1999), Biodiesel production: A review. *Bioresource Technology*, 70(1), 1-15.

[14] Meng, X., Yang, J., Xu, X., Zhang, L., Nie, Q., Xian, M., (2008), Biodiesel production from oleaginous microorganisms. *Renewable Energy*, 34 (1), 1-5.

[15] Ogbonnaya M. (2010), Production of Biodiesel from Jatropha oil for use in compression ignition engines. *M.Sc Thesis, University of Lagos, Nigeria.*

[16] Refaat A. A, Attia N. K, Sibak H. A., El Sheltawy S. T., ElDiwani G. I. (2008), Production optimization and quality assessment of biodiesel from waste vegetable oil. *Int. J. Environ. Sci. Tech*., 5 (1), 75-82. A review of renewable

energy based cogeneration technologies

[17] Raj N. T, Iniyan S, Goic R. (2011), A review of renewable energy based cogeneration technologies. *Renewable and Sustainable Energy Reviews* 15, 3640–3648

[18] Schuchardt U., Serchelia R. and Vargas R. M. (1999), Trans-esterification of vegetable oils: A Review. *Journal of Brazilian Chemical Society*, 9(3), 199-210.

[19] Sharma, Y. C., Singh, B., Upadhyay, S.N. (2008), Advancements in development and characterization of biodiesel: A review. *Fuel*, 87, 2355-2373.

[20] Tat, M.E.; Van Gerpan, J.H. (1999), The Kinematic Viscosity of Biodiesel and its Blends with Diesel Fuel. *JAOCS.,* 76, 1511–1513

[21] Tesfa, B.; Mishra, R.; Gu, R.; Powles, N. (2010), Prediction models for density and viscosity of biodiesel and their

effects on fuel supply system in CI engines. *Renew. Energy*, 35, 2752-60

[22] Xue J., Grift T.E., Hansen A.C (2011), Effect of Biodiesel on Engine Performances and Emissions. *Renewable and Sustainable Energy Reviews* 15, 1098–1116.

[23] Xue JL, Grift TE, Hansen AC (2011), Effect of biodiesel on engine performances and emissions. *Renew Sustain Energy Rev* 15, 1098–1116.

[24] Yuan, W., Hansen A. C., Tat M. E., Van Gerpen J. H. and Tan Z. (2005), Spray, ignition and combustion modelling of biodiesel fuels in a DI diesel engine. *Trans. ASAE* 48(3), 933- 940.

[25] Yuan, W., Hansen, A.C., Zhang, Q., (2003), Predicting the physical properties of biodiesel for combustion modeling. *Transactions of the American Society of Agricultural Engineers*, 46(6), 1487-1493.

An Open Access Journal Available Online

Noise Level Investigation and Control of Household Electric Power Generator

Onawumi, A. Samuel[1,2], Okoli S. T. O. [2], Mfon U.[2], Raheem, W.A.[1] & Ajayeoba A. O,[1,2].

[1]Mechanical Engineering Department, Ladoke Akintola University of Technology,
[2]Mechanical Engineering Department, Covenant University, Ota. Nigeria.

Abstract - Electric power generator is an essential household facility particularly in developing countries. It is made by various manufacturers in sizes and capacities and found in business centres, offices, workshops and factories. The attendant environmental risks of this source of power supply are major challenges to users both at household and industrial level. Efforts through research and development are still ongoing to mitigate the prevailing health hazards. This study investigates noise level of typical portable generator (2 kW/220 V, 18 kg, and 370×330×320 mm) and the sound absorbance capacity of an acoustic enclosure (440×440×440 mm) developed from a multilayer panel made of locally sourced galvanized metal sheet (0.90 mm), Polyurethane acoustic foam (7.50 mm), Particle board (35.0 mm) and plywood (10.0 mm). The noise produced by the generator when on load and no load were considered for cases of it being placed inside and outside the enclosure and compared with acceptable OSHA safe thresholds noise level for the school environment where the study was carried out using Sound Level Meter HD600 (IEC 61672-1) by Extech Inc. USA. The result shows a significant reduction of noise produced indicating a shift from very laud threshold with average of 86.23 dB (A) for no load and no enclosure to moderately low noise level (average of 69.34 dB(A)) for the case of no load using enclosure. Likewise considering loaded scenario similar trend was recorded with average acoustic capacity of the enclosure of 23.20 dB(A). The effect of the enclosure was noticed and the potential benefits of improved noise absorption panels to enhance better performance of the developed enclosure for office and household generators was established.

Key Words: Electric Generator, Enclosure Panel, Noise control, Load

I. Introduction

Electric power is a major driver of any nation economy which opens viable and veritable investment opportunities to government, corporate bodies and private individual [1]. A novel product of engineering invention developed to provide continuous electric power is a device known as electric generator. The machine combines the knowledge, skills and training of mechanical, electrical and chemical engineering disciplines to develop a fossil fuel based engine which convert the chemical energy to mechanical energy and then to electrical energy [2]. The bye products of the operation of this devise are emissions in the form of CO gas and noise which create environmental hazards and constitutes challenging global menace such as greenhouse effect and disability in man [3]. Efforts are then geared towards minimising the pollutions and other negative contributions of the human invention called electric generator and to make life safer for mankind. This work considers the development of enclosure for common portable generating set used in small scale business and small households also known as "*I pass my neighbour*".

Fossil fuel energy sourced electric generator is a common household and industrial facility found in shops, homes, offices and business centers [4]. It is a major requirement for the establishment of both service and manufacturing enterprise. This technological system comes with benefits and adverse effects on human life with the emission of toxic fumes and noise which constitute pollution to the environment possess health challenges and decreases in worker's efficiency. Noise which happens to be a significant product of most mechanical or mechatronic devices has been define as undesirable or excessive sound [3]. Research efforts are being made to reduce the noise produced by technological activities, equipment, machine and large industrial facilities to the barest threshold level established by existing standard organizations and noise regulatory bodies. In Nigeria, portable power generators are the common and affordable sourced electrical power during power outage and prevents discontinuity of business activities. It is used in many cottage businesses like barbing and air dressing salon, photo studios, business centers, electrical accessory shops and other small scale one-man business outfits. It is also found in homes and hostels being used by individual tenants. The effect of noise from many units of this small sized power generator could annoying, disturbing and counterproductive particularly when they operate near schools, libraries, residential apartment, conference room, class room, examination venue, banks, small and private offices, court room, Radio and TV studio and hospitals.

Power availability has been a major challenge in Nigeria with individuals and organization always in the search for safe, reliable and economic source of energy to power their machines and appliances [5][14][16]. The introduction of 1KVA capacity into the market brought lot of relieves to low income earners Nigeria who could afford to purchase of the generator and its capacity is sufficient for their essential business or household activities [4].

However, the noise level it generates with age increases with more concern just as it is the case with other electric power generators of higher capacities. The inclusion of enclosure in the design of electric generator is known with heavy duty generator in many corporate and industrial organizations but no consideration was given to portable generator which are found more popular among low income earners in Nigeria [6]. Mitigation is said to be the measures taken to reduce the effects of noise or the noise levels on a receptor. Adverse noise effects generated by a facility can be avoided or reduced at the point of generation thereby diminishing the effects of the noise at the point of reception. The priority of noise monitoring and control is to reduce the noise at the source by engineering means once the main noise source has been verified. Noise reduction in electric motors can be achieved by the use of an absorptive silencer [7] or by redesigning the cooling fan.

Despite the extensive generation of noise in urban areas of Nigeria, surprisingly little research and documentation exist on the nature and extent of noise generation activities, their accompanying impacts and the implication for urban communities and their residents. In order to achieve sustainable urban development in Nigeria there is need to combat the main sources of noise pollution in Nigerian urban areas both at Local Government level and Federal Government level [8], [9]. Figure 1 below shows typical noise levels associated with various surroundings and noise sources [10].

Noise from electric power generators can be traced to the two major units of the power systems (Mechanical and Electrical Units) and further investigation reveal specific noise sources as Alternator, mechanical/combustion in the engine, cooling fan, structural/mechanical system, induction, and exhaust [11] [6] [12].

Several studies have considered the noise levels of electric generator and its control using enclosures padded with different absorbents [3]. Sound absorbing capacity of different material suggests the potential application in construction of walls or sound barriers. Reflective and absorbing materials such as fuzzy, porous, soft, and or thick fibre, wood, textile are potential choices for building sound barriers, panels and sound prove walls. The absorbing capacity of the developed panels made of different composites varies and these form the basis for growing research in the field acoustic material development. In this work practical approach was employed with the selection of acoustic materials which were developed into a panel for the walls of the enclosure [6]. Design consideration observed also include the heat capacity and absorption of the material and the critical components of the generating set, weight minimization of enclosure to enhance portability and cost reduction in other to ensure affordability. For the enclosure in this study, locally available acoustic materials was used and tested for performance rating.

II. Materials and Method

The enclosure is made of six panels of the same composition designed to insulate the noise from the outside environment at minimum weight and cost. The degree of reduction is enhanced by the use of the panel on all sides of the enclosure. The heat is dissipated through the vents created on the right and left sides of the enclosure. The selected materials for panel with thickness values include galvanized metal sheet (0.90 mm),
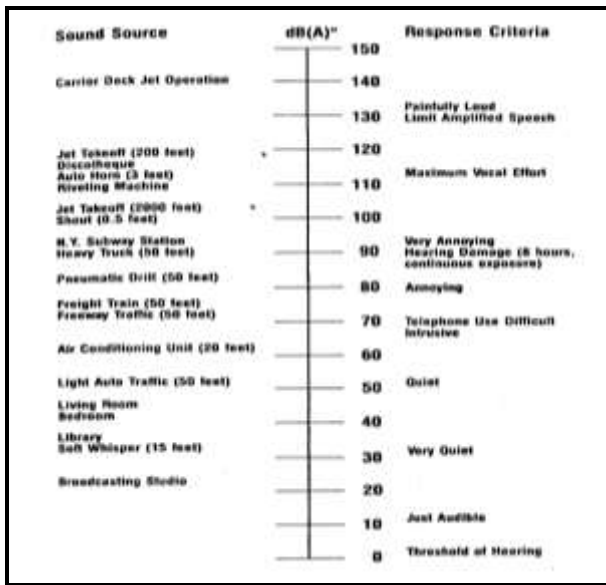
Figure 1: Typical noise level 13]

Polyurethane acoustic foam (7.50 mm), Particle board (35.0 mm) and plywood (10.0 mm) (Figure 2). Materials for the components of the panel were sourced locally with the aim of enhancing availability and improve affordability. Like wise the material used are workable using the available workshop machine tools at LAUTECH. Mechanical Engineering workshop.

Fig. 2: Multilayer Panel

A portable 2KVA electric power generator rated 950 W/220 V, 18 kg weight and 370×330×320 mm dimension (L×W×H) was considered. Six walls made of designed acoustic panel were constructed for the enclosure. A slider was introduced at the base to serve as the base to ease the placement of the generator inside the enclosure. Sufficient clearance was provided between the generator and the enclosure for necessary

circulation of air. This is assisted by four bores that were created on the slider to accommodate the shoes to fix the generation in a position and minimise movement of resulting from vibration. To avoid the risk of explosion and fire hazard that could result from excessive heat exposure during the operation of the generator the fuel (gasoline) tank was isolated from the generator and mounted on the top of the enclosure. Vents were made on the sides of the enclosure to convey heat away from the enclosure. An extension pipe was designed and made to serve as passage for exhaust gases from the enclosure. The outside dimension of the enclosure is 440×440×440 mm (Figure 3). To enhance heat absorption, the inner galvanised sheet metal was coated with black paint.

The noise level measurement was carried out using calibrated Sound Level Meter HD600 (IEC 61672-1) by Extech Inc. USA. The meter which has dimension of 278×76×60 mm and powered by either 9V battery or AC power adaptor can measure, display and data log sound pressure level (SPL) from 30 -130 dB(A) with 1.4 dB(A) accuracy (Figure 4). The meter was directed towards noise source and located from 1.0 m distance.

For evaluation of the effectiveness of the enclosure sound level were measured and recorded for

1. Ambient condition,
2. Generator noise without enclosure and
3. Noise with generator inside the enclosure.

Three different times of the day (7-9 am, 1–3 pm, 8–10 pm) were considered to monitor the contributions of environmental noise due to other activities taking place around the location of the generator. The effect of loading on the noise level variation were also recorded for on and off loading at all the time frames considered for the experiment.

Figure 3: Enclosure and 2KVA Electric Power Generator

Figure 4: Sound Level Meter HD600 (IEC 61672-1) by Extech Inc. USA.

Thermal conditions of the enclosure through the monitoring of the heat generated in the inside during the operation of the generator were also considered. A resistant thermometer was used to measure heat in the enclosure for the 45minute experiment. The experiment was repeated three times to obtain average values for the temperature.

III. Results and Discussion
The allowable noise is accepted by the National Environmental Standard and Regulation Enforcement Agency NESREA (2009). The minimum noise level was measured to be 34.5 dB(A), at ambient noise condition in the morning as shown in Tabl

Table 1: Ambient Noise Measurements

Time	Minimum dB(A)	Maximum dB(A)	Average dB(A)
7a.m- 9a.m (Morning)	34.5	49.9	42.3
1p.m – 3p.m (Afternoon)	43.9	54.5	47.0
8p.m – 10p.m (Evening)	45.4	50.5	46.6

Figures 5 and 6 showed the significant decrease in the noise level of the generator when placed in the fabricated enclosure at no load and on load conditions respectively. Noise level from the exposed single sourced generator (without load) under study ranges between 81.3 dB and 82.3 dB within a day. When the generator is placed inside enclosure the noise level dropped from the annoying threshold to near quiet range of 64.5 – 68.8 dB(A). When load is place on the exposed generator the noise levels measured ranged between 82.1 and

82.9 dB(A). With the generator properly secured inside the enclosure the noise dropped near quiet range of 66.1 – 66.5 dB(A). The ambient noise range between 42.3 and 47.0 dB(A) with maximum noise level of 47 dB(A) which occurs in the afternoon. It depicts that the domestic generator noise level category has been reduced from 'Very Loud' to 'Moderately loud'. The reduction in the category of the noise level makes it gains importance in localities where legal noise limits may not allow operation of domestic generator with 'Very

loud' categories and only for lower noise category generator. The area where the experiment was carried out was educational environment with ambient noise range of 42.3Db (A) – 47dB (A) which suggest quiet response criteria. The sound proof enclosure designed could efficiently reduce the noise level of the generator by approximately 20.1% which meets the required standard and allowable noise level in most countries. The efficiency of the sound proof enclosure is noticeably high, due to reduction in the noise level by approximately 22 dB(A). Due to the use of enclosure, the sound has decreased significantly, making the sound emitted to be at a comfortable zone and bearable to the people in the environs. The results obtained from the present (Tables 2 and 3) study show a compliance to reportedly permitted noise level in North America where maximum noise levels range from 45 dB(A) to 72dB(A), depending on the location and zoning.

The result of the analysis shows a significant noise reduction is experienced when the enclosure is in use. Considering the acceptable nose level with what was obtained in the experiment, a safer exposure to noise from the generator could be adjudged to have been achieved.
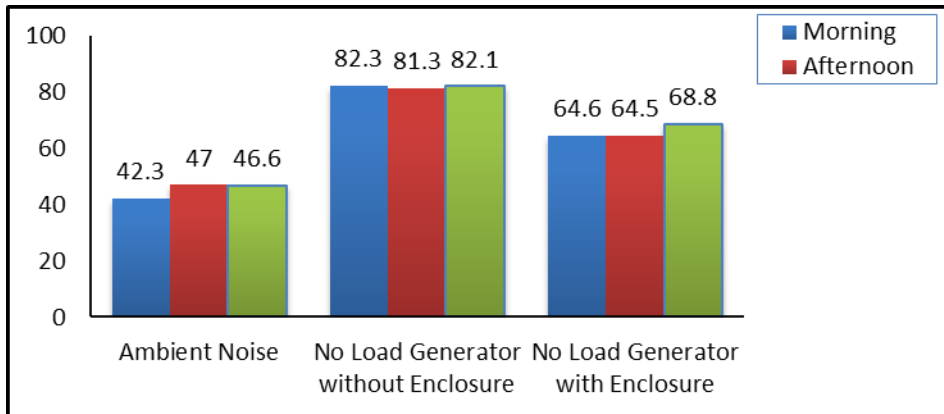

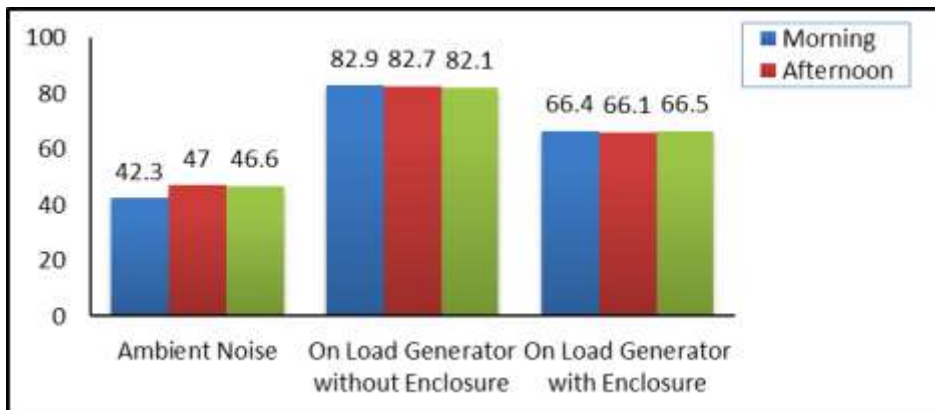Fig. 5 Sound levels distributions at no load conditions with and without enclosure

Fig. 6 Sound levels distributions when loaded with and without enclosure

In an open-air environment where the environmental noise is minimal, the highest reduction were calculated which is approximately 17.7dB(A) (21.5%) in the morning at no load condition and 16.6dB(A) (20.1%) in the afternoon at on load condition as shown in Tables 2 and 3 respectively. Investigation revealed that a well-designed and relatively airtight enclosure has the capacity of reducing noise by as much as 30 dB to 40 dB which suggests that the study has achieved about 50% of the expected attenuation potential thereby explain the need for further improvement in the design and construction effort.

Table 2 Reduction in noise Levels due to Enclosure at No Load

Time	Measurement Condition		Reduction In Noise Level	
	Without Enclosure dB(A)	With Enclosure dB(A)	Reduction dB(A)	Percentage (%)
7a.m- 9a.m (Morning)	82.3	64.6	17.7	21.5
1p.m – 3p.m (Afternoon)	81.3	64.5	16.8	20.7
8p.m – 10p.m (Evening)	86.4	68.8	17.6	20.4

Table 3 Reduction in noise Levels due to Enclosure at On Load

kTime	Measurement Condition		Reduction in Noise Level	
	Without Enclosure dB(A)	With Enclosure dB(A)	Reduction dB(A)	Percentage (%)
7a.m- 9a.m (Morning)	82.9	66.4	16.5	19.9
1p.m–3p.m (Afternoon)	82.7	66.1	16.6	20.1
8p.m –10p.m (Evening)	82.1	66.5	15.6	19.0

The temperature due to heat generated within the enclosure was observed to increase with time. The temperature-time curve shows that the heat within the enclosure is maximum (31.7^OC - 60.5^OC) in the afternoon and minimum (29.8^OC - 57.4^OC) in the evening. This explained the effect of atmospheric heat outside the enclosure on the system (Figure 7).
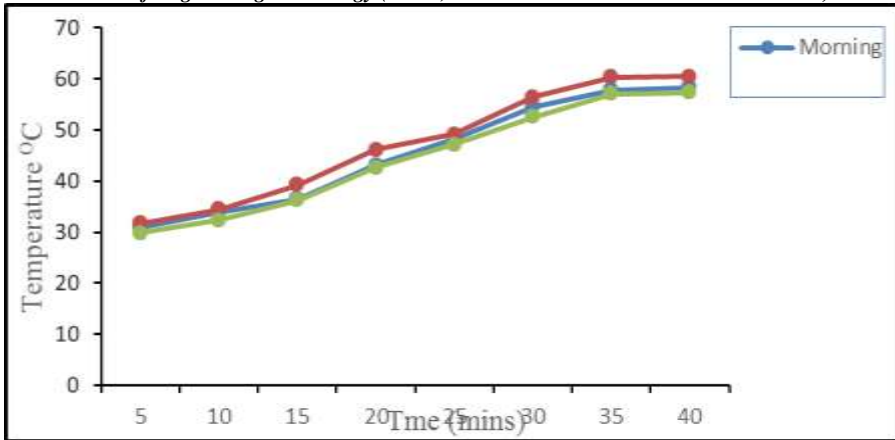
Fig. 7: Internal Thermal Condition of the Enclosure

IV. Conclusions

Noise from electric generator is considered repulsive and discouraging factor for its choice among other available power sources. With continue interest in improving the quality of life by minimizing hazard associated with human inventions at minimal cost, each effort made in respect of improved design/re-design of enclosure is expected to yield encouraging result.

Further efforts is suggested for an improved mitigation in the noise from electric generators that people live with daily at work place and residences. Likewise opportunities exist with the use of some sound absorbing wastes/scraps from textiles and other composite material in the development of acoustic panels which could improve the noise absorption propagation/dispersion.

References

[1] Sambo A. S., "Strategic Developments In Renewable Energy In Nigeria". *Proceedings at International Association for Energy Economics*, vol. 1: pp. 15-19, (2009).

[2] Stanley A .M.,. *Air Pollutant Concentration and Noise Levels from Electric Power Generators.* Seminar Presented at the seminar series of the Faculty of Environmental Design , Ahmadu Bello University, Zaria. (2010).

[3] Tandon N., B.C. Nakra, D.R. Ubhe and N.K. Killa . "Noise control of engine driven portable generator set". *Applied Acoustics,* 307 – 328. (1998).

[4] Onawumi A. S., Dunmade I.S., Ajayi O. O.,
Sangotayo E.O. and Oderinde M. O. (2016) "Investigation into House-Hold Energy Consumption in Saki, South-western Nigeria". *International Journal of Scientific and Engineering Research*, Volume 7(3) pp 720-727. (2016).

[5] Sambo, A.S., Ali, S. and Asere, A.A., (2001); "Household energy consumption in Bauchi: Metropolis and environs" *Nigeria Journal of Tropical Engineering* vol. 2, No 1 pp 44-59, (2001).

[6] Dennis. A., *Generator set noise solution: Controlling unwanted noise from on-site power system.* Technical information from commis power generation Inc Power topic no. 7015, pp 1-6, (2007).

[7] Sehrndt, G. A., Parthey, W. and Gerges, S. N. Y.. *Noise sources.* Retrieved August 3, 2012 from http://www.who.int/occupational_health/publications/noise5.pdf. (2006).

[8] Atolagbe, A.M.O and Tanimowo. *Noise Pollution in Nigeria Urban Centres. A Focus on Ogbomoso Town.* Urban Environment Sustainability: Interventions and Responses, Akure S. Publishers, pp 77-87. (2006)

[9] Evelyn, M. I. T. and Thomas, T., *Environmental Pollution In Nigeria: The Need For Awareness Creation For Sustainable Development,* 4(2), 5–10. (2013)

[10] Richard D. B.. *The Aggregate Handbook*. National Stone Association, First Edition. Alexandria VA. (1991)

[11] Jack B. E., Chad N. and Himmel P.E . "Acoustical and Noise Control Criteria and Guidelines for Building Design and Operations". *Engineered Vibration Acoustics and Noise Solutions*. (2009).

[12] Danley W., *Engine Generator Uses and Safety* (accessed 12th August, 2015) http://www.academia.edu/12098907/engine-generator. (2015).

[13] OSHA, *Noise Control-A Guide for Workers and Employers Occupational Safety and Health Administration.* Publication Number 3048. (1980).

[14] Okokpujie, K. O., Odusami, M., Okokpujie, I. P., & Abayomi-Alli, O. (2017). A Model for Automatic Control of Home Appliances using DTMF Technique. *International Journal of Scientific & Engineering Research*, 8(1), 266-272.

[15] Odia, O. O., Ososomi, S. A., & Okokpujie, P. I. (2016). Practical Analysis of A Small Wind Turbine for Domestic Use on Latitude 7.0670 N, Longitude 6.2670 E. *Journal of Research in Mechanical Engineering*, 2(11), 8-10.

Finite Element Analysis of Floating, Production, Storage and Offloading (FPSO) Vessel Subjected to Sudden Crash (Impact) Load

Olalekan H. I.[1*], Oluwole O.O.[1], Odunfa K.M.[1]

[1]Department of Mechanical Engineering,
University of Ibadan, Ibadan, Nigeria.

Abstract- The need for deep-water development and continuous exploitation of depleting shallow water reserves has spawned new forms of offshore structures like FPSO (Floating, Processing, Storage and Offloading) vessel for production and storage of oil or gas. Many offshore structures have been designed to cater for these needs but FPSO due to its storage capacity and ease of installation is suitable for smaller fields which can be depleted quickly and avoids the need for installing permanent and expensive pipelines. However, for continuous production and offloading of oil, DP shuttle tanker which has flexibility of loading and transporting oil to any destination is required since FPSO would not hold crude products for a longer period. Thus, tandem offloading operation from FPSO to DP shuttle tanker is essential. This work aimed at studying the effect of crash (impact) load on FPSO in tandem offloading operation was achieved by modeling an FPSO using SolidWorks then subjected to impact/collision at different velocities of DP shuttle tanker which ranges between 0.6m/s to 200m/s. ANSYS Explicit Dynamics was used to analyze parameters like deformation/displacement, stress and equivalent elastic strain under the impact (collision) loading. The results obtained from the simulation reveled that at DP shuttle tanker velocities 5m/s and 20m/s the crash load did not reached the damage point on both FPSO and DP shuttle tanker. At velocities above 20m/s there is a great damage after collision. In addition, as the velocity of DP shuttle tanker increases, the values of those parameters also increase. This implies that at low velocity of DP shuttle tanker in tandem offloading operation, the risk of damage after impact/collision is lesser and at velocity greater than 20m/s there is tendency of heavy damage after collision resulting to stern damage on FPSO and consequent penetration and flooding in the machine room.

I. Introduction

FPSO simply means Floating, Production, Storage and Offloading which is a ship-shaped vessel similar to trading tanker, is one of the offshore platforms currently being used in the offshore industries. The development of the offshore industry commenced with the use of fixed structures. As development accelerated with the discovery of oil and gas in deeper water, the use of floating structure have become popular and commonplace, among those floating structure is FPSO. This ship-shaped floating structure has ability to produce, store and offloading the oil but it does not have the drilling capability [1]. FPSO system represents an important solution for the exploitation of the deep-water oil and fields. The floating type of platform used designed to gather oil or gas produced from the seabed as well as from nearby platforms and to store it until the oil or the gas are offloaded onto shuttle tanker or sent through a pipeline.

The main reasons for choosing FPSO as the offshore platform are due to its storage capacity and the provision of large topsides particularly in marginal deep water fields. Offloading operations require a safe relative positioning between two vessels under the action of environmental forces such as wind, waves and current. These can subject the vessel to quartering or beam seas that can significantly influence the response of FPSO [2]. A transportable platform, FPSO vessels are popular as they can be easily moved and installed to nearby platforms and also allow for easy transportation of oil to tankers or pipelines. Once an existing field has been depleted FPSO can then be moved to other locations. This makes them suitable for smaller fields which can be depleted quickly and avoids the need for installing permanent expensive pipelines.

An FPSO vessel is fixed to a central anchoring point by means of the mooring system, which permits free rotation of the unit to account for wind and wave action. The crude oil is pumped onto the FPSO vessel through riser lines fastened to the seabed. Once on board, the oil is passed through separators to separate the gas and to remove water and sand, after which the product is stored. Typically, the tank capacity is one million barrels. At regular intervals, a shuttle tanker calls to collect the crude oil for processing ashore [3]. A Shuttle tanker is a specialized ship designed to transport oil from offshore oil field to onshore refineries. Shuttle tankers are often used as an alternative to pipelines in harsh climates, remote locations or deep waters [4].

Loads on Offshore Structures

Loads are generally estimated using the classification rules or by direct hydrodynamic calculations. The loads that an offshore Structure experiences can be roughly divided into two parts [5];

Static Loads: These consist of loads, which do not vary with time, or even if they vary, the effect of time could be neglected. The hydrostatic pressure, Weights of the offshore platform components, Cargo and

Ballast loads come under this category. In addition to these, wave moments and forces coming due to component parts are also considered as static loads.

All these loads can be group into Dead weight e.g. weights of structure in air, ballast and Hydrostatic forces.

Dynamic Loads: These are the loads, which vary with time, and the variation is substantially large because a dynamic analysis is generally required. The hydrodynamic Pressure due to waves, wind Loads and other operational loads like loads due to underwater Explosion, Machinery operational loads etc., are the loads which are considered as dynamic loads.

Dynamic loads can be group into;

Operational Loads: this includes the weights of drilling/production facilities, living quarters and forces generated from operations such as drilling and crane operation.

Environmental Loads: this includes the wind, wave, ocean current, ice, thermal and earthquake. These loads especially the wave loads usually dominate the design of offshore platform.

Construction Loads: these are the loads arising from fabrication and installation of the platform and its components.

Accidental Loads: it includes Ship collision hazards, Dropped object hazards, Fire hazards and Blast hazards. Both the above categories of loads, would act on offshore structures/vessels and its components from time to time.

Impact Load/Collision. Impact load is dynamic load i.e. it varies with time. An example is caused by ships collision. Impact occurs when one object strikes another, such that large forces are developed between the objects during a very short period of time. In ship impacts on offshore structures/vessels, the loads are governed by the kinetic energy of the striking ship. The kinetic energy may be estimated from the mass of the ship, including the hydrodynamic added mass, and the speed of the ship at the instant of impact. If the collision is non-central, a part of the kinetic energy may remain as kinetic energy after the impact. The remainder of the kinetic energy has to be dissipated as strain energy in the installation and in the vessel. Generally this involves large plastic strains and significant structural damage to the installation, the ship or both. Given that the collision event takes place, the loads and consequences of the collision event must be determined. A number of analysis tools and procedures for collision analyses have been developed and presented during the last decades.

The main concern in ship impacts on fixed platforms is the reduction of structural strength and possible progressive structural failure. However, the main effect for buoyant structures is damage that can lead to flooding and, hence, loss of buoyancy. The measure of such damages is the maximum indentation implying loss of water tightness. However, in the case of large damage, reduction of structural strength, as expressed by the indentation, is also a concern for floating structures [6].

Contact incidents between FPSO/FSU and shuttle tanker have clearly demonstrated a high

likelihood of contact between vessels in tandem offloading. The large masses involved, i.e. the high potential impact energy, make the collision risk large.

Hence it becomes essential to consider the loads correctly and analyze the structure accordingly. Use of ANSYS software which is a finite element analysis tool, makes the process of application of load very simple and manageable and also the chances of errors in combining the loads are eliminated.

Finite Element Analysis

The finite element method (FEM) is the most popular simulation method to predict the physical behavior of systems and structures. Since analytical solutions are in general not available for most daily problems in engineering sciences, least square approximation techniques and numerical methods have been evolved to find a solution for the governing equations of the individual problem [7-9]. This research investigated and analyzed the displacement/deformation, force, stress and strain on 3-D model of FPSO and DP shuttle tanker after impact/collision in tandem offloading operation using finite element analysis software known as ANSYS® Explicit Dynamics.

ANSYS® Explicit Dynamics. If your product needs to survive impacts or short-duration high-pressure loadings, you can improve its design with ANSYS® explicit dynamics. The ANSYS explicit dynamics suite enables you to capture the physics of short-duration events for products that undergo highly nonlinear, transient dynamic forces. ANSYS® explicit dynamics software is an

extension to ANSYS® structural mechanics suite, it shares the same graphical user interface (GUI), serving mechanical engineers who need to study highly complex problems especially ones with high strain rates and other complications that are difficult to solve with general-purpose implicit solution methods [10].

FPSO in Tandem Offloading Operation

The tandem offloading means that the shuttle tanker is positioned at some distance, e.g. 80 m, behind the FPSO as shown in Fig. 1. The two vessels are physically connected by a mooring hawser and a loading hose through which cargo is offloaded. The tanker may position itself by its own dynamic positioning system so that the hawser is not tensioned (DP mode), or by applying certain astern thrust and maintain a small tension on hawser (Taut hawser mode). Tug or standby vessel assistance may be required for taut hawser mode. The DP tankers have greater uptime in harsh environments and therefore are widely applied in the North Sea. FPSO and DP shuttle tanker in tandem offloading operation can in principle be summarized into the following five operational phases, from the point of view of the tanker [11].

1. Approach: tanker approaches FPSO stern and stops at a wanted distance.

2. Connection: messenger line, hawser and loading hose are connected.

3. Loading: oil is transferred from FPSO to tanker.

4. Disconnection: manifold is flushed, and loading hose and hawser are disconnected.

5. Departure: tanker reverses away from FPSO stern while sending back hawser messenger line, and finally sails away from field.
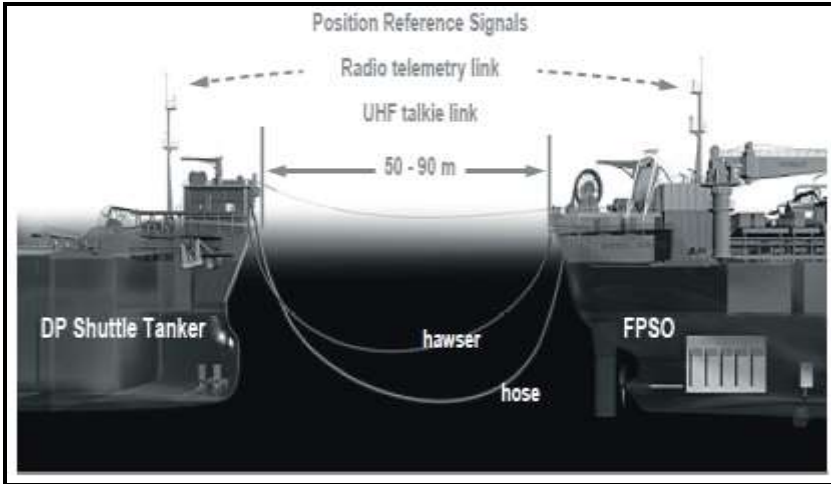
Fig.1 A Typical FPSO and DP Shuttle tanker in a tandem offloading operation

II. Methodology
Material Data
Since both the FPSO and offloading tanker are ship-like offshore platforms, structural steel, which has the building material properties for both FPSO and DP shuttle tanker, is selected. Table 1 and Table 2 show the material properties of Structural Steel.

Table 1 Structural Steel Constants

Density	7.85e-006 kg/mm^3
Coefficient of Thermal Expansion	1.2e-005 C^{-1}
Specific Heat	4.34e005 mJ/ kg C
Thermal Conductivity	6.05e-002 W/ mm C
Resistivity	1.7e-004 ohm mm

Table 2 Structural Steel Isotropic Elasticity

Temperature C	Young's Modulus MPa	Poisson's Ratio	Bulk Modulus MPa	Shear Modulus MPa
22	2.0e+005	0.3	1.6667e+005	76923

Assumptions
  i. The FPSO structure is assumed to be inside water.

  ii. The FPSO is fixed.

  iii. The DP shuttle tanker collides with the FPSO in tandem offloading operation.

iv. The Impact occurs in tandem offloading operation between FPSO to DP shuttle tanker.

Governing Equations

Considering the law of conservation of Momentum

$$M_1V_1 + M_2V_2 = (M_1 + M_2)V \qquad (1)$$

where M_1 =FPSO mass

M_2 = Offloading tanker mass

V_1= FPSO velocity

V_2= Offloading tanker velocity

V= Velocity after impact

Since the FPSO is fixed during tandem offloading operation, equation (1) becomes

$$V = M_2V_2/(M_1 + M_2) \qquad (2)$$

Impulse

$$Ft = M * V \qquad (3)$$

where F= Impact Load/force which is very high

t= time of impact which is very small

M= M_1+M_2

From eqn. (3), Impact force/load can be calculated.

To calculate the deformation/displacement, stress and equivalent elastic strain of FPSO after impact, theory of Elasticity is used [12].

Considering an infinitesimal element on the FPSO after impact as shown in Fig. 2, the summation of forces in vertical and horizontal axes gives;
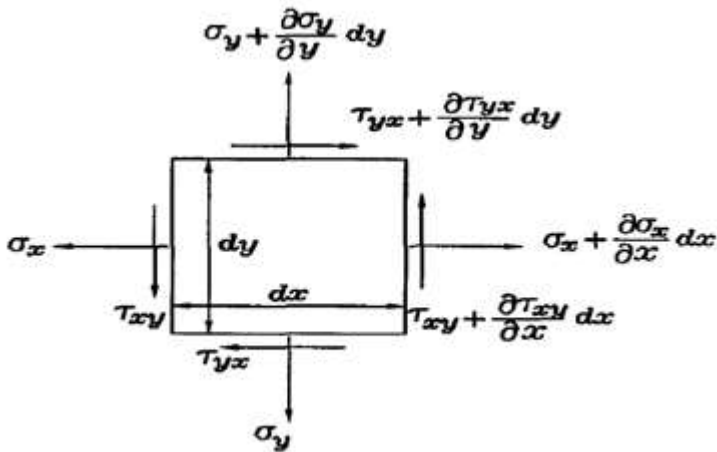
Fig. 2 Free body diagram of infinitesimal element

$$\sum F_x = \left(\sigma_x + \frac{\partial \sigma_x}{\partial x}\right) dxdy - \sigma_x dxdy + \left(\tau_{xy} + \frac{\partial \tau_{xy}}{\partial y}\right) dxdy - \tau_{xy} dxdy + f_x dxdy = 0 \qquad (4)$$

$$\sum F_y = \left(\tau_{xy} + \frac{\partial \tau_{xy}}{\partial y}\right) dxdy - \tau_{xy} dxdy + \left(\sigma_x + \frac{\partial \sigma_x}{\partial x}\right) dxdy - \sigma_y dxdy + f_y dxdy = 0 \qquad (5)$$

Simplifying eqns. (4) and (5) yield

$$\frac{\partial \sigma_x}{\partial x} + \frac{\partial \tau_{xy}}{\partial y} + f_x = 0 \qquad (6)$$

$$\frac{\partial \tau_{xy}}{\partial x} + \frac{\partial \sigma_y}{\partial y} + f_y = 0 \qquad (7)$$

For an Isotropic material, the constitutive equation which relates stresses and strains together is

$$\{\sigma\} = [D]\{\epsilon\} \qquad (8)$$

where $\{\sigma\} = \{\sigma_x \sigma_y \tau_{xy}\}^T$ denotes the stress and $\{\epsilon\} = \{\epsilon_x \epsilon_y \gamma_{xy}\}^T$ is the strain

The material property matrix

$$[D] = \frac{E}{1-v^2}\begin{bmatrix} 1 & v & 0 \\ v & 1 & 0 \\ 0 & 0 & \frac{1-v}{2} \end{bmatrix}$$ is for plane

stress condition   (9)

and

$$[D] = \frac{E(1-v)}{(1+v)(1-2v)}\begin{bmatrix} 1 & \frac{v}{1-v} & 0 \\ \frac{v}{1-v} & 1 & 0 \\ 0 & 0 & \frac{1-2v}{2(1-v)} \end{bmatrix}$$

for plane strain condition
       (10)

where *E*= Elastic Modulus
     v = Poisson's ratio

The kinematic equation which relates strain to displacement can be expressed as

$$\begin{Bmatrix} \epsilon_x \\ \epsilon_y \\ \tau_{xy} \end{Bmatrix} = \begin{Bmatrix} \frac{\partial u}{\partial x} \\ \frac{\partial v}{\partial y} \\ \frac{\partial u}{\partial y} + \frac{\partial v}{\partial x} \end{Bmatrix}$$ (11)

Where *u* and *v* are displacements in the x and y directions respectively.

Combining eqns (6), (7), (8) and (11) give eight unknowns (three stresses, three strains and two displacements) for eight equations (two equilibrium, three constitutive and three kinematic equations).

To develop the finite element formulation for the elasticity problem, apply Gallerkin's method by applying weighted residual

function to equations (6) and (7) and writing them together yield

$$\int_\Omega \begin{Bmatrix} w_1 \left(\frac{\partial \sigma_z}{\partial x} + \frac{\partial \tau_{zy}}{\partial y}\right) \\ w_2 \left(\frac{\partial \tau_{xy}}{\partial x} + \frac{\partial \sigma_y}{\partial y}\right) \end{Bmatrix} d\Omega + \int_\Omega \begin{Bmatrix} w_1 f_x \\ w_2 f_y \end{Bmatrix} d\Omega -$$
$$\int_{\Gamma_e} \begin{Bmatrix} w_1 \Phi_x \\ w_2 \Phi_y \end{Bmatrix} d\Gamma = 0$$
     (12)

Where Γ_e is the Boundary for essential condition and w_i $(i = 1,2)$ is the weighting function.

Applying integration by part to the terms in the first integral of eqn (12) gives

$$-\int_\Omega \begin{Bmatrix} \left(\frac{\partial w_1}{\partial x}\sigma_x + \frac{\partial w_1}{\partial y}\tau_{xy}\right) \\ \left(\frac{\partial w_2}{\partial x}\tau_{xy} + \frac{\partial w_2}{\partial y}\sigma_y\right) \end{Bmatrix} d\Omega + \int_\Omega \begin{Bmatrix} w_1 f_x \\ w_2 f_y \end{Bmatrix} d\Omega +$$
$$\int_{\Gamma_n} \begin{Bmatrix} w_1 \Phi_x \\ w_2 \Phi_y \end{Bmatrix} d\Gamma = 0$$
     (13)

Where Γ_n is the boundary for natural conditions and eqn (13) can be rearrange and rewritten as

$$\int_\Omega \begin{bmatrix} \frac{\partial w_1}{\partial x} & 0 & \frac{\partial w_1}{\partial y} \\ 0 & \frac{\partial w_2}{\partial y} & \frac{\partial w_2}{\partial x} \end{bmatrix} \begin{Bmatrix} \sigma_x \\ \sigma_y \\ \tau_{xy} \end{Bmatrix} d\Omega + =$$
$$\int_\Omega \begin{Bmatrix} w_1 f_x \\ w_2 f_y \end{Bmatrix} d\Omega + \int_{\Gamma_n} \begin{Bmatrix} w_1 \Phi_x \\ w_2 \Phi_y \end{Bmatrix} d\Gamma$$
     (14)

Substitution of the constitutive equation to eqn (14) gives

$$\int_\Omega \begin{bmatrix} \frac{\partial w_1}{\partial x} & 0 & \frac{\partial w_1}{\partial y} \\ 0 & \frac{\partial w_2}{\partial y} & \frac{\partial w_2}{\partial x} \end{bmatrix} [D] \begin{Bmatrix} \epsilon_x \\ \epsilon_y \\ \tau_{xy} \end{Bmatrix} d\Omega =$$
$$\int_\Omega \begin{Bmatrix} w_1 f_x \\ w_2 f_y \end{Bmatrix} d\Omega + \int_{\Gamma_n} \begin{Bmatrix} w_1 \Phi_x \\ w_2 \Phi_y \end{Bmatrix} d\Gamma$$
     (15)

Then substitution of kinematic equation to eqn (15) yields

$$\int_{\Omega} \begin{bmatrix} \frac{\partial w_1}{\partial x} & 0 & \frac{\partial w_1}{\partial y} \\ 0 & \frac{\partial w_2}{\partial y} & \frac{\partial w_2}{\partial x} \end{bmatrix} [D] \begin{Bmatrix} \frac{\partial u}{\partial x} \\ \frac{\partial v}{\partial y} \\ \frac{\partial u}{\partial y}+\frac{\partial v}{\partial x} \end{Bmatrix} d\Omega =$$

$$\int_{\Omega} \begin{Bmatrix} w_1 f_x \\ w_2 f_y \end{Bmatrix} d\Omega + \int_{\Gamma_n} \begin{Bmatrix} w_1 \Phi_x \\ w_2 \Phi_y \end{Bmatrix} d\Gamma$$

(16)

Using triangular linear element and interpolating the displacements u and v using shape function as

$$u(x,y) = \sum_{i=1}^{3} H_i(x,y) u_i \qquad (17)$$

$$v(x,y) = \sum_{i=1}^{3} H_i(x,y) v_i \qquad (18)$$

$$\begin{Bmatrix} \frac{\partial u}{\partial x} \\ \frac{\partial v}{\partial y} \\ \frac{\partial u}{\partial y}+\frac{\partial v}{\partial x} \end{Bmatrix} = \begin{bmatrix} \frac{\partial H_1}{\partial x} & 0 & \frac{\partial H_2}{\partial x} & 0 & \frac{\partial H_3}{\partial x} & 0 \\ 0 & \frac{\partial H_1}{\partial y} & 0 & \frac{\partial H_2}{\partial y} & 0 & \frac{\partial H_3}{\partial y} \\ \frac{\partial H_1}{\partial y} & \frac{\partial H_1}{\partial x} & \frac{\partial H_2}{\partial y} & \frac{\partial H_2}{\partial x} & \frac{\partial H_3}{\partial y} & \frac{\partial H_3}{\partial x} \end{bmatrix} \{d\} \qquad (20)$$

Using symbol **[B]** to denote the matrix expression in on the right hand side of eqn (20) i.e.

$$\{\epsilon\} = \begin{Bmatrix} \frac{\partial u}{\partial x} \\ \frac{\partial v}{\partial y} \\ \frac{\partial u}{\partial y}+\frac{\partial v}{\partial x} \end{Bmatrix} = [B]\{d\} \qquad (21)$$

Since Gallerkin's method states that $w_i = H_i$ (i =1, 2, 3) and $w_2 = H_i$ (i =1, 2, 3), applying these weighting functions and putting eqn (20) into

where H_i is the shape function and the displacement can also be expressed as

$$\begin{Bmatrix} u \\ v \end{Bmatrix} = \begin{bmatrix} H_1 & 0 & H_2 & 0 & H_3 & 0 \\ 0 & H_1 & 0 & H_2 & 0 & H_3 \end{bmatrix} \begin{Bmatrix} u_1 \\ v_1 \\ u_2 \\ v_2 \\ u_3 \\ v_3 \end{Bmatrix} =$$

$$[N]\{d\}$$

(19)

Where

$\{d\} = \{u_1 \quad v_1 \quad u_2 \quad v_2 \quad u_3 \quad v_3\}^T$

is the nodal displacement vector, using this expression for strains yield

eqn (16) gives for the finite element domain integral

$$\int_{\Omega^e} [B]^T [D][B] d\Omega \{d\} \qquad (22)$$

where Ω^e is the element domain and therefore the element stiffness matrix for elasticity is expressed as

$$[K^e] = \int_{\Omega^e} [B]^T [D][B] d\Omega \qquad (23)$$

Eqn (23) holds for any kind of element and dimension.
Evaluation of linear shape function provide

$$[B] = \frac{1}{2A} \begin{bmatrix} (y_2 - y_3) & 0 & (y_3 - y_1) & 0 & (y_1 - y_2) & 0 \\ 0 & (x_3 - x_2) & 0 & (x_1 - x_3) & 0 & (x_2 - x_1) \\ (x_3 - x_2) & (y_2 - y_3) & (x_1 - x_3) & (y_3 - y_1) & (x_2 - x_1) & (y_1 - y_2) \end{bmatrix} \quad (24)$$

Substituting eqn (24) in eqn (23) results in

$$[K^e] = \int_{\Omega^e} [B]^T [D][B] d\Omega$$
$$= [B]^T [D][B] A \qquad (25)$$

where A is the Area of the element.

Eqn (25) is true for both plane stress and plane strain conditions. The material properties [D] are selected for both plane stress or plane strain accordingly. A unit thickness is assumed for plane stress condition because the solution is independent of thickness direction. However the thickness can be included by multiplying the matrix by the thickness.

The Force Vector

The two right handed terms of eqn 16 are the forced vector. The first is the term due to body force which is zero since there is no initial force before impact and the other is due to tractions which is the Impact force *F* that is gotten from the impulse formula in eqn (3). Therefore the governing eqn for this project work is

$$[F] = [K][U] \qquad (26)$$

where *[F]* is the Impact/ load force as in eqn. (3)

$[K]$ is $[K] = \int_{\Omega^e} [B]^T [D] [B] d\Omega$
$= [B]^T [D] [B] A$

Stiffness matrix

$[U]$ is
$\{d\} = \{u_1 \quad v_1 \quad u_2 \quad v_2 \quad u_3 \quad v_3\}^T$

Deformation / Displacement

Analysis Procedures

The procedures include a 3D model of both FPSO and DP shuttle tanker using SolidWorks which was then imported into ANSYS Explicit Dynamics for analysis as shown in Fig. 3-6. Assumed masses of 50000000kg and 30000000kg were added to both FPSO and DP shuttle tanker respectively. The geometry was discretized into 5880 elements with 2901nodes when meshed. The FPSO is fixed while the DP Shuttle tanker is dynamically positioned with velocities ranging from 0.6m/s to 200m/s as the initial condition. The end time of impact, number of cycles and time step safety factor are set as 0.05seconds, 100000000 and 0.9, respectively. All other parameters were set as program controlled in the analysis settings before solving. After the establishment of analysis settings, explicit dynamic solver (AUTODYN) utilized these data in solving the total deformation/deflection, elastic strain and equivalent stress on the FPSO after impact.
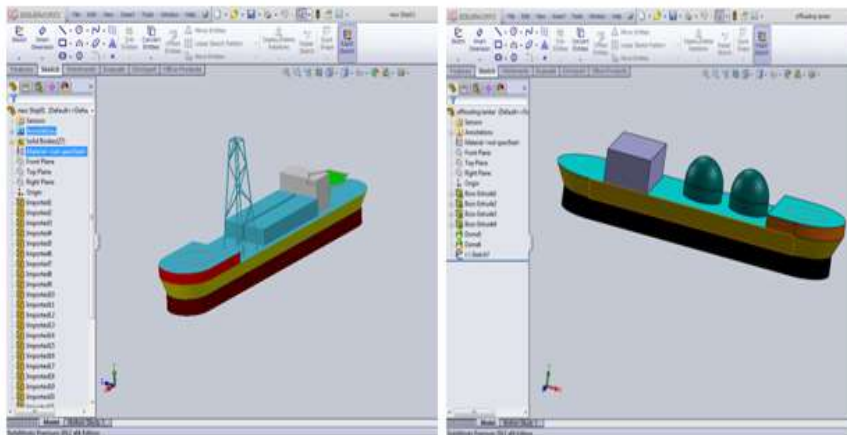

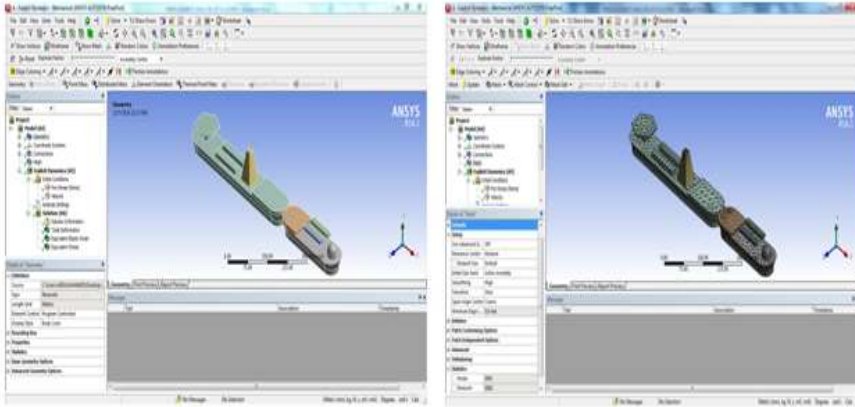Fig. 3 Geometry of Both FPSO and DP Shuttle Tanker in SolidWorks
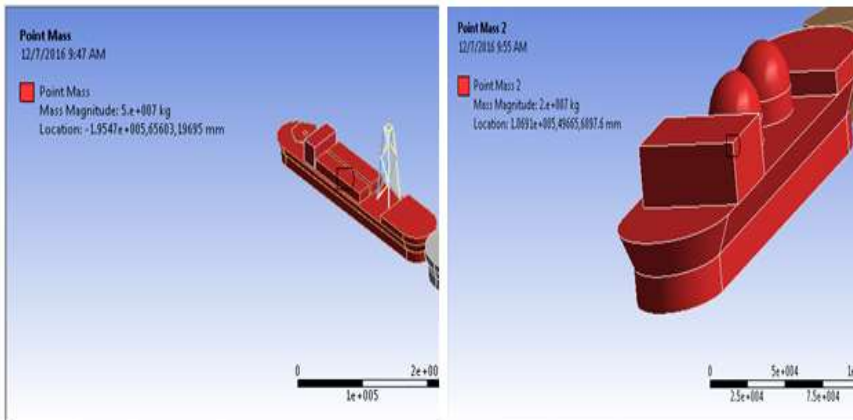
Fig. 4 Model Imported into ANSYS and Meshed

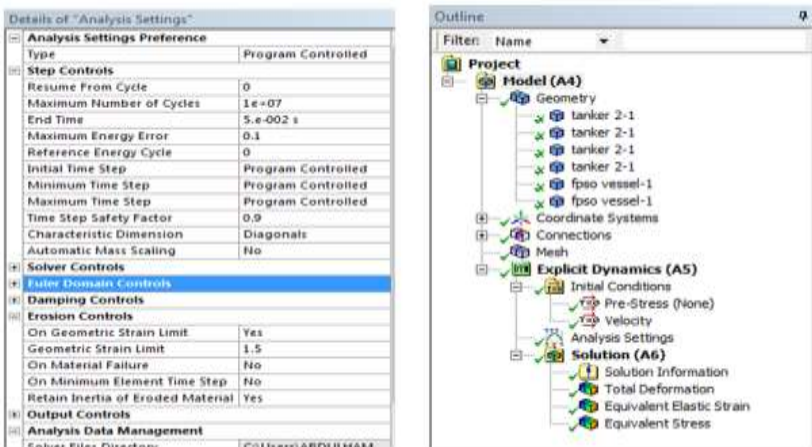Fig. 5 Masses Added to Both FPSO and DP Shuttle Tanker

Fig. 6 Analysis Setting and the Project Tree showing Solution Information

III. Results and Discussion

The results obtained from the analysis which include, the deformation/ displacement resulting from the impact, equivalent elastic strain and equivalent stress after the collision or impact, are presented as follows.

Effect of DP Tanker velocity on deformation/displacement

As obtained in Table 4, FPSO at velocity of 5m/s has no deformation since it is fixed and that the collision is initiated by the DP shuttle tanker with a maximum deformation/ displacement of 341.58mm. This is an indication that before impact (at time t=0) there is no displacement. As the time of collision increases the deformation/ displacement increases until all the energy generated due to collision is lost. Thus, the result obtained in table 5 revealed that the DP shuttle tanker has a maximum deformation/ displacement of 770.98 mm at velocity of 20m/s while the FPSO remained fixed. This indicates that as velocity increases the deformation also increases (Fig. 8).

Table 4 Solution Results at velocity v= 5m/s

Definition					
Type	Total Deformation	Directional Deformation		Equivalent Elastic Strain	Equivalent (von-Mises) Stress
Orientation		X Axis	Y Axis		
Coordinate System		Global Coordinate System			
Results					
Minimum	0. mm	-1.4741e-004 mm	-142.25 mm	1.9944e-007 mm/mm	1.6572e-002 MPa
Maximum	341.58 mm	323mm	136.01 mm	8.9638e-004 mm/mm	177.54 MPa
Minimum Occurs On	fpso vessel		DP Shuttle tanker		
Maximum Occurs On		DP Shuttle tanker		fpso vessel	

Table 5 Solution Results at velocity v= 20m/s

Definition					
Type	Total Deformation	Directional Deformation		Equivalent Elastic Strain	Equivalent (von-Mises) Stress
Orientation		X Axis	Y Axis		
Coordinate System		Global Coordinate System			
Results					
Minimum	0. mm	-1.8548e-004 mm	-93.091 mm	3.8361e-007 mm/mm	7.3299e-002 MPa
Maximum	770.98 mm	765.32 mm	157.32 mm	1.3063e-003 mm/mm	247.48 MPa

| Minimum Occurs On | fpso vessel | DP Shuttle tanker | |
| Maximum Occurs On | DP Shuttle tanker | | fpso vessel |
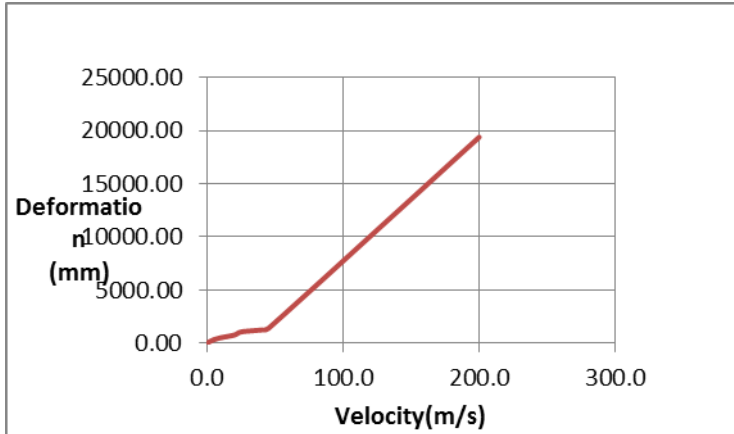
Fig. 8 Plot of Maximum Deformation/displacement against velocity

Effect of DP Tanker velocity on elastic strain

From Table 4, the minimum and maximum strains values of 1.9944e-007 and 8.9638e-004 occurred at the DP shuttle tanker and FPSO, respectively at 5m/s. This has no significant effect on the elastic strain since the value of the velocity is too small. The FPSO is having the maximum value because it is a relatively fixed vessel compared to the DP shuttle tanker during impact and also it is the DP shuttle tanker that is colliding with the FPSO.

In addition, the minimum and maximum strains values of 3.8361e-007 and 1.3063e-003 as observed in Table 5 occurred at the DP shuttle tanker and FPSO, respectively at 20m/s. This implies that as velocity increases, the elastic strain also increases (Fig. 9).
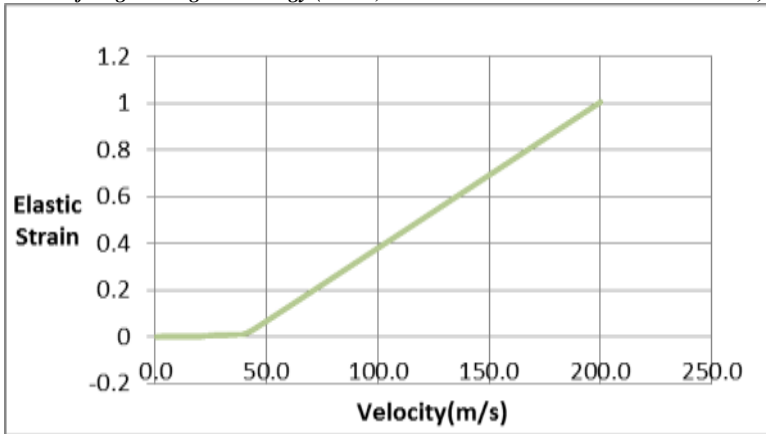
Fig. 9 Plot of Equivalent Elastic Strain against Velocity

Effect of DP Tanker velocity on equivalent stress

From Table 4, the minimum and maximum stress values of 1.6572e-002 MPa and 177.54 MPa is occurring at DP shuttle tanker on the FPSO. This value (177.54MPa) is smaller compared to 250MPa which is the yield strength of the material at 5m/s. Therefore at velocity of 5m/s the both the FPSO and the DP shuttle tanker will not have massive crash.

In addition, the minimum and maximum equivalent stress values of 7.3299e-002 MPa and 247.48 MPa is obtained at DP shuttle on the FPSO as observed in Table 5 at 20m/s. This value (177.54MPa) is almost equivalent to 250MPa which is the yield strength of the material that both FPSO and DP shuttle tanker is made-up. Therefore at velocity of 20m/s the both the FPSO and the DP shuttle tanker will not yield or fail massively. Thus as velocity increases, the equivalent stresses also increase (Fig. 10).
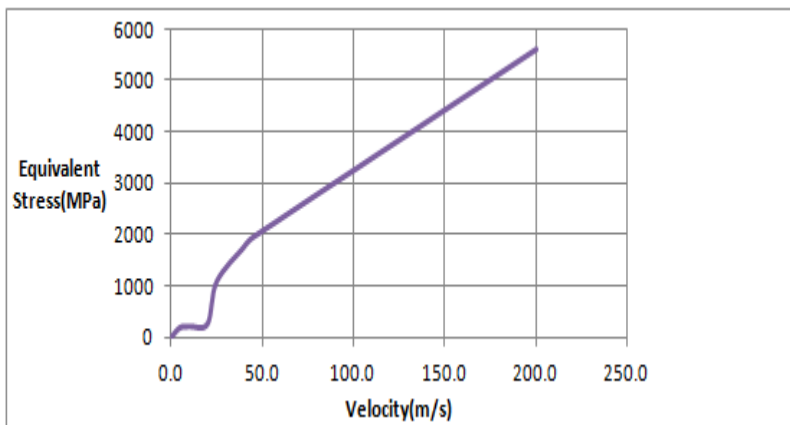
Fig. 10: Plot of Maximum Equivalent Stress against velocity

Effect of velocity above 20m/s on displacement, strain and equivalent stress

Table 6 shows the maximum values of deformation/displacement, equivalent stress and equivalent elastic strain at different velocities of DP shuttle tanker result after simulation. It can be seen that from v=25m/s and above the outcome for maximum deformations/deflections, maximum equivalent stresses and maximum equivalent elastic strains are relatively high and also as the velocity increases from v=25m/s there is significant increase in the values of deformation/displacement, equivalent stress and equivalent elastic strain. This is substantiated with Fig. 8-10.

In summary, the results generated using velocities 5m/s and 20m/s showed that there are no significant deformation/displacement on both FPSO and DP shuttle tanker at velocities of 0.6m/s and 1.0m/s. Also above 20m/s, the results outcomes for equivalent stress have exceeded the yield strength of the material for both vessels. The application of this could be found in RPG (Rocket Propelled Grenade). For instance, when RPG is fired at FPSO at a speed of 200m/s will cause a great damage.

Table 6 Different DP Shuttle Tanker Velocities Considered For Simulation

Velocity (m/s)	Maximum Total Deformation (mm)	Maximum Equivalent Stress (MPa)	Maximum Equivalent Elastic Strain
0.6	30.00	13.31	0.00003773
1.0	102.46	25.79	0.00009841
5.0	341.58	177.54	0.0008964
10.0	516.78	201.89	0.0010569
20.0	770.98	247.48	0.0013063
25.0	1068.30	1072.60	0.005412
40.0	1246.20	1747.90	0.01147
45.0	1398.90	1938.22	0.03621
200.0	19405.77	5592.00	1.0049

IV. Conclusions

This research work has analyzed the deformation/displacement, equivalent stress and equivalent elastic strain developed in crash (impact) load between FPSO and DP shuttle tanker in tandem offloading operation. ANSYS Explicit Dynamics was used to analyze those parameters and the results obtained reveled that at DP shuttle tanker velocities 5m/s and 20m/s the crash load did not reached the damage point on both FPSO and DP shuttle tanker. At velocities above 20m/s there is a great damage after collision. In addition, as the velocity of DP shuttle tanker increases, the values of those parameters also increase. This implies that at low velocity of DP shuttle tanker in tandem offloading operation, the risk of damage after impact/collision is lesser and at velocity greater than 20m/s there is tendency of heavy damage after collision resulting to stern damage on FPSO and consequent penetration and flooding in the machine room.

References

[1] Mohamad Shaiful, M. Z. and Agoes, P. *Analysis of Motion on FPSO in Shallow Water with a Non- Collinear Environment.* Malaysia : International Society of Ocean, Mechanical and Aerospace Scientists and Engineers, 2013.

[2] Islam, M. Y., Malik, A. A., and Kamal, M. Simulation of Current Forces on Floating Production Storage and Offloading in Irregular Computational. s.l. : Sharif University of Technology., 2010.

[3] Royal Belgian Institute of Marine Engineers. THE BASICS: What is an FPSO? [Online] 2017. www.gl- nobledenton.com.

[4] Rigzone. How do shuttle tankers work? [Online] 2017. www.rigzone.com.

[5] American Bureau of Shipping. *Accidental Load Analysis and Design for Offshore Structres.* Houston, Texas, USA : American Bureau of Shipping, ABS, 2013.

[6] Fricke, W. and Bronsart, R. *Damage Assesment Following Accidents.* Rostock, Germany : Schiffbautechnische Gesellschaft, 18th International Ship and Offshore Structures Congress . ISBN 978-3-87700-131-{5,8,.2012.

[7] Oluwole, O.O. *Finite Element Modeling for Materials Engineers using MATLAB®.* London, UK : Springer, 2011.

[8] AK, Ezugwu Chinedu. "Stability Analysis of Model Regenerative Chatter of Milling Process Using First Order Least Square Full Discretization Method." *International Journal of Mechanics and Applications* 6.3 (2016): 49-62.

[9] Nwoke ON, Okokpujie IP, Ekenyem SC. INVESTIGATION OF CREEP RESPONSES OF SELECTED ENGINEERING MATERIALS. Journal of Science, Engineering Development, Environmen and Technology (JOSEDET). 2017;7(1):1-5..

[10] ANSYS, Inc. Explicit Dynamics. [Online] 2011. www.ansys.com.

11] Haibo, C. *Probabilistic Evaluation of FPSO-Tanker Collision in Tandem Offloading Operation.* Trondheim – Norway: Department of Marine Technology, Norwegian University of Science and Technology, 2003.

[12] Young, W. K. and Hyochoong, B. *The Finite Element Method Using Matlab.* USA : CRC Press LLC, 1997. pp. 307-322. 0-8494-9653-0.

An Open Access Journal Available Online

Electronic Fare Collection Systems in Public Transits: Issues, Challenges and Way-Forward

O. N. Omoruyi[1], M. G. Omoruyi[2], K. O. Okokpujie [3] & I. P. Okokpujie[4]

1,3Department of Electrical and Information Engineering,
Covenant University, PMB 1023, Ota, Nigeria.
2National Centre for Technology Management (NACETEM),
Federal Ministry of Science and Technology,
PMB 012, OAU, Ile-Ife, Nigeria
4Department of Mechanical Engineering,
Covenant University, P.M.B 1023, Ota, Ogun State, Nigeria
*kennedy.okokpujie@covenantuniversity.edu.ng

Abstract— With an estimated 174 million in 2013, Nigeria is faced with innumerable challenges. One of such challenges is ensuring that public transit systems within its metropolitan areas are fast and effective. Our system of interest is the Bus Rapid Transit (BRT) system. This paper looks at the present challenges in deploying Electronic Fare Collection Systems for the Bus Rapid Transit (BRT) system in Lagos state, Nigeria. The study sampled commuters with questionnaires administered using a simple random sampling technique. The study also interviewed a representative of the Electronic Fare Collection System Technology Provider (e-Purse). Findings revealed commuter's adoption of Electronic Fare Collection System remains low due to amongst other factors a lack of knowhow on the smart card usability. We propose an extended technical requirement for the Fare Collection system as well as modifications of the Lagos BRT policies that will ensure its effectiveness.
Keywords: Bus Rapid Transit, Commuter Electronic Fare Collection System, Architecture, Hardware, Software, Fare Estimation.

I. Introduction

Urban spaces and cities are characterized by multi-modal transit networks because of the growth in population within respective

94

locations. Modes like Bus Rapid transit, Light rail transits, Ferry services etc. serve millions worldwide within their cities. City authorities worldwide are in a search for every sustainable means to fend off congestion and manage mobility of people. Lagos Nigeria is not left out of the race. With a population of over 20 million, it's the largest urban enclave in Nigeria. In Lagos, the efforts to ensure seamless mobility are championed by the Lagos Metropolitan Area Transport Authority (LAMATA). LAMATA so far has deployed a number of solutions within a brief period of time. This includes the BRT lite (an abridged Bus rapid Transit scheme for ease of movement) and the soon to be on-stream Light rail Transit (LRT) scheme. The Lagos BRT has proven to be a success, currently serving an estimated 80 million passenger traffic yearly. Lagos state, often times referenced as a mini-Nigeria, is noted for its Urban-City-State nature. More so, the emergence of BRT makes available an alternative to curb the challenges posed by public transits in Lagos State. For a BRT system to be effective, the system must be able to provide efficient services and as well possess adequate institutional and regulatory framework. One of the ways in which effectiveness can be achieved is through the enhancement of its Electronic Fare Collection System which adopts the use of Smart Card technology for fare payment by commuters. Studies have revealed that the use of the Electronic Fare Collection system has been largely successful in other climes due to factors such as; pricing, convenience, accessibility of Tap-to-pay

devices, publicity and marketing of smart cards, availability of top-up vendors, etc. However, the existing Electronic Fare Collection System in Lagos State still pales in comparison to other known systems worldwide (Osemwegie et al, 2016; Azeta et al, 2016; Nwoke et al 2017, Salawu et al 2018, Okokpujie et al 2017; Ezugwu et al 2016).

This study is structured as follows: Section 2 presents an overview of the Lagos BRT system which includes; its routes, interacting parties and players, smart card technology in use for its electronic fare system and the fare policies and structure used. The peculiarities of implementing and operating the Lagos BRT Electronic Fare Collection System are discussed. Some attention is paid to the system's hardware design, software or information system architecture. Section 3 discusses the methodology used in evaluating the BRT fare payment system. Section 4 Highlights findings and discusses the relevant data retrieved from the survey. Section 5 proposes recommendations based on the findings and concludes on the study.

II. Overview of the Lagos BRT

The Lagos BRT Lite system functions on a 22km corridor and about 65% of the route is physically isolated from the usual roadway with about 20% separated by road marking (Mobereola, 2009). Reforms beyond those in the infrastructure also play a crucial role in making this system a success, including a holistic approach with reorganization of the bus industry, financing new buses, creating a new institutional structure and regulatory framework to support the system, and training the personnel needed to drive, maintain, enforce,

and manage the BRT-Lite system (Mobereola, 2009). BRT Lite is a compromised BRT scheme that falls short of expected standards but still fills the gap. BRT consists of 7 elements which are: Running way, Stations, Vehicles, Services, Route Structure, Fare Collection and Intelligent Transport Systems (Levinson et al, 2002). This has been further expanded by the BRT Standard 2014 to include BRT Basics, Communication, Service Planning, Infrastructure, Stations and Access Integration. (See Table 1 for sub-elements, their description and a checklist of their presence in BRT lite).

Service Element	Sub elements	Presence in BRT lite
BRT Basics	Dedicated Right-of-Way	
	Busway Alignment	*
	Off-board Fare Collection	**
	Intersection Treatments	
	Platform-level Boarding	***
Communication	Branding	
	Passenger Information	****
Service Planning	Multiple Routes	
	Express, Limited, and Local Services	
	Control Center	
	Located in Top Ten Corridors	
	Demand Profile	
	Hours of Operations	*****
	Multi-corridor Network	
Infrastructure	Passing Lanes at Stations	
	Minimizing Bus Emissions	
	Stations Set Back from Intersections	******
	Centre Stations	
	Pavement Quality	
Stations	Distances Between Stations	
	Safe and Comfortable Stations	*******
	Number of Doors on Bus	
	Docking Bays and Sub-stops	
	Sliding Doors in BRT Stations	
Access Integration	Universal Access	
	Integration with Other Public Transport	********

	Pedestrian Access	*********
	Secure Bicycle Parking	
	Bicycle Lanes	
	Bicycle-sharing Integration	

* Busways that ** 60% of routes that touch the *** 100% of buses are **** Up-to-date static passenger ***** Late-night service. no

****** 75% of ******* Some stations on ******** Integration ********* Good, safe pedestrian

Highlighted as the first BRT scheme in sub-Saharan Africa, the Lagos BRT route commenced operation on March 17, 2008, in Lagos, Nigeria (Mobereola, 2009). The first phase was the Mile12 to Tafawa Balewa Square (TBS) depicted in the figure 1 and figure 2.

Figure: 1 The First Phase of BRT Route in Lagos
Source: Mobereola (2009)

This is a 22Km BRT corridor. A second Phase was completed in 2015 from Mile 12 to Ikorodu bringing the total mileage to 37 Kilometres. The

Lagos BRT runs a 16-hour operation from 6.00 am to 10.00 pm while the bus has a maximum seating capacity of 47.

Figure 2: The BRT Corridor Source: *LEDS (2016)*

The Lagos BRT operates both a paper ticket and an Electronic fare collection system. Tickets and e-fares are sold using a zonal fare structure. A total of 460 buses as at March 2016, were in operation in the BRT corridor. However, daily operations may require fewer than this total number. The daily usage of the BRT corridor by commuters is estimated to rise to 400,000 (Guardian Newspaper online, 2015).

Lagos BRT Electronic
Fare Collection System

The Lagos BRT Electronic Fare Collection System first started operation in July 2013, however this was discontinued two years later after a disagreement between the Bus Operators (NURTW BFS) and the technology providers (e-Purse). The technology providers attribute this to a breakdown in relationship between them and the erstwhile bus operators. However, Electronic Fare Collection System was reintroduced in November 2015 after the old bus operators were replaced and the right to use the BRT routes transferred to new bus operators. The new operators

promptly reintroduced the electronic fare collection system and approved vendors for paper tickets tied to the smart card technology.

The electronic fare collection system uses contactless smart cards with tap-to-pay devices. In the contactless smart card the chip can be completely embedded within plastic, but is usually visible. A small antenna is also installed in the contactless card, which makes smart card technology similar to radio frequency identification (RFID) technology (Pelletier et al, 2011). Smart cards usually don't contain passenger details and thus are limited in use to payment transaction. This makes them susceptible to theft and other security concerns. The electronic fare collection system operates as an on-board fare collection system using the zonal fare structure. With zonal based system, prices depend upon the number and type of zones, for which the ticket is valid (Urbanek, 2015). Electronic fare collection operators (e-Purse) noted that security and power supply concerns as the determining factor for

98

its choice of an on-board fare collection system. Tap-to-pay devices are Liquid Crystal Display (LCD)-equipped, Personal Computer (PC)-Linked, Near Field Communication (NFC) Contactless Reader with USB as its host interface. It is developed based on the 13.56 MHz RFID technology and the ISO/IEC 18092 standard (Advanced Card Systems Holdings, 2016, Okokpujie et al, 2016, Okokpujie et al, 2017, Obiazi et al, 2009). These devices are not insured and thus Technology operators incur losses when devices are damaged, stolen or destroyed.

Interacting Parties

The Lagos BRT fare collection system has a number of parties in close interaction which participate in fare price modelling and policy making. This consists of the Regulator (LAMATA), the bus operators (Primero or BFS), Funding Bank (Sterling Bank Plc), Technology providers/operators (e-Purse) and ticketing and card sales vendors and dealers.

Fare tables are decided upon by the close interaction between the Regulator and the Bus Company. This fare tables are the guiding template for the technology operators in setting the pricing policy in operation on BRT routes. Unlike its past operations, all fare is paid using either technology operator terminals or smart cards. Charge units that are retailed to commuters using pay terminals and smart cards. In the case of paper tickets, a token is printed indicating charge units purchased. Funding banks are also interacting parties (or elements) within the Lagos BRT fare collection system. Funding banks provide a means of remission of funds from approved vendors.

Approved vendors are entitled to pre-negotiated fees, technology operators are also paid via funds remitted.

III. Methods

This study was conducted in Lagos metropolis, in Lagos State Nigeria. Lagos is the sixth largest and fastest growing city in Nigeria and the Lagos metropolitan area has a population estimated at between 15 and 18 million. It is projected to go beyond 25 million by 2025, making Lagos the third largest agglomeration in the world, after Tokyo and Mumbai. The Lagos metropolis is made up of 16 local government areas which includes both the Islands of the former municipality of Lagos and the Mainland suburbs with a land area of about 999.6 km2 (Somuyiwa and Adebayo, 2009). In Lagos, road transport dominates more than 90% of all intra-urban movement (Oni, 2004). The Lagos BRT Lite System which is Africa's first Bus Rapid Transit Scheme in sub-Saharan Africa has proved a most effective public transit scheme as it conveys about 800, 000 commuters daily and about 20 million passengers annually. The Lagos BRT is based on existing BRT models such as the one in Bogota and Colombia (Mobereola, 2009).

The primary sources of data for this study included the use of questionnaire and guided oral interview. The study sampled about 55 BRT commuters which cuts across passengers going to Fadeyi-Ikorodu route, Fadeyi-Mile12 route and Ojota-Fadeyi route using a simple random sampling technique. The questionnaire was divided into three sections in which the first section elicits information on the socio-economic characteristics of the

respondents while the second section elicits information on commuter awareness of the BRT system and adoption of the electronic fare collection system (i.e. the e-Purse ticketing system). The third part of the questionnaire elicits information on commuters' perception of the e-Purse card payment system. A comparison of commuters' adoption of electronic ticketing system on commuters' satisfaction with the services provided by the electronic fare collection provider (e-Purse) in Lagos BRT system was done; using a five point Likert Scale ranging from 'very satisfied' to 'very dissatisfied'. Data generated was analyzed using Special Package for Social Sciences (SPSS). The study also interviews an Electronic Fare Collection Technology Provider (e-Purse) to obtain information on the technological capacity, innovation and challenges since the implementation of the Electronic Fare Collection System. Data was also obtained from secondary sources such as; the sub-Sahara Africa Policy Program report, journals, and other relevant publications.

IV. Results and Discussion

Socio-Economic Characteristics of Respondents:

The survey revealed that more male commuters (63.6%) use the Lagos BRT as compared to female commuters (36.4%). This is in agreement with the findings of Okagbue et al. (2015). Majority (65.4%) of the commuters are about 30years of age, which implies that younger individuals make more use of the Lagos BRT services than the older ones. BRT operators can redesign its policies and make available features that will attract or increase the older populations' patronage. More so, most (70.4%) of the Lagos BRT commuters are low income earners as their monthly income is far below N100,000. The reason for this is not far-fetched as most of the commuters are young individuals who might just be at the very early stage of their career and therefore may not have enough money to own a car. Policies relating to fare structure to accommodate more low-income earners should continue to be in the forefront of the thinking of Regulatory authorities.

Lagos BRT System Awareness and Usage:

All respondents surveyed demonstrated high level awareness of the existence of Lagos BRT system. Most (74%) of them became aware of the Lagos BRT system not less than four years ago and only a few (26%) became aware of the Lagos BRT system within the last three years. Thus, implying that majority of the Lagos dwellers are aware of the existence of Lagos BRT system. Despite the level of awareness, about 43% of the respondents use the BRT services not more than ten times monthly. This implies that most commuters are yet to deploy the services of the Lagos BRT as a major means of transportation daily. About 31.5% of commuters surveyed uses the BRT services at most once daily and about 22.2% of the respondents use the BRT services at most twice daily. This result shows the intensity of usage of the BRT could still be considerably improved upon, with only about 43% of the commuters using the services of the Lagos BRT not more than ten times monthly. This therefore implies that most commuters still use other transport

mediums such as Danfo (mini-buses deployed for transportation in Lagos), Molue (old express-buses deployed for transportation in Lagos), taxi or individual's own car which is the reason for the high-traffic congestion and environmental pollution emanating from the exhaust pipes of this fleet of automobiles presently experienced in the Lagos metropolis.

Interestingly, most (50%) of these commuters use the services of the Lagos BRT as a means to get to their workplace and only about 7.4% of them still uses the Lagos BRT to get back home after work. This implies that commuters prefer to board the BRT to their workplace as it is timely and faster than other public transit vehicles. This may be connected to the dedicated right of way feature of the BRT that makes it easy to avoid traffic congestions and to convey passengers faster and these findings is in accordance with Okagbue et al. (2015) findings. Most of the commuters indicated their use of the BRT services between the hours of 6:00am and 9:00am. The main reason is that this is usually the period that most office workers leave home for their workplace.

Adoption and Perception of the Electronic Card Payment System (e-Purse)

On the adoption of the electronic card payment system (i.e. e-Purse card); only about 16.3 % of the respondent indicated their ownership of an e-Purse card. Of this few that possesses an e-Purse card, majority of them indicated that hey last used their card two years ago and some couldn't even remember when their e-Purse card was last used. However, about 83.7% of the respondents do not own an e-Purse card. A major reason for

this is their lack of understanding of how electronic card payment system works and their lack of knowledge of where e-Purse card can be purchased. Only a few of the commuters indicated their unawareness of the existence of an e-Purse card payment system. This implies that majority of the BRT commuters are aware of the e-Purse card payment system yet the level of adoption is still very low due lack of adequate enlightenment campaign to educate the commuters on the usability and accessibility of the e-Purse card by the technology providers (i.e. the BRT operators and e-Purse). This implies that there is an urgent need for the technology providers (e-Purse) to effectively enlighten the BRT commuters on the usage, accessibility and benefits of e-Purse card payment system so as to encourage increased adoption of the electronic card payment system.

On commuters' perception of e-Purse card payment system; of the few commuters that possesses the e-Purse card, about 57.1% indicated having problems using the card. The major challenges faced by the commuters in using the e-Purse is that only few Lagos BRT had the e-Purse card machine installed in them and commuter's inability to access where recharging their e-Purse card could be done easily. Other challenges include; cash loaded on e-Purse card is less than amount credited to the card, cash deducted from the card more than the actual bus fare, and the fact that e-Purse card machines are usually turned off in most BRT buses that has this facility. Despite these array of challenges, most (65%) of the commuters still indicated their preference for the e-Purse card payment system to the paper ticketing

system if the e-Purse card payment system is adequately improved upon by the technology provider. Quite a number of the respondents (56%) indicated their satisfaction with the services of the Lagos BRT (in terms of Ticket sales, ticket inspectors and drivers). This implies that most Lagos BRT commuters are satisfied with the BRT services provided to them and this was also affirmed by Okagbue et al. (2015).

Relationship between Smartcard (e-Purse Card) Usage and Commuters' BRT Travel Frequency /BRT Service Satisfaction

The study examined the relationship between commuters' Smartcard usage and the frequency with which commuter's travel using BRT. This was done to know if Smartcard usage is associated with BRT travel frequency. The study shows a weak positive association between Smartcard usage and BRT travel frequency (r = 0.091). This implies that increase in BRT travel frequency is not likely to bring about a significant increase in Smartcard usage. From the table 2 below, this is not statistically significant (P > 0.05), hence there is no real evidence that increase or decrease in Smartcard usage relates to increase or decrease in BRT travel frequency. Also, the study examined the relationship between e-Purse card usage and commuter's satisfaction with Lagos BRT services. The study reveals a strong positive relationship between Smartcard usage and BRT service satisfaction (r = 0.620) and this is statistically significant as P < 0.05. Hence, there are real evidences that Smartcard usage is associated with commuters' BRT service satisfaction.

This implies that an increase in Smartcard usage is more likely to bring about an increase in commuters' BRT service satisfaction.

The study further examined the relationship between Smartcard usage and two control variables; 'age' and 'income'. The study revealed a negative relationship between Smartcard usage and commuters' age (r = -0.236) (see Table 2). This implies that with increase in commuter's age, the usage of Smartcard decreases, therefore younger commuters are more likely to use Smartcards more. However, this is not statistically significant (P >0.05), hence increase or decrease in Smartcards usage does not significantly relate to increase or decrease in BRT commuters' age. The study also revealed that no relationship exists between Smartcard usage and commuters' income level (r = 0.000) (see Table 2). Again, this is not statistically significant (P > 100 0.05), hence, there are no real evidences that Smartcard usage is not associated with commuters' income level.

Regression Analysis:

The study further conducted a regression analysis to reveal how much of a total variation in BRT service satisfaction (BRT-SS) can be explained as regards variation in Smartcard usage (ScU). Table 3 shows that R2 = 0.384, hence 38.4% variation in BRT service satisfaction can be explained by Smartcard usage. The ANOVA table (table 4) shows how well the regression model predicts BRT service satisfaction. In this case, the regression model predicts BRT service satisfaction well since P<0.05.

The coefficients table (table 5) provides information that predicts BRT service satisfaction from Smartcard usage as well as determines if Smartcard usage contributes statistically significantly to the model. Hence the regression equation is given as: BRT-SS = 1.583 + 0.275 (ScU).

Table 2: Correlations

		1	2	3	4	5
Electronic Smart Card Usage	Pearson Correlation	1				
	Sig. (2-tailed)					
BRT Usage Frequency	Pearson Correlation	.091	1		.	
	Sig. (2-tailed)	.791				
BRT Service Satisfaction	Pearson Correlation	.620*	.020	1		
	Sig. (2-tailed)	.042	.902			
Age	Pearson Correlation	-.236	.083	-.152	1	.
	Sig. (2-tailed)	.485	.549	.330		
Commuters Income Level	Pearson Correlation	.000	-.119	.187	.342*	1
	Sig. (2-tailed)	1.000	.436	.275	.020	

*. Correlation is significant at the 0.05 level (2-tailed).

Table 3: Model Summary[b]

Model	R	R^2	Adjusted R^2	Std. Error of the Estimate
1	.620[a]	.384	.316	1.010

Predictors: (Constant), Smart Card Usage

Table 4: ANOVA[b]

Model		Sum of Squares	Df	Mean Square	F	Sig.
1	Regression	5.730	1	5.730	5.618	.042a
	Residual	9.179	9	1.020		
	Total	14.909	10			

Table 5: Coefficients[a]

Model		Unstandardized Coefficients		Standardized Coefficients	t	Sig.
		B	Std. Error	Beta		
1	(Constant)	1.583	.637		2.485	.035
	Smart Card Usage	.275	.116	.620	2.370	.042

*a. dependent variable: BRT Service Satisfaction

III. Conclusion

This study shows that most Lagos commuters are aware of the BRT system and the Lagos BRT services are deployed mostly by younger commuters than the older ones. Significantly, the survey demonstrated a good relationship between Service satisfaction and Smart card usage. Also, the adoption of the electronic card payment system (e-Purse) by commuter is still very low due to commuters' lack of know-how on the e-Purse card usability and accessibility. Of the few commuters that uses the electronic card payment system (e-Purse), a significant number have had challenges using the system. Challenges such as non-availability of the electronic payment device in most BRT buses and lack of access to where the e-Purse card can be recharged easily. Regardless of these challenges, commuters prefer the e-Purse card payment system to the paper ticketing system if the e-Purse card payment system is adequately improved upon. Interestingly, most commuters seem to be satisfied with the Lagos BRT services. In addition, the usage of Smartcards by commuters has a significant positive relationship with BRT service satisfaction. Contrarily, e-Purse capacity to effectively manage electronic fare collections is doubtful due to its limited capacity. Also, the superiority of e-Purse local

monitoring station as well as the security of fare payment devices in off- board locations and bus stops cannot be clearly proven indicating a need for increase in their absorptive capacity. More so, the issue of innovation and integration of other services and products (such as; the storage of commuter's data and analysis of passenger flows) into the contactless smart card still remains a myth. Also, there is absence of competition in the electronic payment system service provision and this may be the reason for the absence of innovation and other value-added services within the electronic payment system.

Based on the findings of this study, the study recommends the following:

- The BRT policies should be redesigned to include features/ services that will increase commuters' patronage particularly the older population.
- Fare structure policies that will accommodate more low income earners should be adopted as well.
- Also, operators should ensure transparency in fare charges and also make the electronic payment cards more accessible thereby improving commuters' confidence with respect to charges and card availability. Transparency in fare charges via text messages that can alert commuters of the charge deductions after paying for a ride.

- Also, proper handling of bus transfers with regards to charging fares and the inclusion of user information on smart cards are also important.
- BRT operators should ensure the availability of tap to pay machines in all BRT buses and commuters should be adequately educated on the usability and accessibility of the electronic payment card (e-Purse card).
- Transport regulatory Authorities should show interest in standards

for a broad range of solutions deployed within its purview. This is because such solutions influence the success of transport projects as well. Solutions often times not developed for particular climes may prove costly to maintain and improve. The inability to guarantee compliance to operational and technical requirements with regards to user's technical private partners shouldn't be tolerated by regulatory authorities.

References

[1] ACR1222L VisualVantage USB NFC Reader with LCD. (2016). Retrieved April 26, 2016, from http://www.acs.com.hk/en/products/169/acr1222l-visualvantage-usb-nfc-reader-with-lcd/

[2] Aderamo, A.J. (2012). Urban Transportation Problems and Challenges in Nigeria: A Planner's View. *Prime Resource Education*, 2:198-203.

[3] Adeoti, J. O. (2013). Explaining the Characteristics and Efficiency of Manufacturing Firms in Lagos. *European Journal of Social Science*, 37 (1):121-138.

[4] Azeta, J., Okokpujie, K. O., Okokpujie, I. P., Osemwegie, O., & Chibuzor, A. (2016). A Plan for Igniting Nigeria's Industrial Revolution. International Journal of Scientific & Engineering Research, 7(11), 489.

[5] Cohen, W. M., and Levinthal, D. A. (1990). Absorptive capacity: A New Perspective on Learning and Innovation. *Administrative Science Quarterly*, 35(1):128−152.

[6] Guardian Nigeria Newspaper (2015, November 10). Ambode commissions LAMATA's Mile 12 to Ikorodu BRT Extension.The Guardian Newspaper Nigeria. Retrieved from http://guardian.ng/features/ambode-commissions-lamatas-mile-12-to-ikorodu-brt-extension/

[7] Hook, W., Breithaupt, M., Wright, L., Hidalgo, D., Menckhoff, G., Martins, W. C., and Rutherford, S. (2014). The BRT Standard 2014 Edition. Institute for Transportation and Development Policy (ITDP), Washington D C.

[8] LEDS GP (2016). Fight Poverty by Reducing Greenhouse Gas Emissions from Urban Transport, Low Emission Development Strategies Global Partnership (LEDS GP).

[9] Levinson, H. S., Zimmerman, S., Clinger, J., and Rutherford, G. S. (2002). Bus rapid transit: An

overview. *Journal of Public Transportation*, 5(2): 1.

[10] Ma, Y., Sang, N., Jiang, W. And Zhang, L. (21012). Feedback-Controlled Security-Aware and Energy-Efficient Scheduling for Real-Time Embedded Systems. *Embedded and Multimedia Computing Technology and Service*, 181: 255-268.

[11[Mobereola, D. (2009). Africa's First Bus Rapid Transit Scheme. The Lagos BRT-Lite System, Sub-Saharan Africa Transport Policy Program. SSATP Discussion Paper No.9. Urban Transport Series.

[12] Obiazi, A. M. O., Anyasi, F. I., Okokpujie, K. O., Erua, J. B., & Osahenvemwen, O. A. (2009). An Innovative Technique in Switching Electrical Appliances: An Omni-Directional RF Remote Control Switch Mechanism. Journal of Engineering and Applied Sciences, 4(4), 268-271.

[13] Odufwa, B., Oriola, S. and Otubaga, O. (2012). Women and the Use of Public Transportation. An Explorative Study in Lagos Metropolis, Nigeria. Masters Thesis, Institute for Housing and Urban Development Studies, Nigeria.

[14] Ogunkoya, A. O. (2008). Public Transport Innovation: The Impact of BRT on Passenger's Movement in Lagos Metropolitan area of Nigeria. *Medwell Journals*, 5 (8): 845-852.

[15] Ogwude, C. (2011) Managing Transportation Infrastructure in Nigeria Cities. Nigeria Institute of Town Planner (NITP) and Town Planner Registration Council of Nigerian (TOPREC) Mandatory Continuing Professional Development Programme (MCPDP), Ibadan Nigeria.

[16] Okagbue, H.I., Adamu, M.O., Iyase, S.A. and Owoloko, E.A. (2015). On the Motivations and Challenges Faced by Commuters Using Bus Rapid Transit in Lagos, Nigeria. *The Social Sciences,* 10(6):696-701.

[17] Okokpujie, K., Noma-Osaghae, E., John, S., & Jumbo, P. C. (2017, October). Automatic home appliance switching using speech recognition software and embedded system. In Computing Networking and Informatics (ICCNI), 2017 International Conference on (pp. 1-4). IEEE.

[18] Okokpujie, Kennedy O. and Odusami , Modupe and Okokpujie, Imhade P. and Abayomi-Alli , Olusola (2017) A Model for Automatic Control of Home Appliances using DTMF Technique. International Journal of Scientific & Engineering Research, 8 (1). pp. 266-272. ISSN ISSN 2229-5518.

[19] Olusola Babatunde, S., Opawole, A., & Emmanuel Akinsiku, O. (2012). Critical success factors in public-private partnership (PPP) on infrastructure delivery in

Nigeria. *Journal of Facilities* Management, 10(3), 212-225.

[20] Oni, S. 1. (2004). Urbanization and Transportation Development in Metropolitan Lagos. In Adejugbe M. O. A. (ed.) Industrialization, Urbanization an Development in Nigeria 1950-1999. Concept publications limited, Lagos, Nigeria.

[21] Osemwegie, O., John, S., Okokpujie, K., & Shorinwa, I. (2016, December). Development Of An Electronic Fare Collection System Using Stationary Tap-Out Devices. In Computational Science and Computational Intelligence (CSCI), 2016 International Conference on (pp. 234-236). IEEE.

[22] Pelletier M., Trépanier M., Morency C. (2011). Smart card data use in public transit: A Literature Review. Transportation Research Part C: Emerging Technologies, 19(4): 557–568.

[23] Somuyiwa, A. and Adebayo, I.T. (2009). Impact of Bus Rapid Transit System (BRT) on Passengers' Satisfaction in Lagos Metropolis, Nigeria. International Journal of Creativity and Technical Development, 1 (1 – 3): 106-122.

[24] Ukpabio, M.G. (2014). A Study of Technology Acquisition and Absorptive Capacity in Nigerian Commercial Banks. A Research Project Submitted to African Institute for Science Policy and Innovation (AISPI), Obafemi Awolowo University, Ile-Ife, in Partial Fulfilment of the Award of Master of Science in Technology Management.

[25] Urbanek, A. (2015). Pricing Policy after the Implementation of Electronic Ticketing Technology in Public Urban Transport: An Exploratory Study in Poland. In J. Mikulski (Ed.), Tools of Transport Telematics (Vol. 531, Communications in Computer and Information Science, pp. 322-332). Switzerland: Springer International Publishing. doi:10.1007/978-3-319-24577-5

[26] Zahra, S.A. and George, G. (2002). Absorptive Capacity: A Review, Reconceptualization, and Extension. *Academy of Management Review*, 27:185–203.

[27] Salawu, E. Y., Okokpujie, I. P., Afolalu, S. A., Ajayi, O. O., & Azeta, J. (2018). INVESTIGATION OF PRODUCTION OUTPUT FOR IMPROVEMENT. *Internatio nal Journal of Mechanical and Production Engineering Research and Development*, *8*(1), 915-922.

[28] Nwoke, O. N., Okokpujie, I. P., & Ekenyem, S. C. (2017). INVESTIGATION OF CREEP RESPONSES OF SELECTED ENGINEERING MATERIALS. *Journal of Science, Engineering Development, Environmen*

and *Technology (JOSEDET)*, *7*(1), 1-15.

[29] AK, E. C. (2016). Stability Analysis of Model Regenerative Chatter of Milling Process Using First Order Least Square Full Discretization Method. *International*

Journal of Mechanics and Applications, *6*(3), 49-62.

[30] Okokpujie, K. O., Abayomi-Alli, A., Abayomi-Alli, O., Odusami, M., Okokpujie, I. P., & Akinola, O. A. (2017). AN AUTOMATED ENERGY METER READING SYSTEM USING GSM TECHNOLOGY.